Supplementary Information for

High-density asymmetric iron dual-atom sites for efficient and stable electrochemical water oxidation

Lili Zhang[1], Ning Zhang[2], Huishan Shang[1,], Zhiyi Sun[3], Zihao Wei[3], Jingtao Wang[1,*], Yuanting Lei[1], Xiaochen Wang[1], Dan Wang[1], Yafei Zhao[1], Zhongti Sun[4,*], Fang Zhang[5], Xu Xiang[6], Bing Zhang[1], Wenxing Chen[3,*]*

[1] School of Chemical Engineering, Zhengzhou University, Zhengzhou 450001, P. R. China.

[2] Changchun Institute of Applied Chemistry Chinese Academy of Sciences. P. R. China.

[3] Energy & Catalysis Center, School of Materials Science and Engineering, Beijing Institute of Technology, Beijing 100081, China.

[4] School of Materials Science and Engineering, Jiangsu University, Zhen-Jiang, Jiangsu 212013, PR China.

[5] Analysis and Testing Center, Beijing Institute of Technology, Beijing 100081, P. R. China.

[6] State Key Laboratory of Chemical Resource Engineering, Beijing University of Chemical Technology, Beijing 100029, P. R. China.

Table of Contents

Supplementary Figures **2**

Supplementary Tables **92**

Supplementary Notes **107**

Supplementary Figures

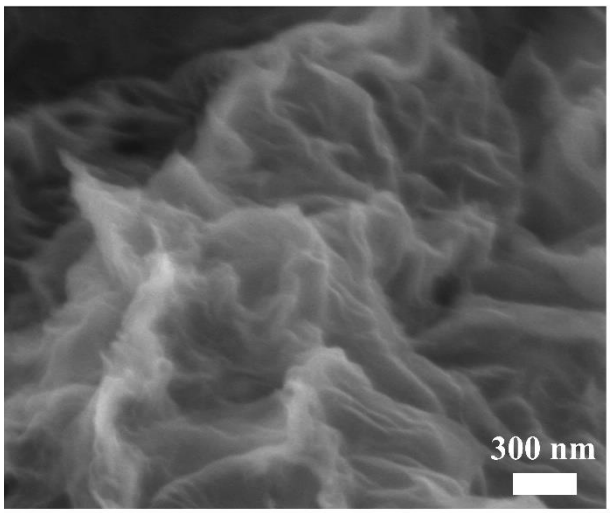

Supplementary Fig. 1. High magnification SEM image of *A*-$Fe_2S_1N_5$/SNC.

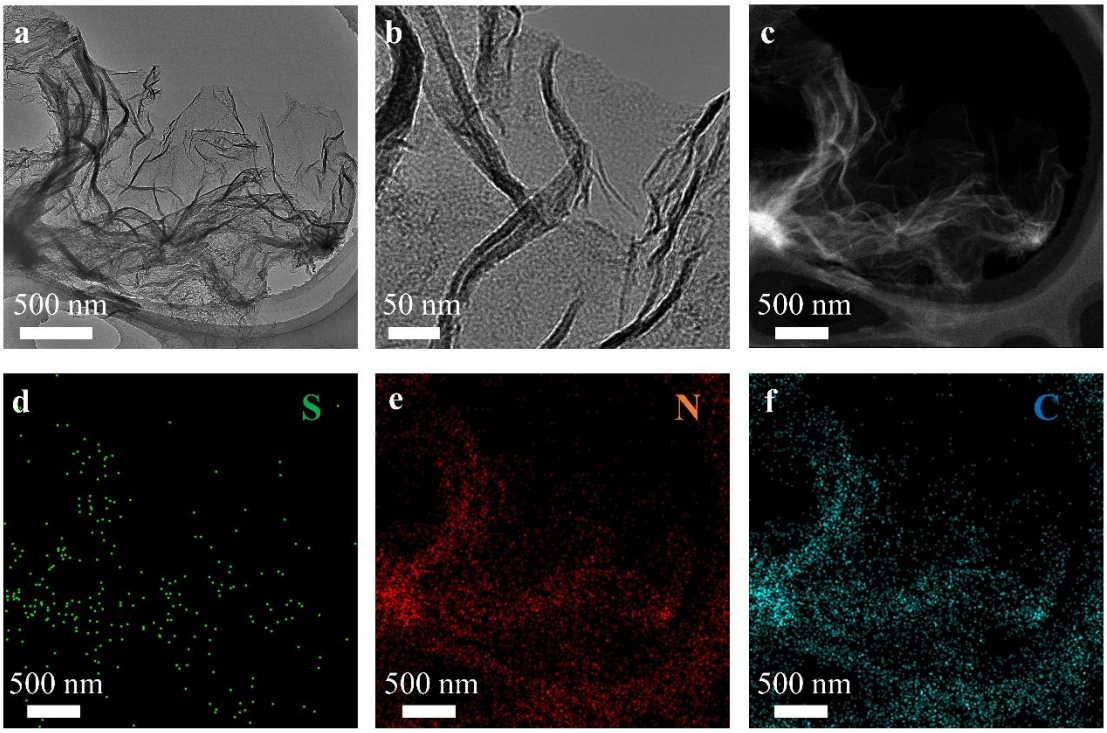

Supplementary Fig. 2. TEM images of SNC. (a) At 500 nm and (b) 50 nm scale bar showing the two-dimensional folded sheet-like structure. (c-f) Corresponding EDS mapping images of SNC. Highly wrinkled SNC nanosheets with numerous tortuous edges can be observed in the transmission electron microscope (TEM) image, which provides a considerable number of active sites for trapping and anchoring metal atoms.

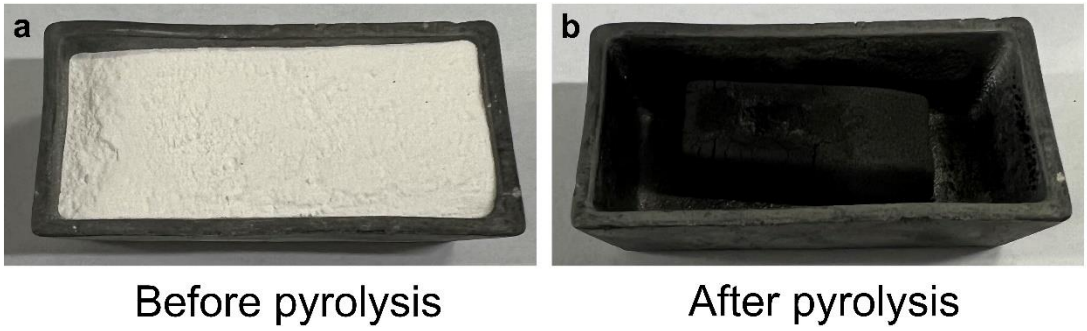

Supplementary Fig. 3. Controllable expansion preparation of SNC nanosheets. (a) Before and (b) after pyrolysis.

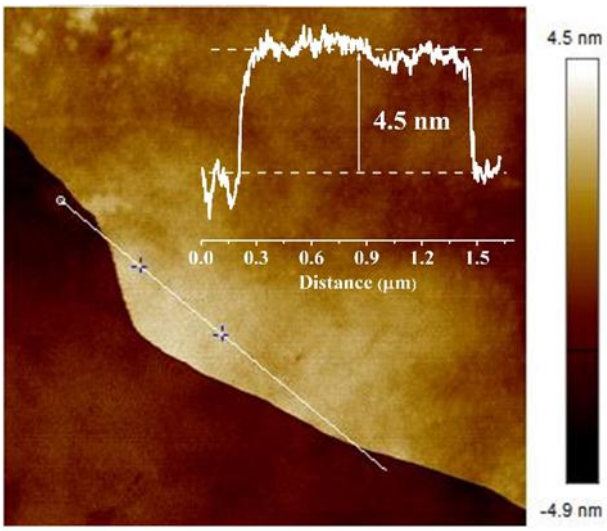

Supplementary Fig. 4. AFM image and corresponding height profile of *A*-$Fe_2S_1N_5$/SNC.

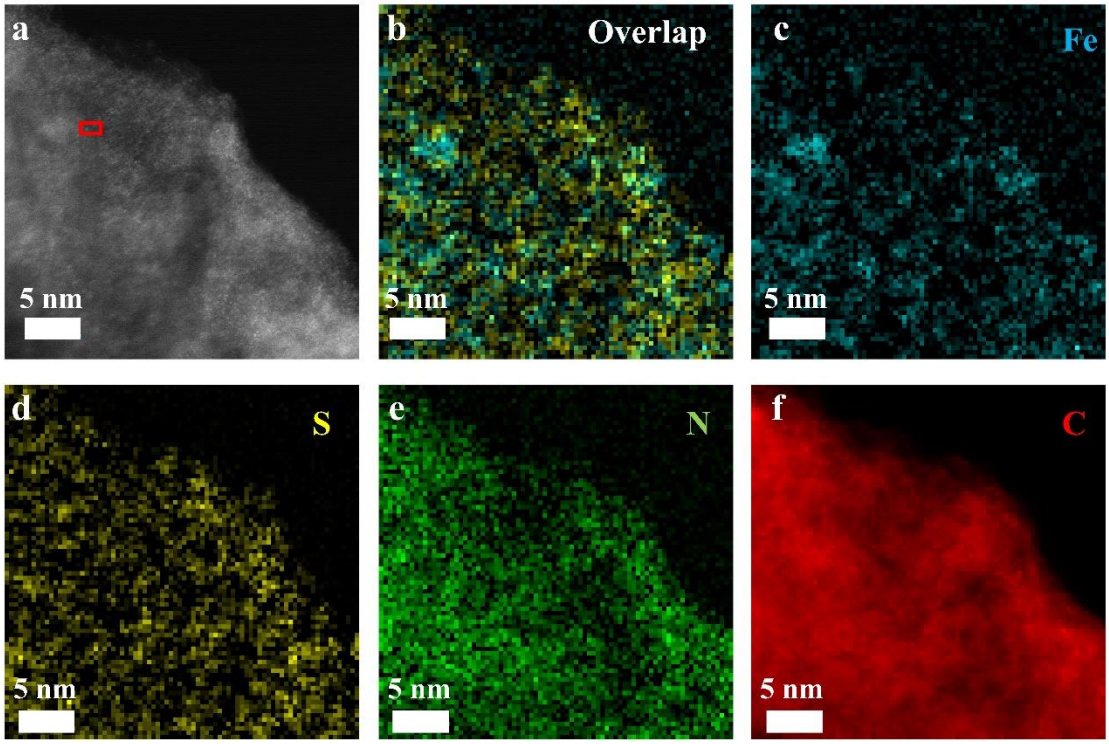

Supplementary Fig. 5. Aberration-corrected high-angle annular dark-field scanning transmission electron microscope (AC-HAADF-STEM) of *A*-$Fe_2S_1N_5$/SNC. (a) AC-STEM, (b-f) EELS mapping of Fe, S, N, and C.

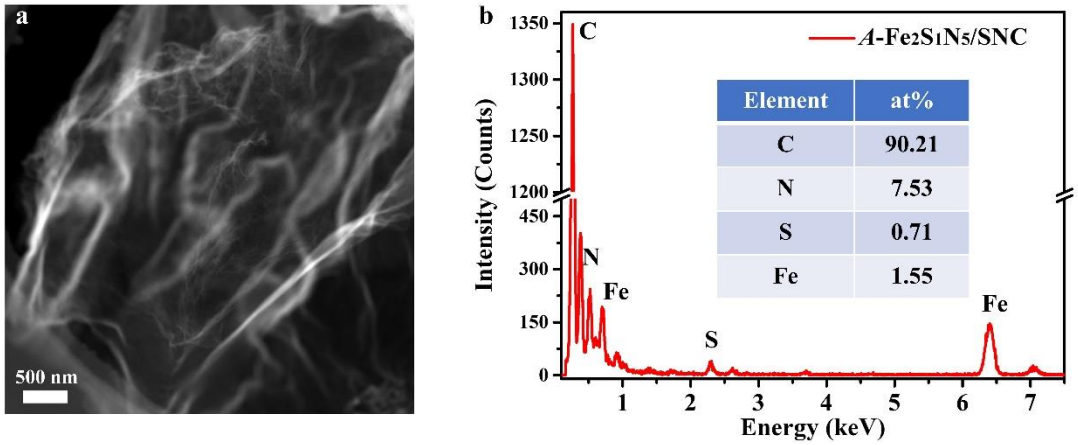

Supplementary Fig. 6. Characterizations of *A*-$Fe_2S_1N_5$/SNC. (a) HAADF-STEM image. (b) EDS spectrum. The element content in *A*-$Fe_2S_1N_5$/SNC was also labeled in the quantitative EDS spectrum.

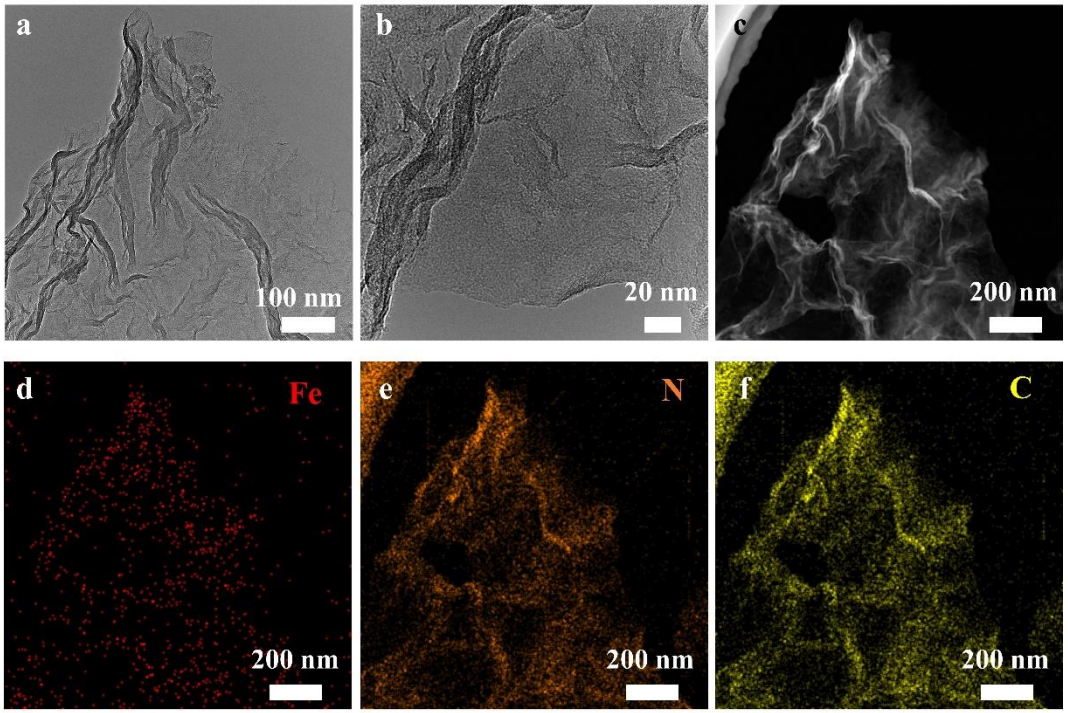

Supplementary Fig. 7. TEM images of Fe_2N_6/NC. (a) At 100 nm and (b) 20 nm scale bar showing the two-dimensional wrinkle sheet-like structure. (c-f) Corresponding EDS mapping images of Fe_2N_6/NC showing the Fe, N, and C elements are uniformly distributed throughout the entire Fe_2N_6/NC.

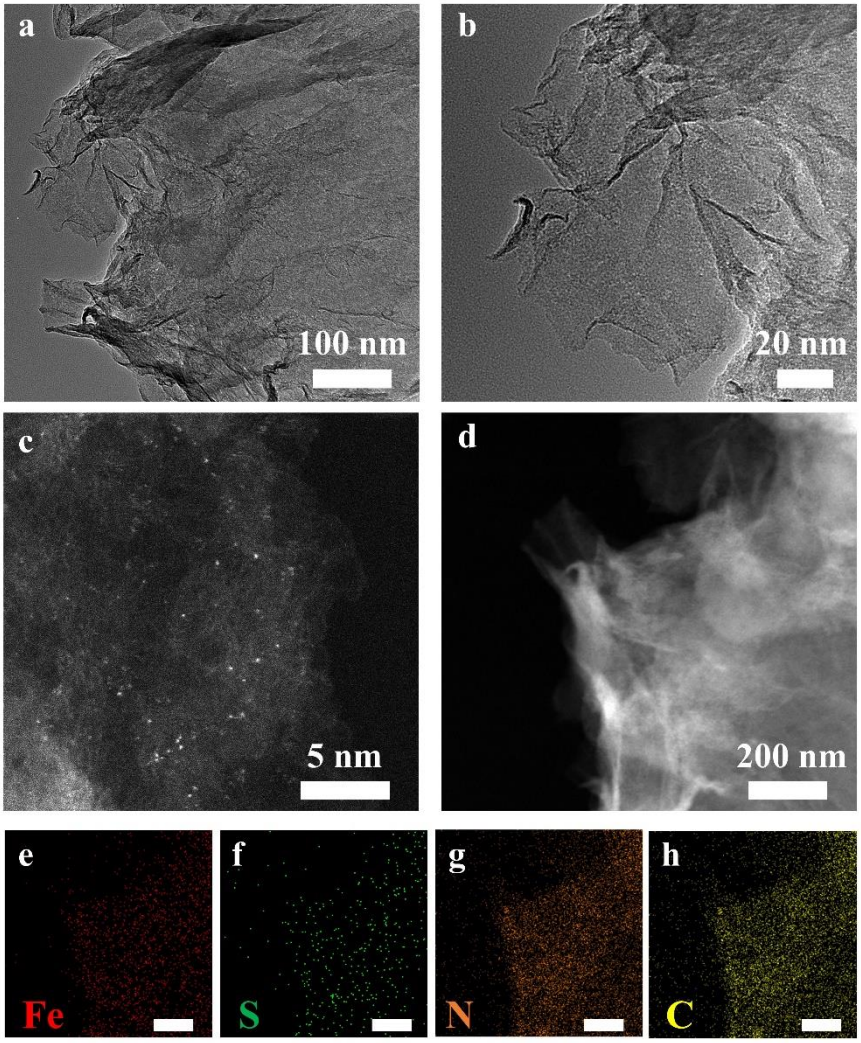

Supplementary Fig. 8. TEM images of $Fe_1S_1N_3$/NC. (a) At 100 nm and (b) 20 nm scale bar showing the two-dimensional wrinkle sheet-like structure. (c) Aberration-corrected HAADF-STEM image. (d) HAADF-STEM image. (e-h) Corresponding EDS mapping images of $Fe_1S_1N_3$/NC showing the Fe, S, N, and C elements are uniformly distributed throughout the entire $Fe_1S_1N_3$/NC. Scale bar: 200 nm.

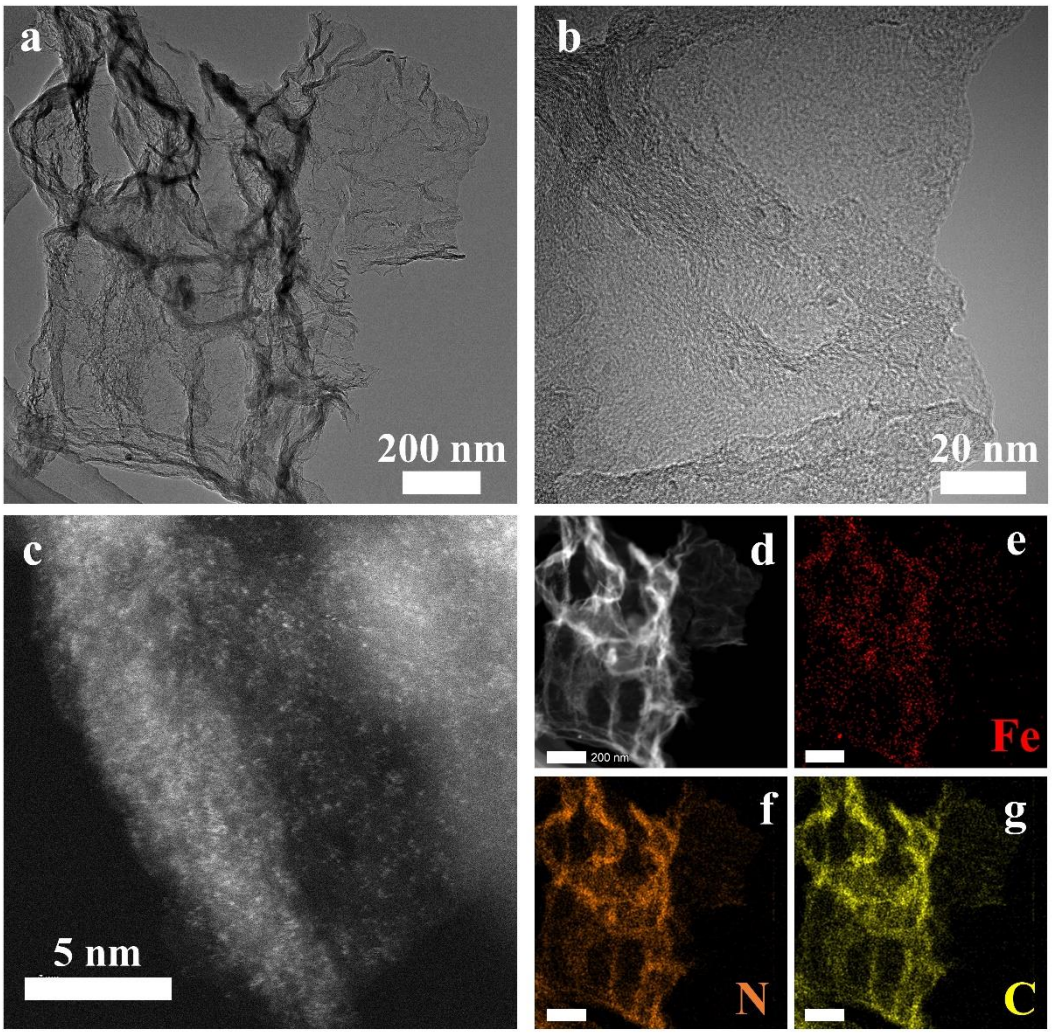

Supplementary Fig. 9. TEM images of Fe_1N_4/NC. (a) At 200 nm and (b) 20 nm scale bar showing the two-dimensional sheet-like structure. (c, d) Corresponding EDS mapping images of Fe_1N_4/NC. Scale bar: 200 nm.

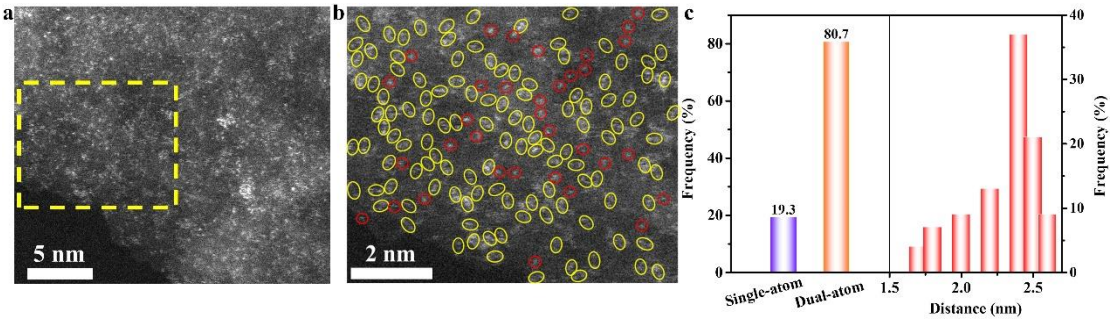

Supplementary Fig. 10. AC-HAADF-STEM of *A*-$Fe_2S_1N_5$/SNC. (a-b) AC-STEM image. The dual Fe sites were signed by the yellow oval. (c) The statistical density of the Fe-Fe dual sites and Fe single sites, as well the Fe-Fe diatomic distance from the AC-STEM images shown in (b). According to the statistical data, the proportion of diatoms Fe reaches ~80.7 %, and the proportion of single atoms Fe is ~19.3%.

The statistical analysis of the site distributions was conducted by counting the pair distance for more than 140 sites (specifically 140 groups of metal sites) on the AC-STEM image of *A*-$Fe_2S_1N_5$/SNC. Among the identified sites, the Fe-Fe dual sites were highlighted by a yellow ellipse. The majority of the dots were counted as dot pairs above 80.7%, which represent the bimetallic dual sites.

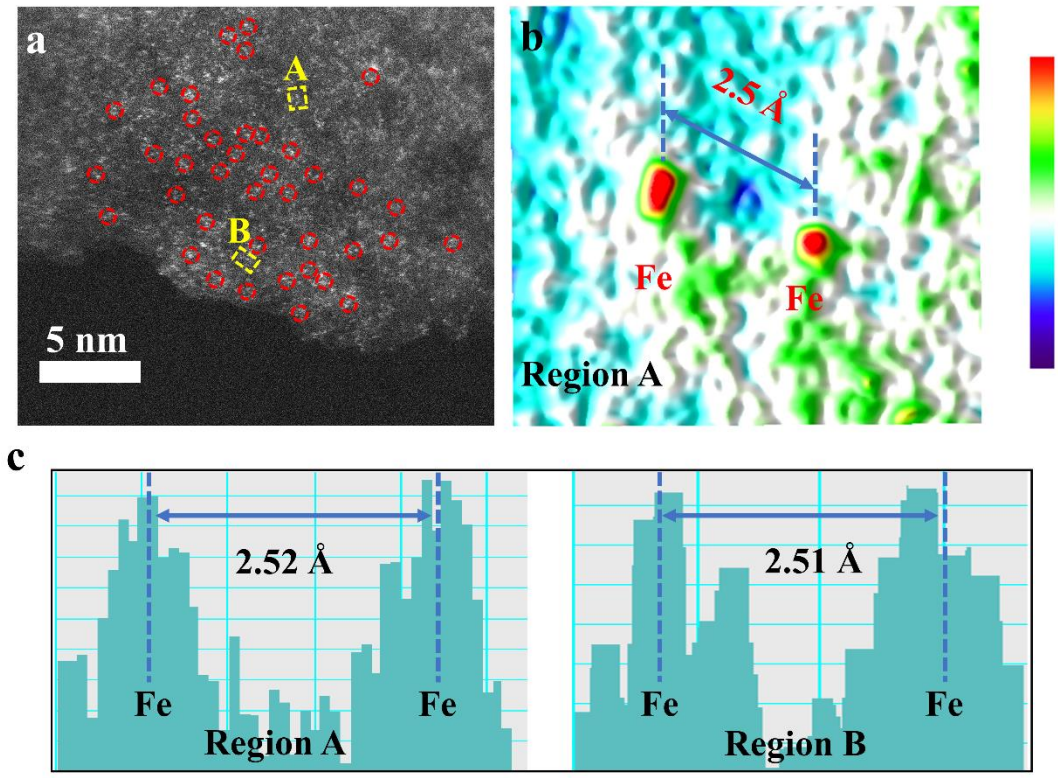

Supplementary Fig. 11. AC-HAADF-STEM of Fe_2N_6/NC. (a) Aberration-corrected HAADF-STEM of the Fe_2N_6/NC. (b) corresponding intensity profile in Region A of (a). The diatomic Fe pair is circled with the red dashed line. (c) Distance between two adjacent Fe atoms in Region A and Region B.

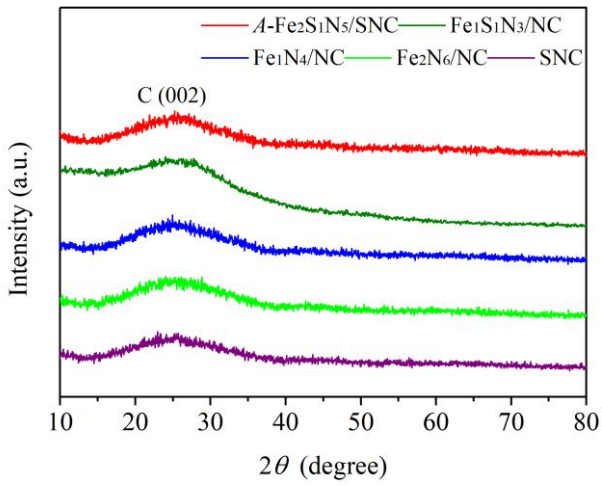

Supplementary Fig. 12. XRD patterns of *A*-$Fe_2S_1N_5$/SNC, $Fe_1S_1N_3$/NC, Fe_1N_4/NC, Fe_2N_6/NC, and SNC. The broad peaks at 20-30°and 40-50° are assigned to the (002) and (101) plane of graphite, respectively.

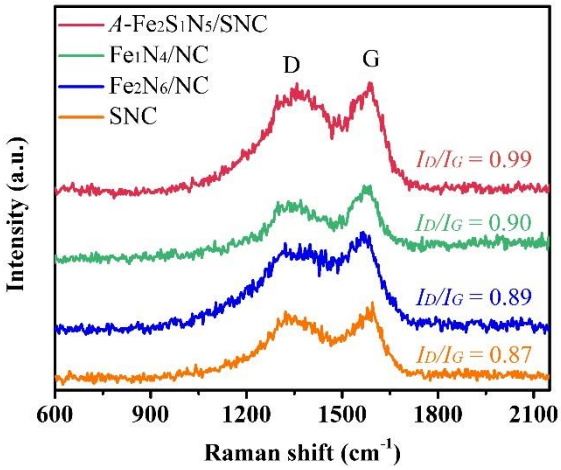

Supplementary Fig. 13. Raman patterns of *A*-$Fe_2S_1N_5$/SNC, Fe_1N_4/NC, Fe_2N_6/NC, and SNC. The results showed that I_D/I_G was slightly elevated for the *A*-$Fe_2S_1N_5$/SNC compared with the Fe_1N_4/NC and Fe_2N_6/NC, indicating a much higher percentage of carbon atoms at the defects/edges of the *A*-$Fe_2S_1N_5$/SNC thin sheet, which were regarded as potential active sites for catalysis.

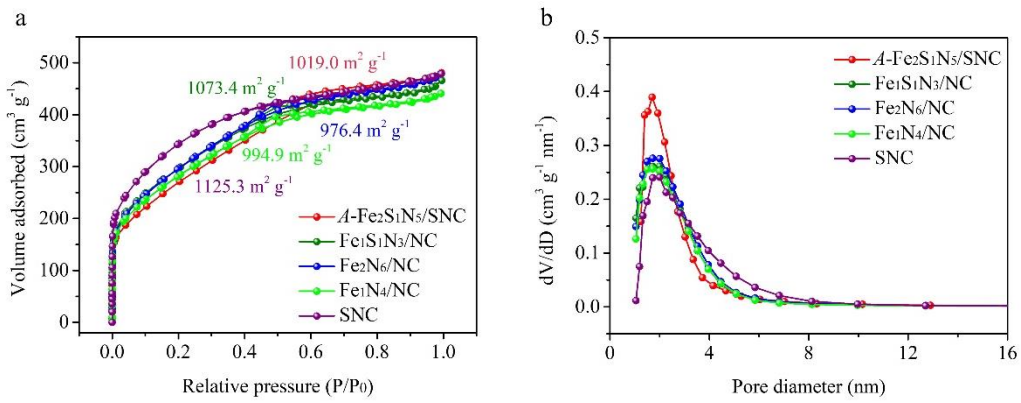

Supplementary Fig. 14. BET analyses of *A*-$Fe_2S_1N_5$/SNC, $Fe_1S_1N_3$/NC, Fe_2N_6/NC, Fe_1N_4/NC, and SNC catalysts. (a) N_2 adsorption and desorption isotherms. (b) The corresponding pore-size distributions.

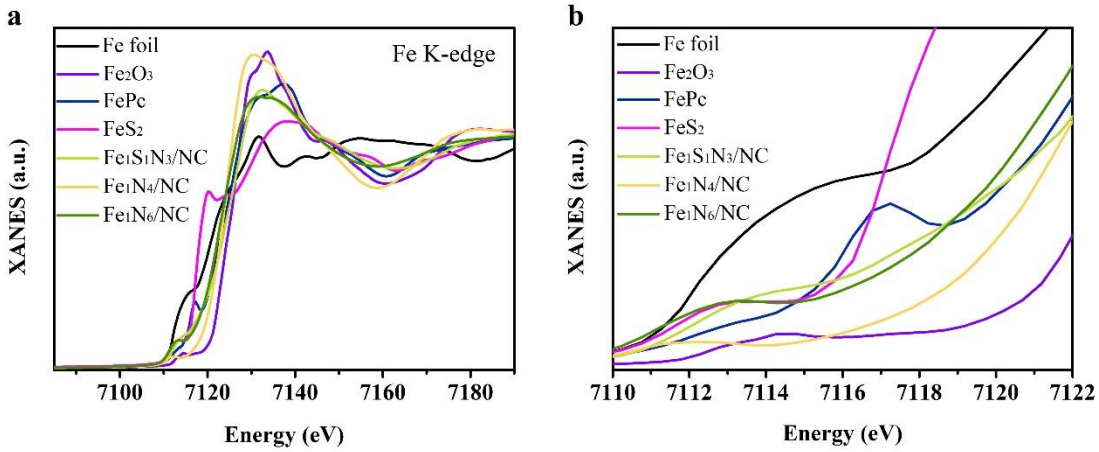

Supplementary Fig. 15. Characterization of Fe oxidation state from XANES. (a-b) The Fe K-edge XANES spectra of the references (Fe foil, Fe_3O_4, FePc, FeS_2, $Fe_1S_1N_3$/NC, Fe_1N_4/NC, and Fe_2N_6/NC).

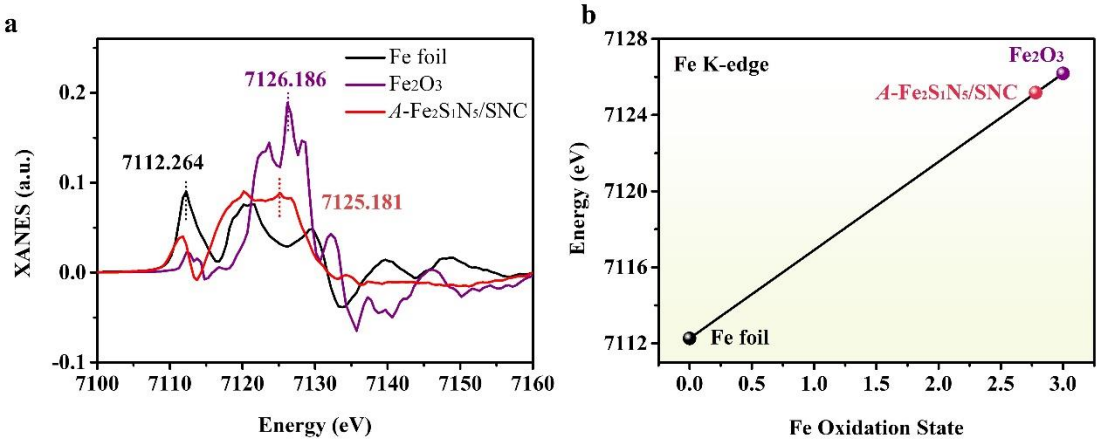

Supplementary Fig. 16. XANES measurements. (a) First-derivative XANES curves of Fe foil, Fe_3O_4, and *A*-$Fe_2S_1N_5$/SNC. (b) Correlation between the Fe oxidation state and the energy position of the XANES spectrum, determined as the first maximum of the first derivative spectrum of *A*-$Fe_2S_1N_5$/SNC and different Fe reference compounds.

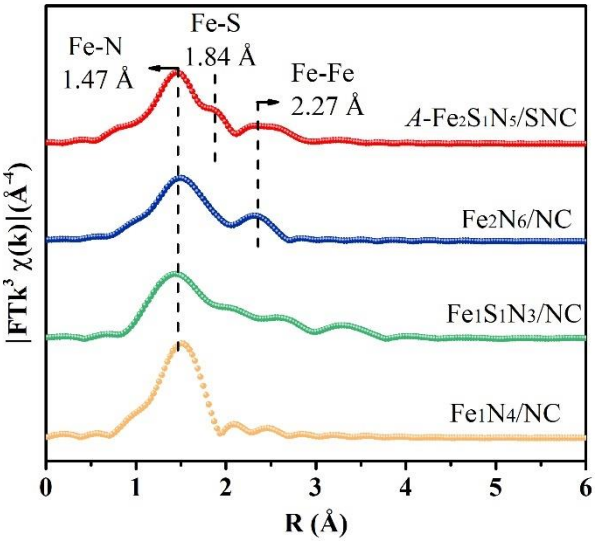

Supplementary Fig. 17. FT-EXAFS fitting curves of *A*-$Fe_2S_1N_5$/SNC, $Fe_1S_1N_3$/NC, Fe_2N_6/NC, and Fe_1N_4/NC.

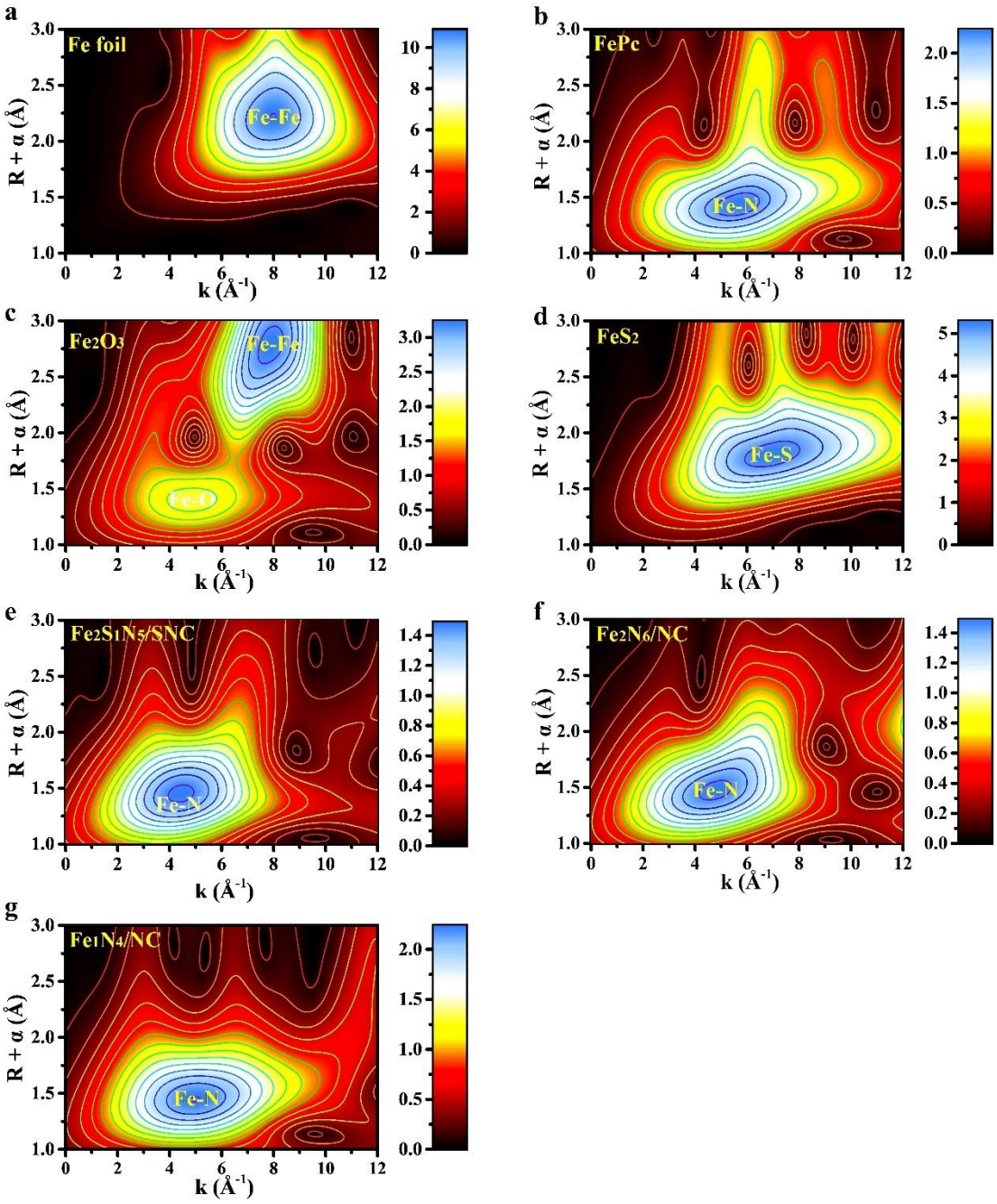

Supplementary Fig. 18. WT-EXAFS plots. (a) Fe foil, (b) FePc, (c) Fe_2O_3, (d) FeS_2, (e) *A*-$Fe_2S_1N_5$/SNC, (f) Fe_2N_6/NC, and (g) Fe_1N_4/NC.

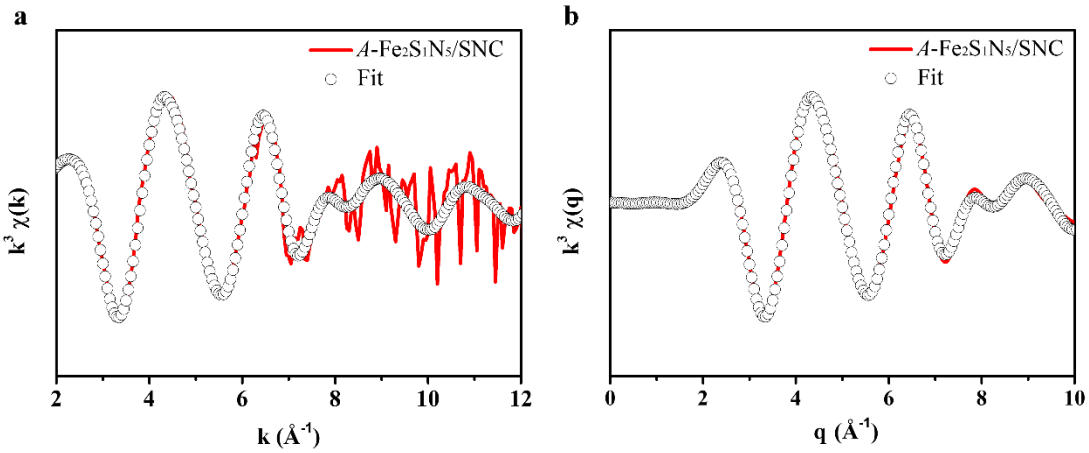

Supplementary Fig. 19. EXAFS fitting of *A*-$Fe_2S_1N_5$/SNC. (a) the EXAFS fitting curve of *A*-$Fe_2S_1N_5$/SNC at Fe K-edge. We carried out EXAFS curve-fitting for the first coordination shell of Fe by considering two backscattering paths, including Fe-N and Fe-S. (b) q space fitting curve at Fe K-edge of *A*-$Fe_2S_1N_5$/SNC.

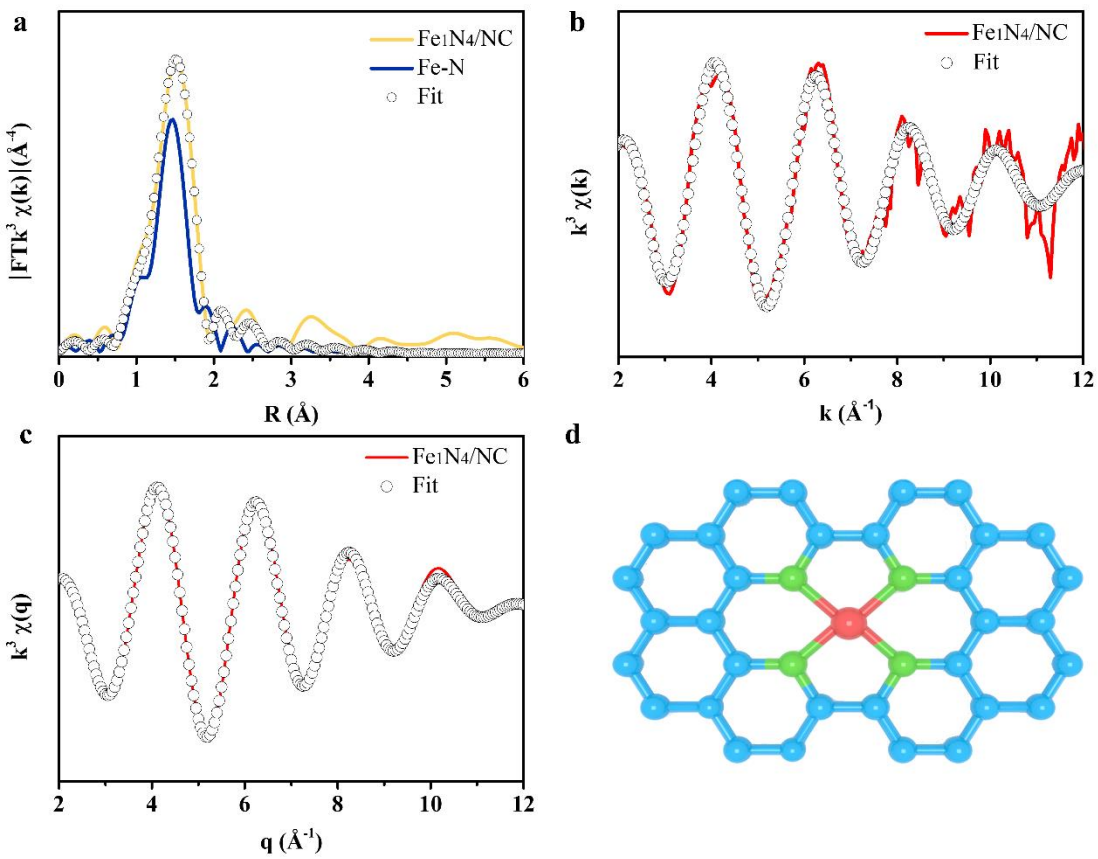

Supplementary Fig. 20. Atomic coordination environment of Fe_1N_4/NC. (a) FT k^3-weighted EXAFS spectra of Fe_1N_4/NC and the reference samples. (b) FT-EXAFS fitting curves of Fe_1N_4/NC and the corresponding Fe K-edge EXAFS fitting curves. (c) q space fitting curve at Fe K-edge. (d) Atomic interface structure model of Fe_1N_4/NC. The gray, blue, and orange spheres represent the C, N, and Fe elements, respectively.

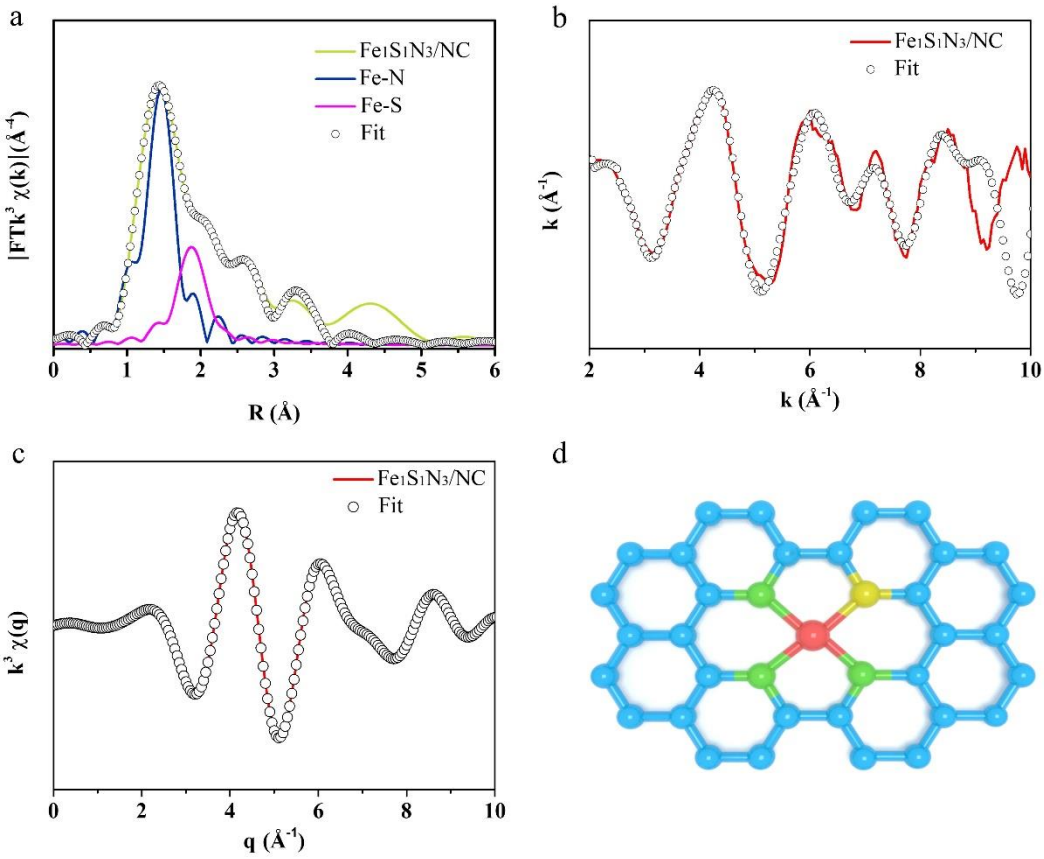

Supplementary Fig. 21. Atomic coordination environment of $Fe_1S_1N_3$/NC. (a) FT k^3-weighted EXAFS spectra of $Fe_1S_1N_3$/NC and the reference samples. (b) FT-EXAFS fitting curves of $Fe_1S_1N_3$/NC and the corresponding Fe K-edge EXAFS fitting curves. (c) q space fitting curve at Fe K-edge. (d) Atomic interface structure model of $Fe_1S_1N_3$/NC. The gray, yellow, blue, and orange spheres represent the C, S, N, and Fe elements, respectively.

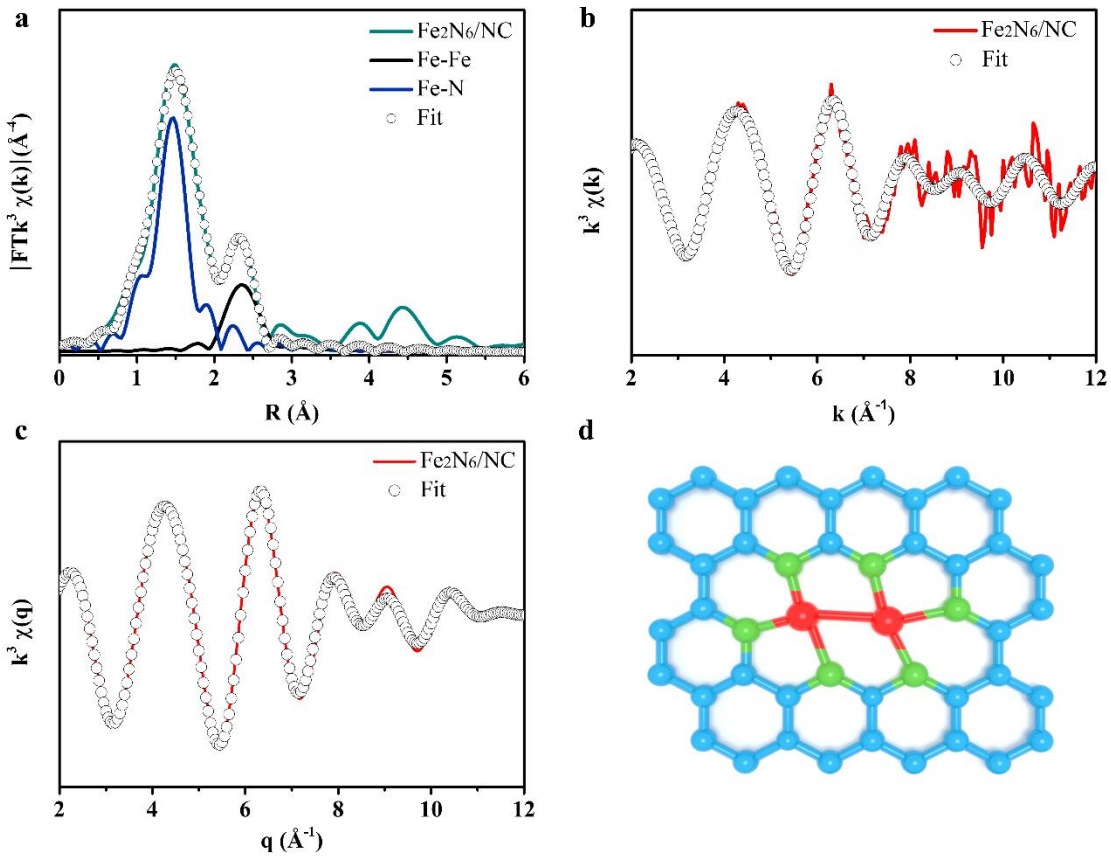

Supplementary Fig. 22. Atomic coordination environment of Fe_2N_6/NC. (a) FT k^3-weighted EXAFS spectra of Fe_2N_6/NC and the reference samples. (b) FT-EXAFS fitting curves of Fe_2N_6/NC and the corresponding Fe K-edge EXAFS fitting curves. (c) q space fitting curve at Fe K-edge. (d) Atomic interface structure model of Fe_2N_6/NC. The gray, blue, and orange spheres represent the C, N, and Fe elements, respectively.

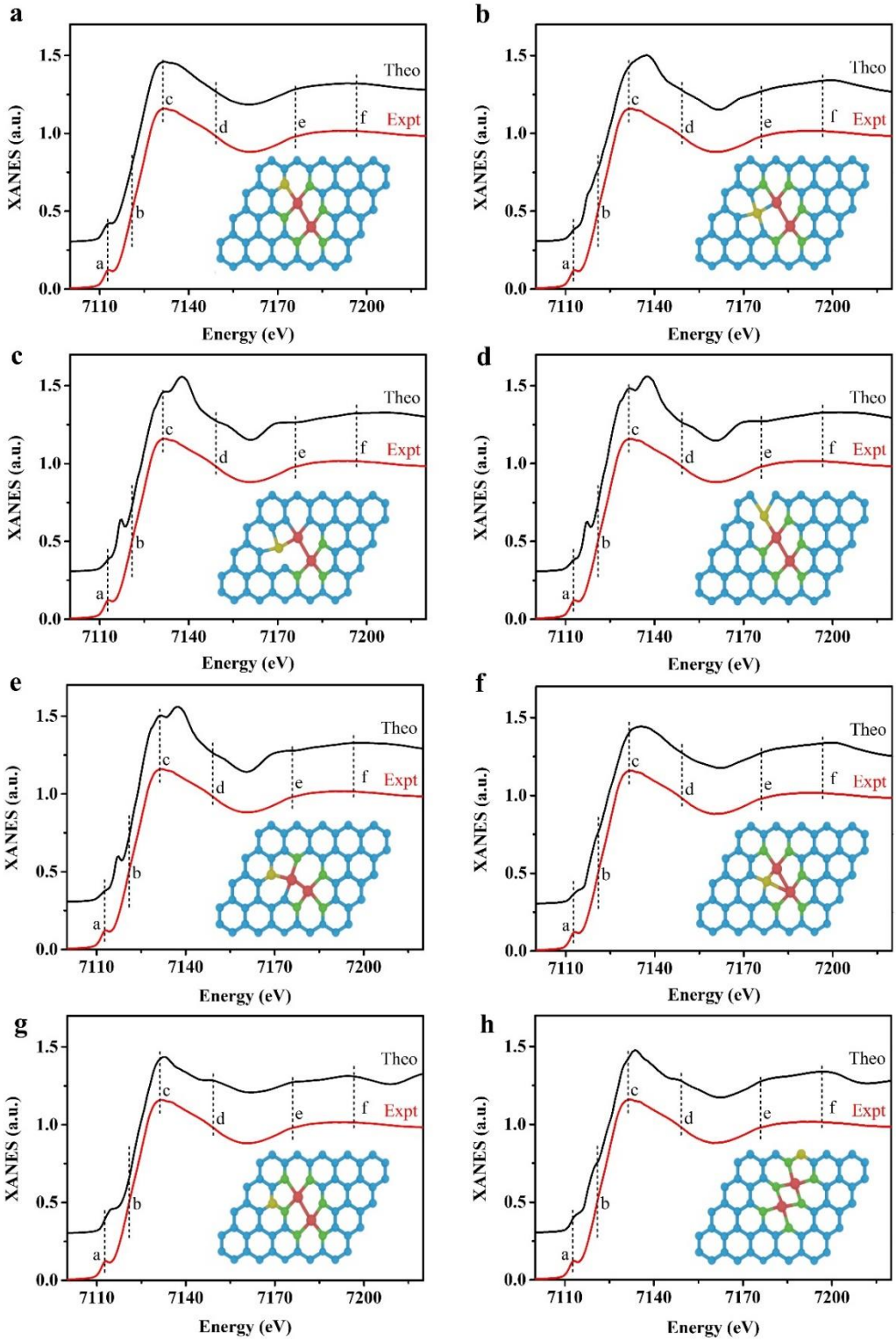

Supplementary Fig. 23. Fe K-edge XANES spectra. (a-h) Comparison between the experimental Fe K-edge XANES spectrum of *A*-$Fe_2S_1N_5$/SNC and the theoretical spectra calculated with the depicted structures based on different Fe-S or C-S positions.

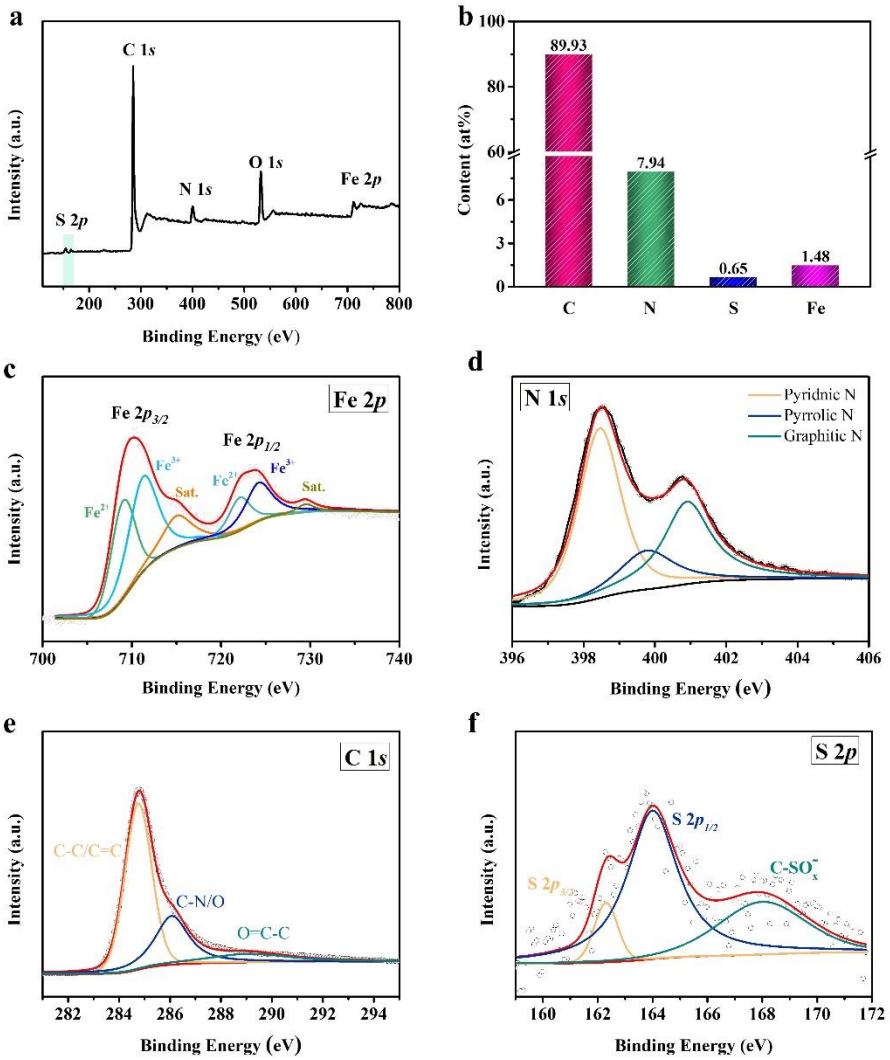

Supplementary Fig. 24. XPS spectrum of *A*-$Fe_2S_1N_5$/SNC. (a) XPS survey scan spectra of *A*-$Fe_2S_1N_5$/SNC. (b) The atomic content percentages of C, N, S, and Fe in *A*-$Fe_2S_1N_5$/SNC. (c) The Fe 2*p*, (d) N 1*s*, (e) C 1*s*, and (f) S 2*p* XPS spectrum.

It was obvious from the Fe 2*p* spectra that the two peaks at the binding energies of 709.3 eV and 722.3 eV were generally attributed to the Fe (II) species in *A*-$Fe_2S_1N_5$/SNC and the other two peaks at 712.4 eV and 724.4 eV were the characteristic peaks of Fe (III). The Fe^{3+}/Fe^{2+} ratio was 1.51 for *A*-$Fe_2S_1N_5$/SNC. The coexistence of Fe (II) and Fe (III) species, suggested partial charge transfer from SNC to Fe^{3+} centers.

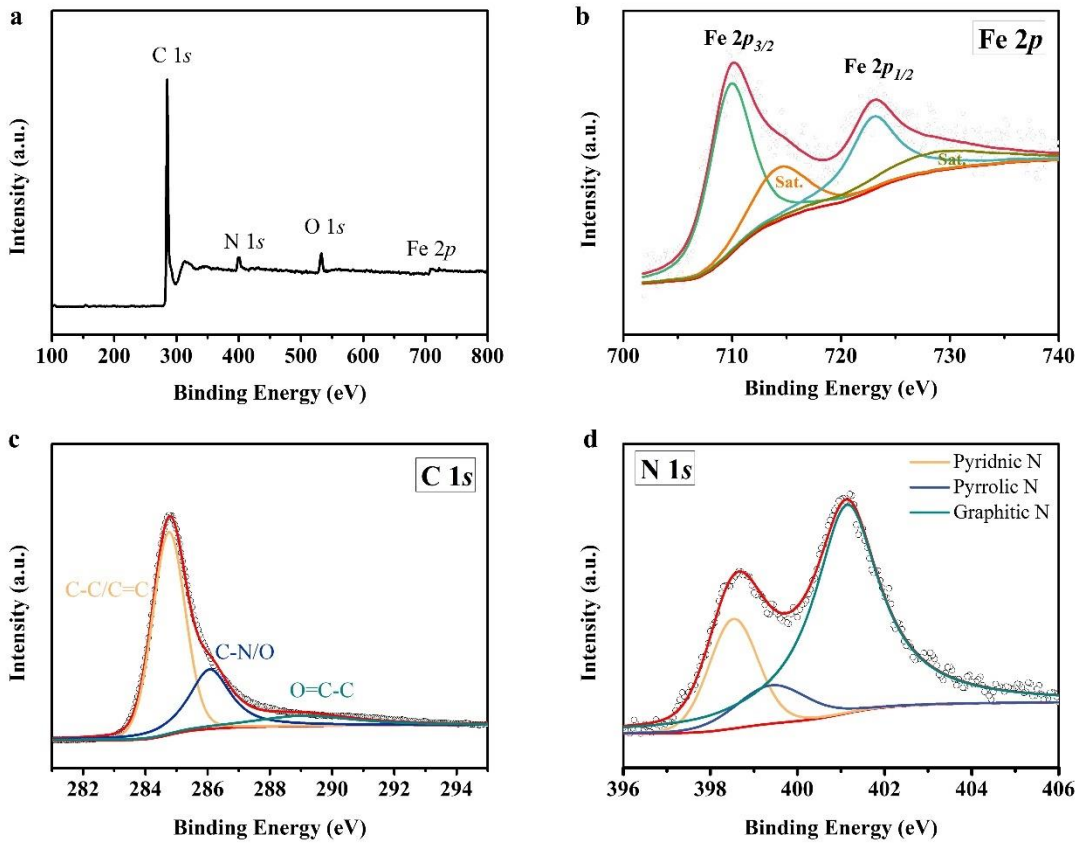

Supplementary Fig. 25. XPS spectrum of Fe_2N_6/NC. (a) survey spectrum, (b) The Fe 2*p*, (c) N 1*s*, and (d) C 1*s*.

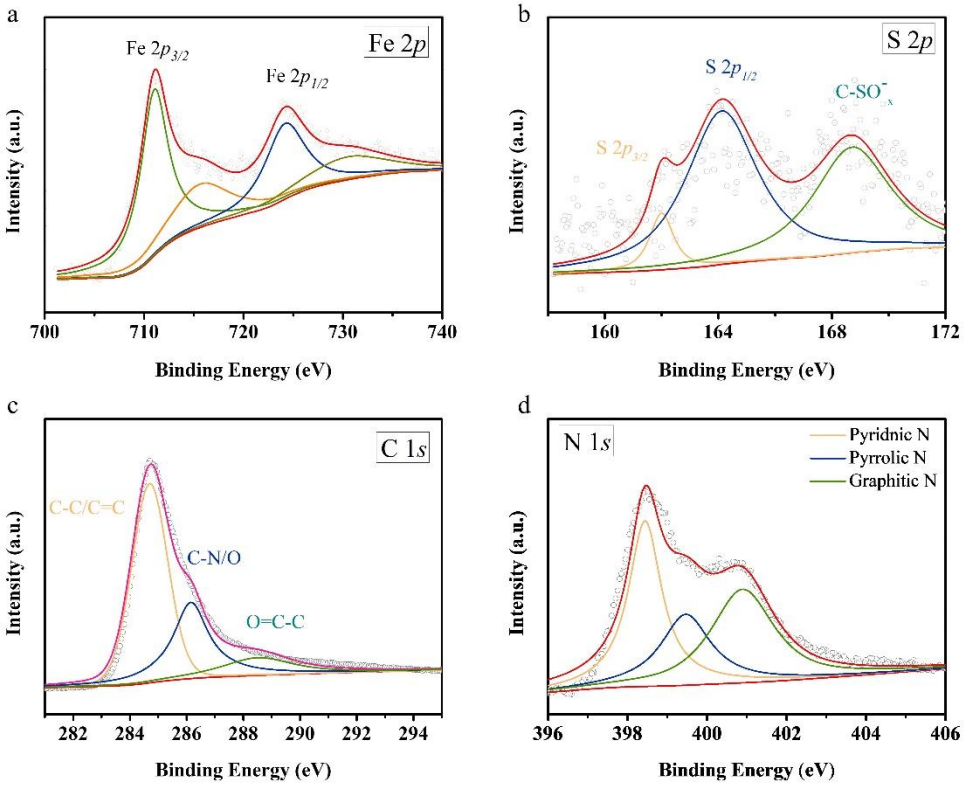

Supplementary Fig. 26. XPS spectrum of $Fe_1S_1N_3$/NC. (a) The Fe 2*p*, (b) S 2*p*, (c) C 1*s*, and (d) N 1*s*.

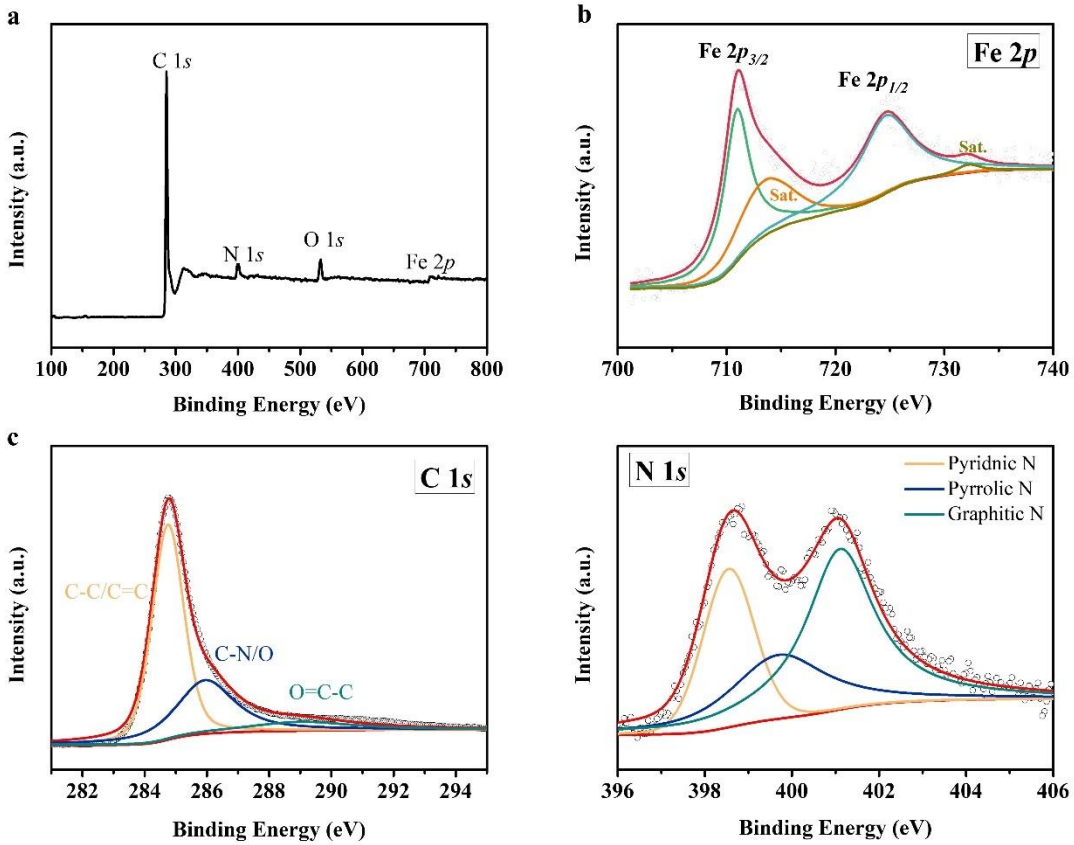

Supplementary Fig. 27. XPS spectrum of Fe_1N_4/NC. (a) survey spectrum, (b) The Fe 2*p*, (c) N 1*s*, and (d) C 1*s*.

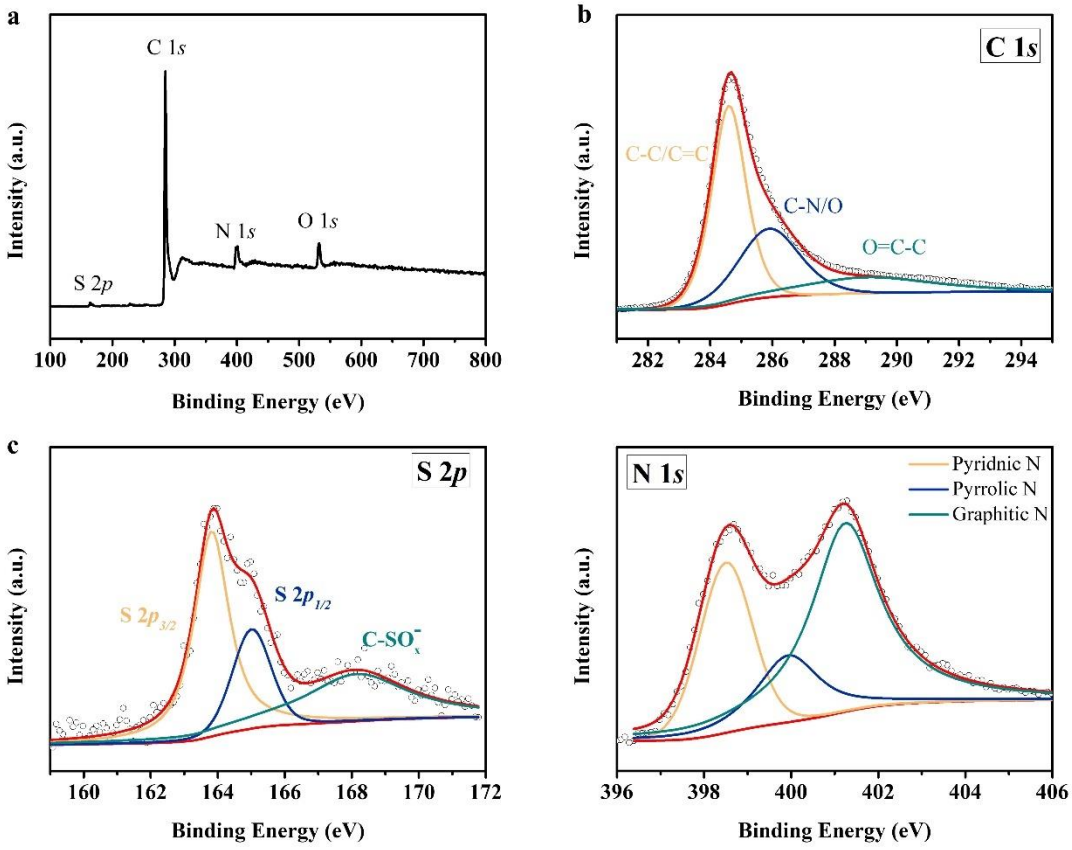

Supplementary Fig. 28. XPS spectrum of SNC. (a) C 1*s*, (b) N 1*s*, and (c) S 2*p*.

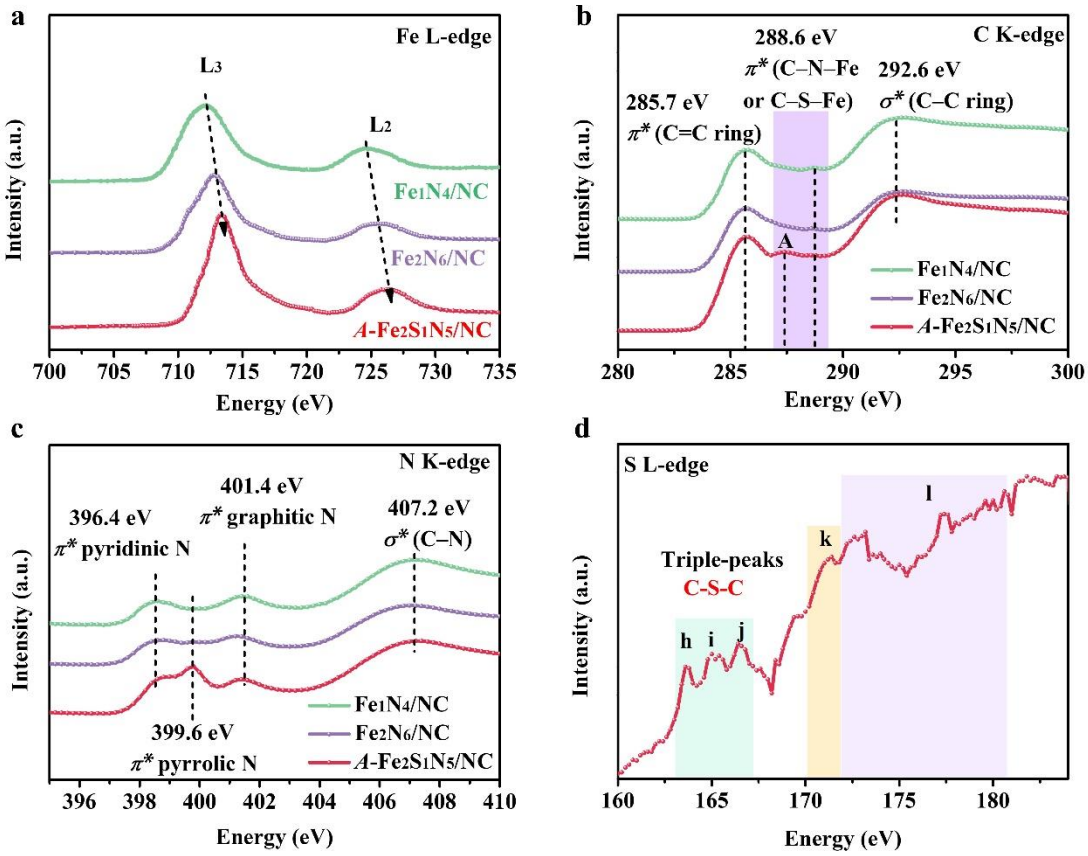

Supplementary Fig. 29. Atomic coordination structure characterization. (a) Fe L-edge XANES spectra. (b) C K-edge and (c) N K-edge XANES spectra of the *A*-$Fe_2S_1N_5$/SNC, Fe_2N_6/NC, and Fe_1N_4/NC. (d) S L-edge XANES spectra of the *A*-$Fe_2S_1N_5$/SNC. The S L-edge features result from the electronic transitions of 2p electrons to partially filled or empty molecular orbitals.

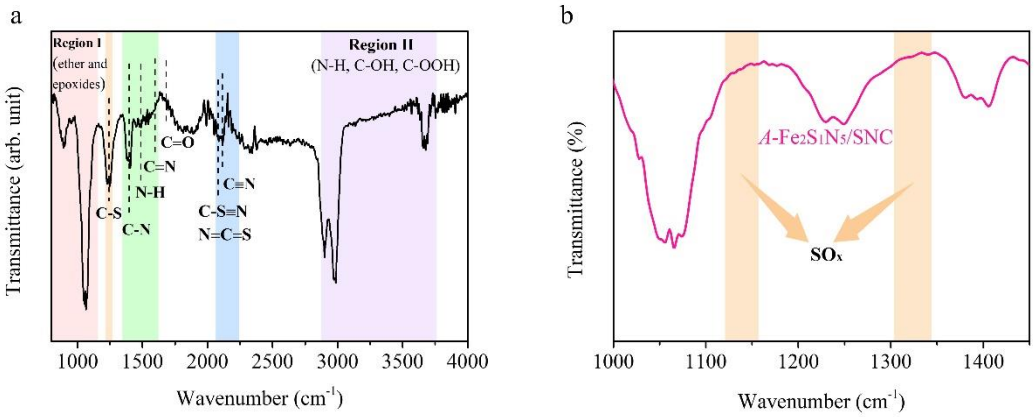

Supplementary Fig. 30. FTIR spectrum of the *A*-$Fe_2S_1N_5$/SNC catalyst. The spectrum in **Fig. R30a** reveals the presence of numerous sulfur-containing and nitrogen-containing terminal groups on the surfaces of *A*-$Fe_2S_1N_5$/SNC. The characteristic absorptions at 1350-1300 and 1160-1120 cm^{-1} are attributed to the stretching vibrations of S=O. For *A*-$Fe_2S_1N_5$/SNC, no distinctive absorptions belonging to S=O groups were found in **Fig. R30b**, which indicates the inexistence of SO_x in *A*-$Fe_2S_1N_5$/SNC.

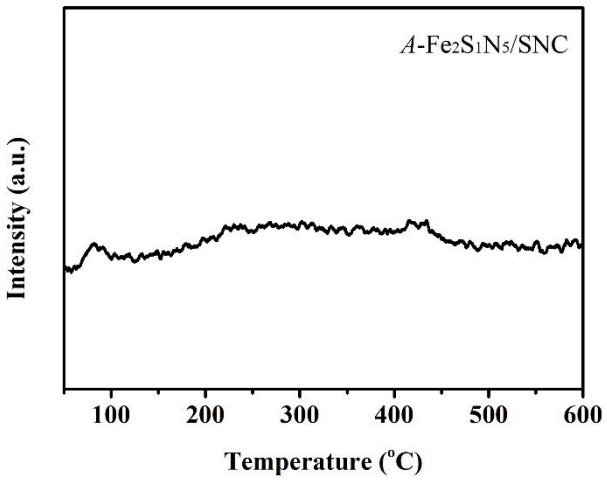

Supplementary Fig. 31. NH_3-TPD profile of *A*-$Fe_2S_1N_5$/SNC catalyst.

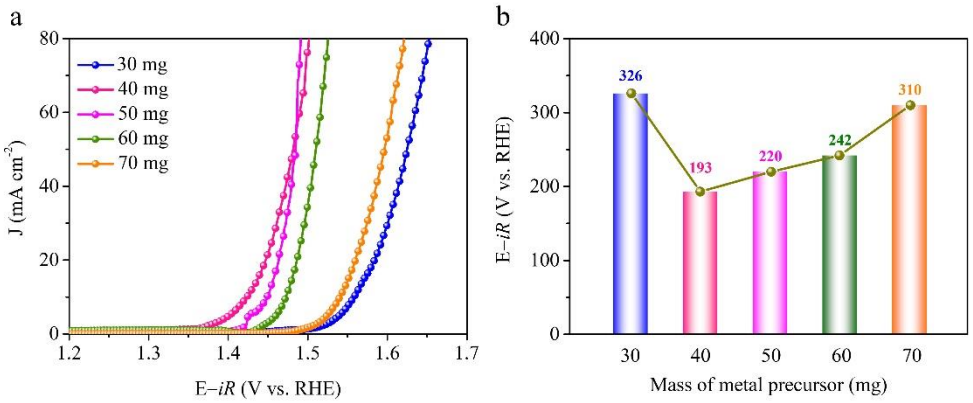

Supplementary Fig. 32. The influence of the amount of metal precursor on OER performance. (a) OER polarization curves of different usage of metal precursor content for different samples. The geometric surface area is 1.0 cm^2. (b) Activity volcano plot based on varied metal precursor content.

The effect of metal precursor (anhydrous ferric chloride) content on OER activity has also been studied. To obtain the optimal amount of metal, we used different qualities of metal precursors (30, 40, 50, 60, 70, and 100 mg) to prepare the catalyst using the same process. Subsequently, the OER performance of the resulting catalysts was evaluated. We depicted the relation of metal precursor content as the function of the overpotentials for the electrode. The OER activity of the catalyst was relatively good when the amount of metal precursor was 40 mg, as shown in the LSV curve of OER.

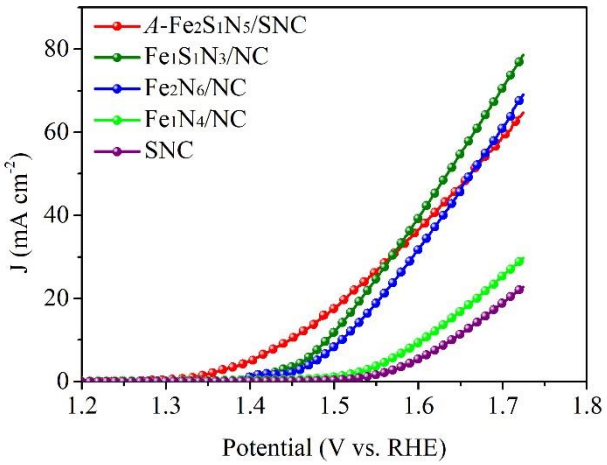

Supplementary Fig. 33. The corresponding LSV curves without *iR* compensation for *A*-$Fe_2S_1N_5$/SNC, $Fe_1S_1N_3$/NC, Fe_2N_6/NC, Fe_1N_4/NC, and SNC.

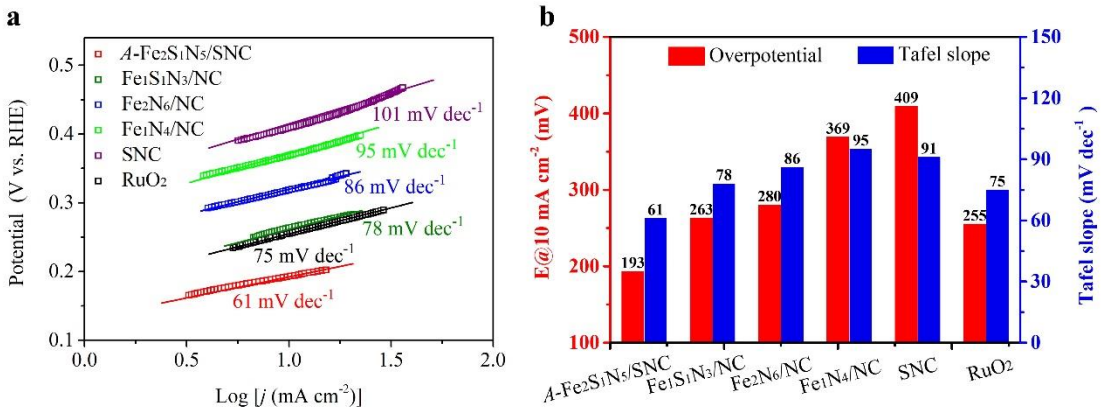

Supplementary Fig. 34. Performance characterization. (a) Tafel slope of *A*-$Fe_2S_1N_5$/SNC, $Fe_1S_1N_3$/NC, Fe_2N_6/NC, Fe_1N_4/NC, and RuO_2. (b) Comparison of overpotential and Tafel slope values at a current density of 10 mA cm^{-2}.

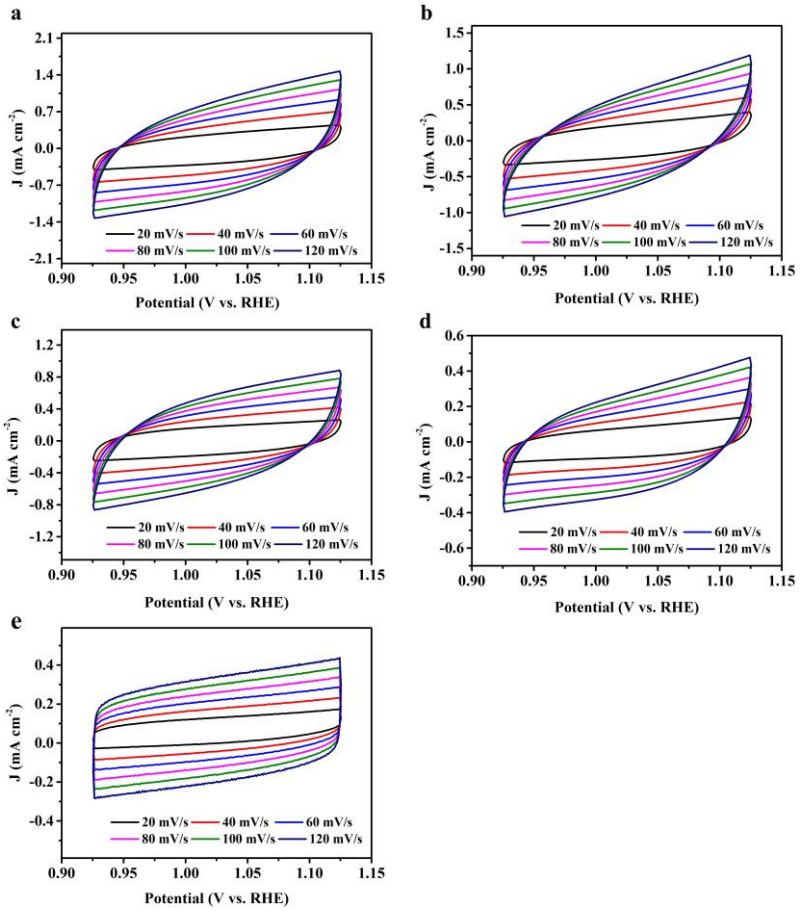

Supplementary Fig. 35. CV plots at various sweep rates. (a) *A*-$Fe_2S_1N_5$/SNC, (b) $Fe_1S_1N_3$/NC, (c) Fe_2N_6/NC, (d) Fe_1N_4/NC, and (e) SNC for OER.

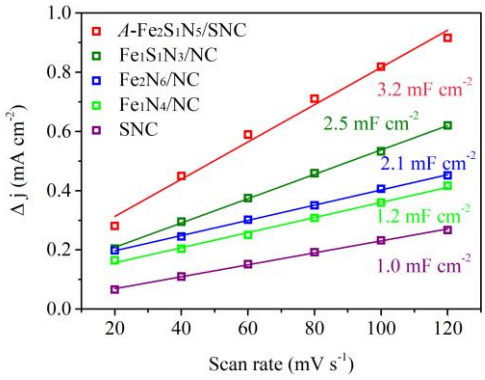

Supplementary Fig. 36. Calculated C_{dl} values of *A*-$Fe_2S_1N_5$/SNC, $Fe_1S_1N_3$/NC, Fe_2N_6/NC, Fe_1N_4/NC, and SNC.

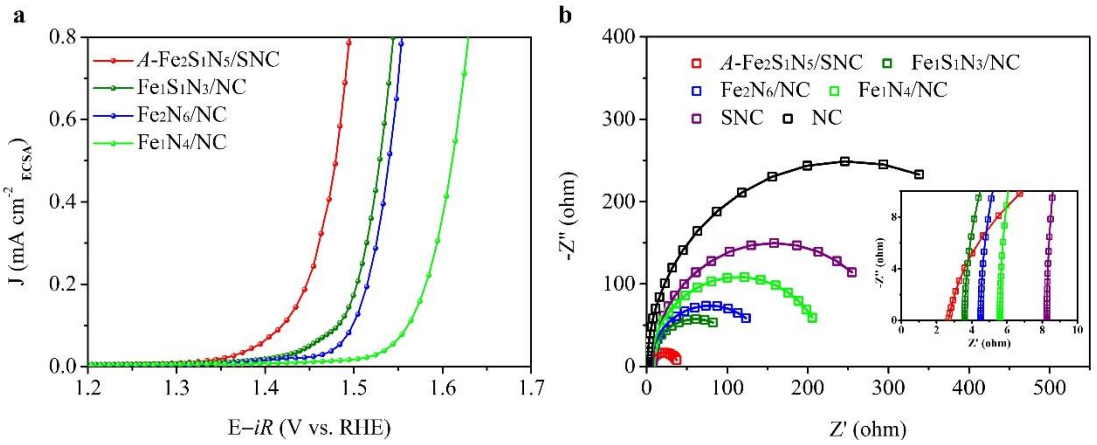

Supplementary Fig. 37. Performance characterization. (a) ECSA normalized LSV curves. (b) EIS curves of *A*-$Fe_2S_1N_5$/SNC, $Fe_1S_1N_3$/NC, Fe_2N_6/NC, Fe_1N_4/NC, and SNC at an overpotential of 10 mV. EIS shows the series resistance (*Rs*) of 2.7, 3.6, 4.5, 5.6, and 8.1 Ω for *A*-$Fe_2S_1N_5$/SNC, $Fe_1S_1N_3$/NC, Fe_2N_6/NC, Fe_1N_4/NC, and SNC, respectively.

The ECSA was determined by: ECSA = C_{dl}/C_s, where C_{dl} is double-layer capacitance and C_s is the specific capacitance of the sample. In this study, a general specific capacitance of $C_s = 0.035$ mF cm^{-2} was used based on the typical reported value.

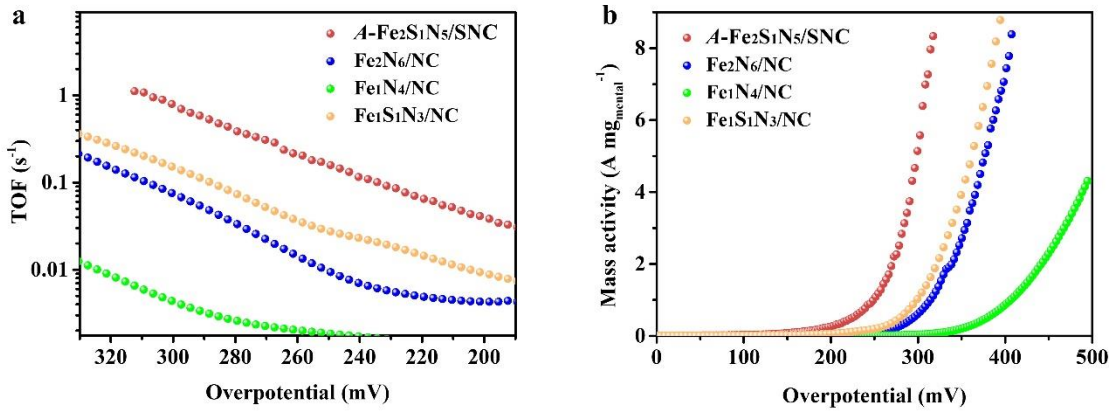

Supplementary Fig. 38. Performance characterization. (a) TOFs of the measured catalysts calculated based on the loaded Fe atoms at different overpotentials. (b) The mass activity of the measured catalysts was calculated based on the loaded Fe atoms at different overpotentials.

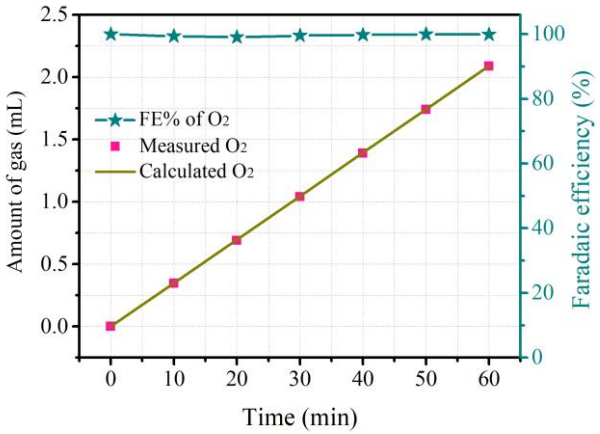

Supplementary Fig. 39. Experimental and theoretical volumes of generated O_2 and Faraday efficiency of *A*-$Fe_2S_1N_5$/SNC in 1.0 M KOH.

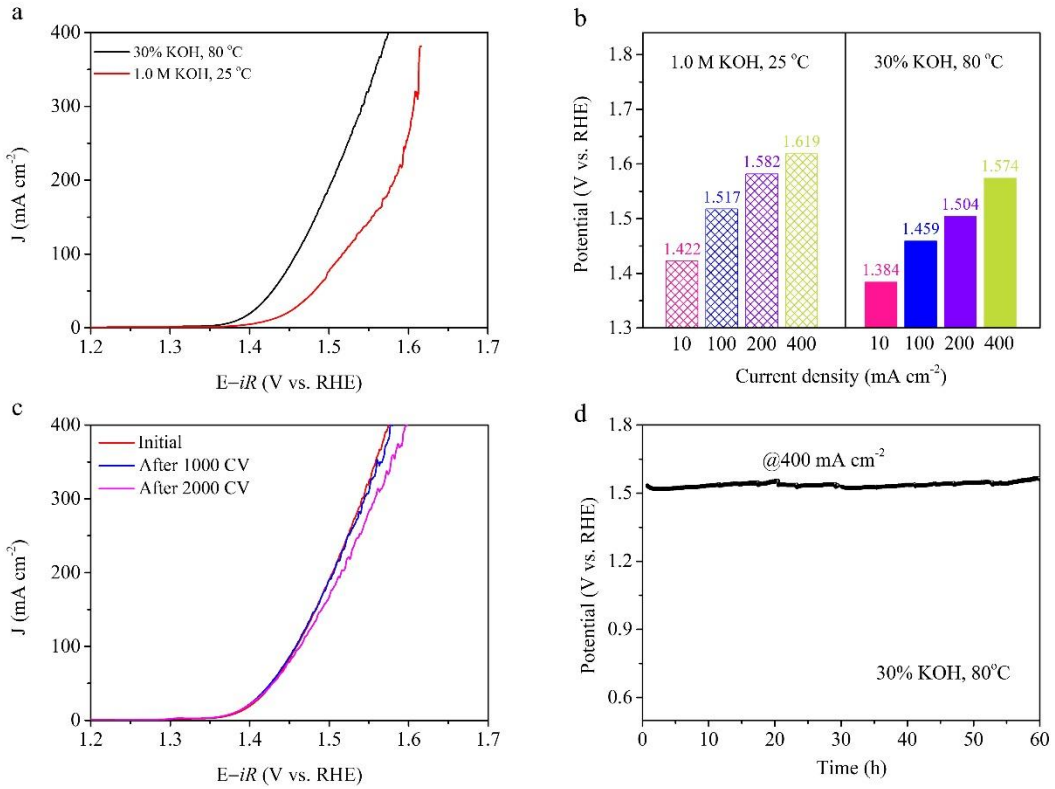

Supplementary Fig. 40. The catalytic performance of *A*-$Fe_2S_1N_5$/SNC under the industrial electrolytic water system. (a) LSV curves of the *A*-$Fe_2S_1N_5$/SNC electrode for water electrolysis in 30% KOH at 80 ℃ and 1.0 M KOH at 25 ℃. (b) Potentials for OER on the *A*-$Fe_2S_1N_5$/SNC electrode at current densities of 10, 100, 200, and 400 mA cm^{-2} in 30% KOH at 80 ℃. and 1.0 M KOH at 25 ℃, respectively. The results were carried out with 95% *iR*-compensation. (c) LSV curves for initial, 1000, and 2000 CV tests on the *A*-$Fe_2S_1N_5$/SNC catalyst in 30% KOH electrolyte at 80 ℃. (d) Chronpotentiometric curve at 400 mA cm^{-2} for the *A*-$Fe_2S_1N_5$/SNC electrode towards OER in 30% KOH at 80 ℃.

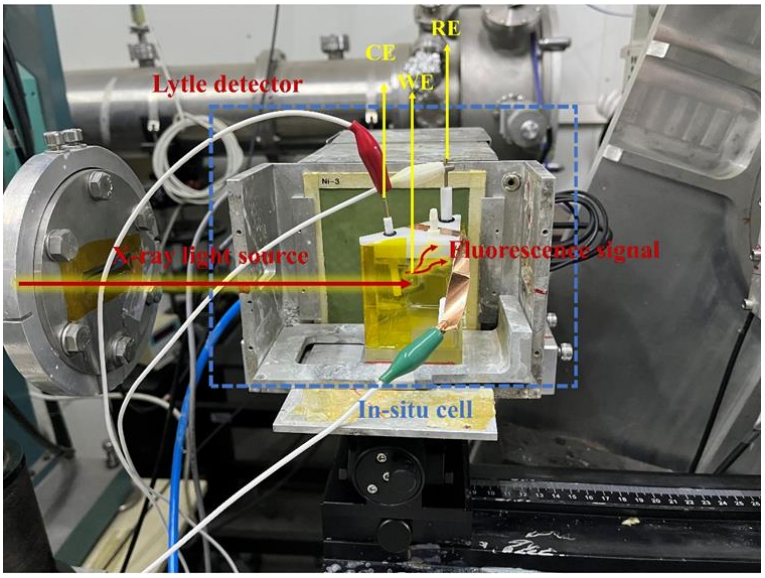

Supplementary Fig. 41. The detail of the *in-situ* X-ray absorption spectroscopy measurement. The device is set up at 14W1 beam line with the support from SSRF, where the X-ray induced fluorescence model is applied. CE, counter electrode; WE, working electrode; RE, reference electrode.

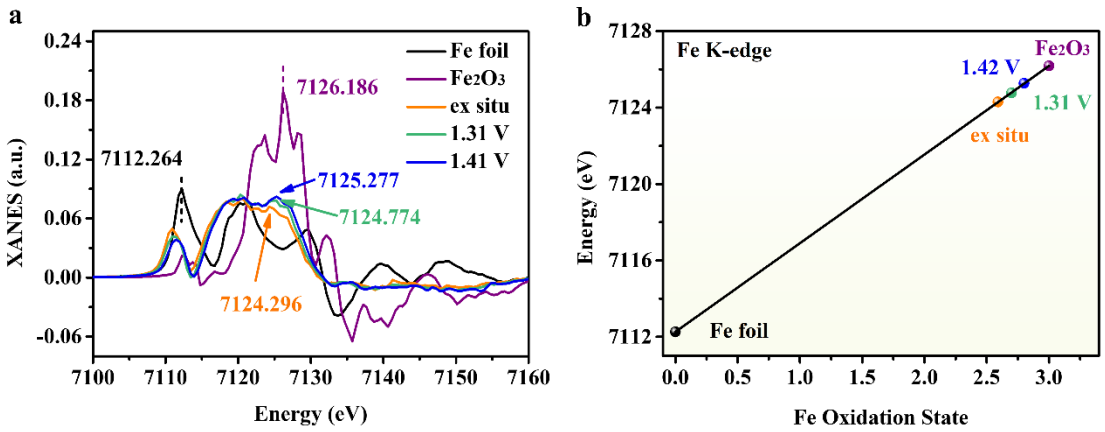

Supplementary Fig. 42. Structural characterization. (a) Corresponding first-derivative XANES curves at the Fe K-edge for OER. (b) The oxidation state of *A*-$Fe_2S_1N_5$/SNC at Fe K-edge for OER derived from (a).

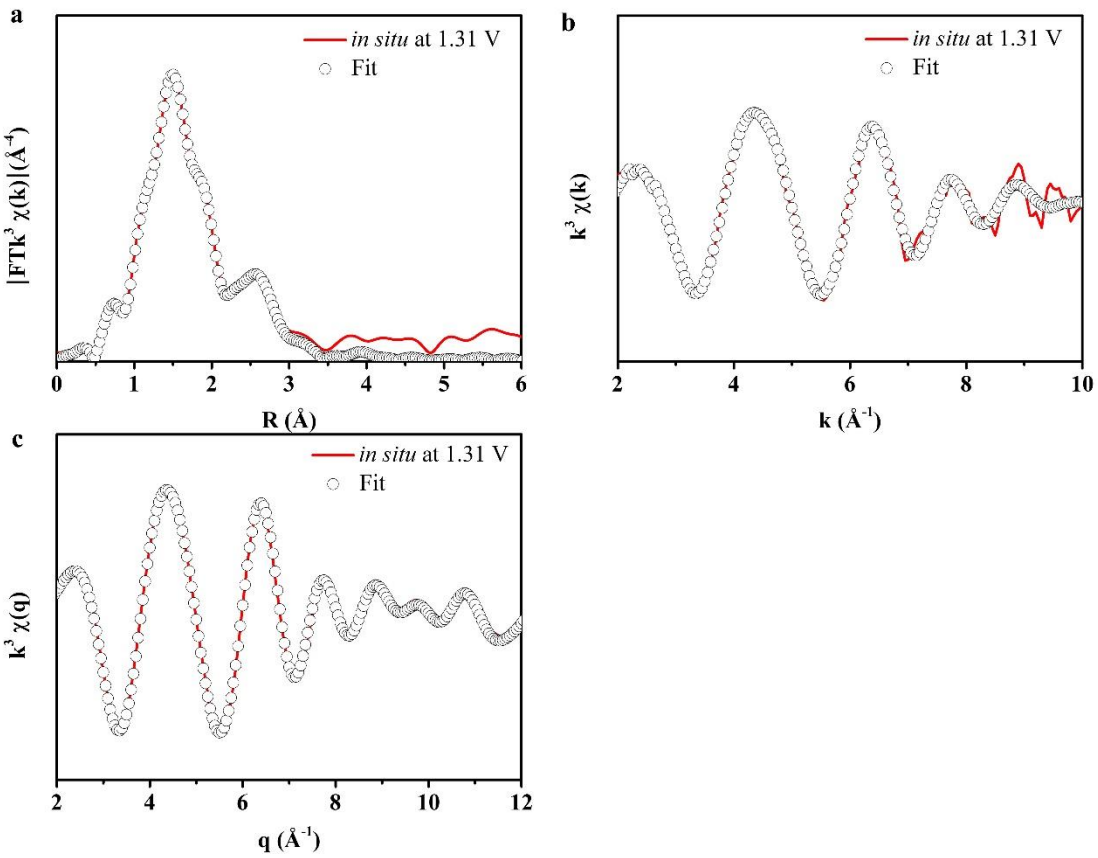

Supplementary Fig. 43. EXAFS fitting curves of *A*-$Fe_2S_1N_5$/SNC-in situ at 1.31 V.

(a) The FT-EXAFS fitting curve at Fe K-edge, (b) k space fitting curve, and (c) q space fitting curve.

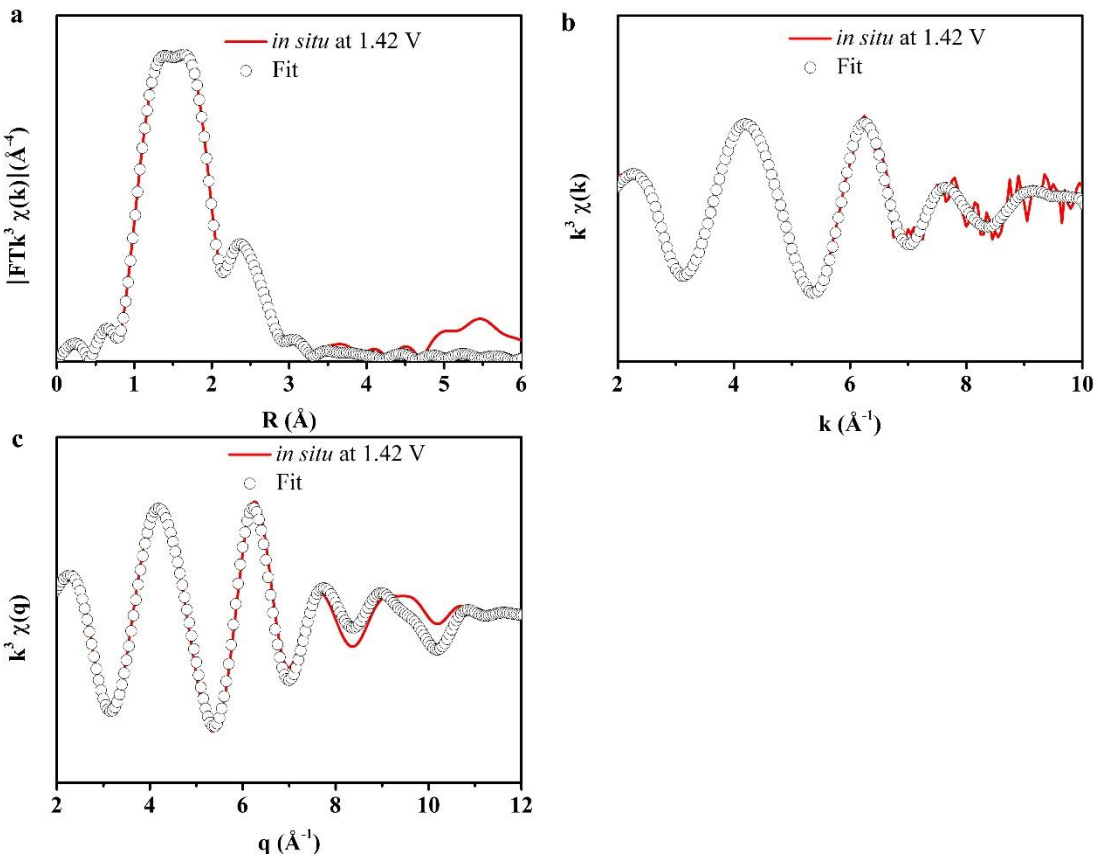

Supplementary Fig. 44. EXAFS fitting curves of *A*-$Fe_2S_1N_5$/SNC-in situ at 1.42 V.

(a) The FT-EXAFS fitting curve at Fe K-edge, (b) k space fitting curve, and (c) q space fitting curve.

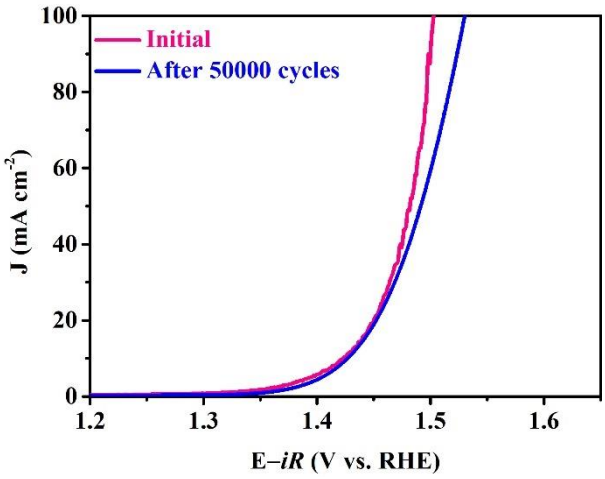

Supplementary Fig. 45. LSV curves before and after the 50000 CV stability test.

Note: the geometric surface area is 1.0 cm^2; series resistance (*Rs*) is 2.7 Ω.

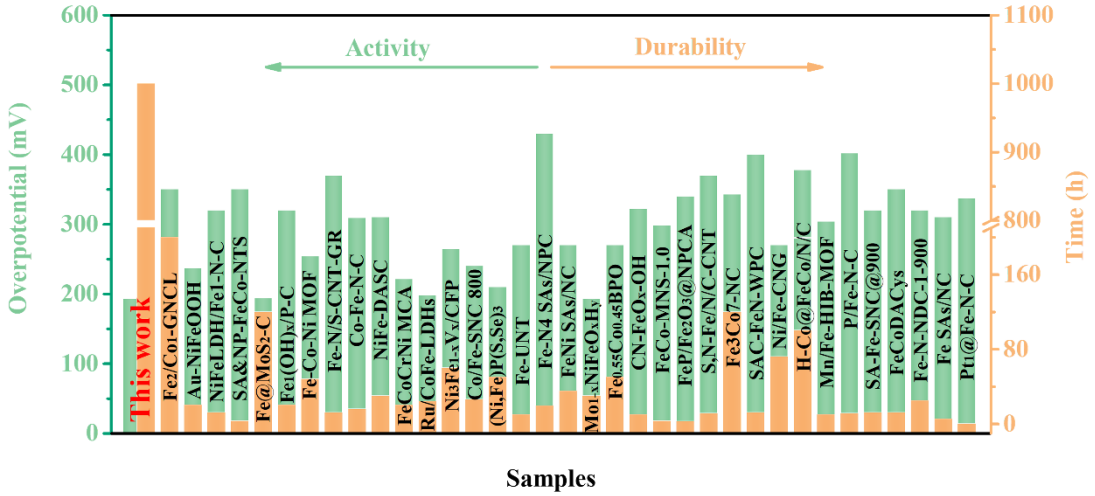

Supplementary Fig. 46. Summary of the long-term durability in water electrolysis for *A*-$Fe_2S_1N_5$/SNC and other reported electrocatalysts (**Supplementary Table 5**).

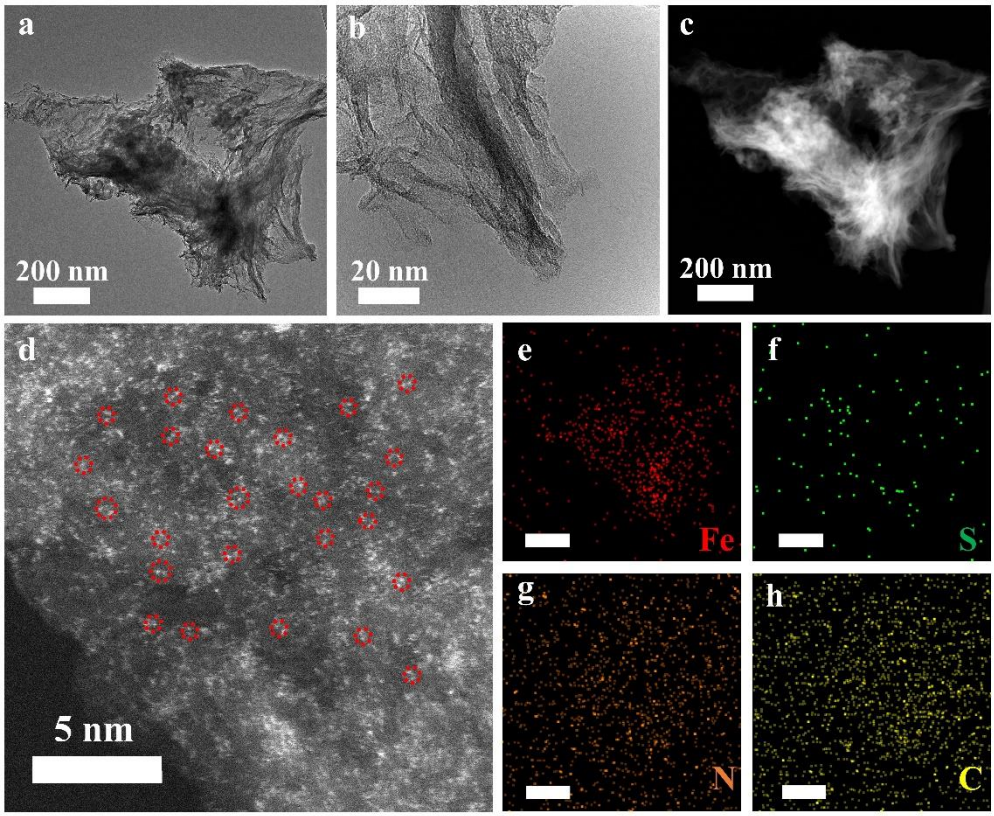

Supplementary Fig. 47. Morphology characterization of *A*-$Fe_2S_1N_5$/SNC after the 50000 cycles CV tests. (a-c) TEM, (d) Aberration-corrected HAADF-STEM, (e-h) EDS mapping images of Fe, S, N, and C. Scale bar: 200 nm.

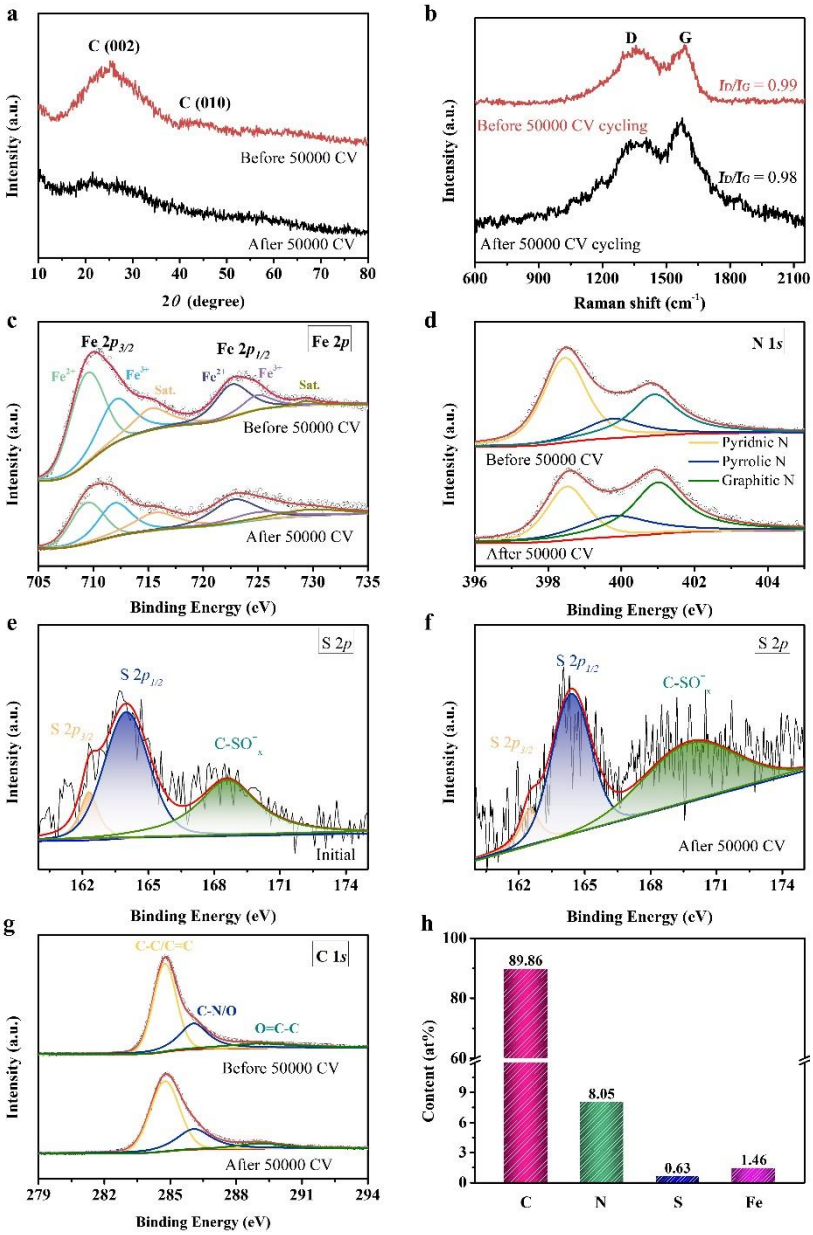

Supplementary Fig. 48. Structural characterization of *A*-$Fe_2S_1N_5$/SNC after the OER 50000 cycles CV test. (a) XRD pattern. (b) Raman pattern. XPS spectra for (c) Fe 2*p* and (d) N 1*s*. XPS spectra for S 2*p* of (e) before 50000 CV and (f) after 50000 CV. (g) C 1*s*. (h) The atomic content percentages of C, N, S, and Fe in *A*-$Fe_2S_1N_5$/SNC after OER cycling.

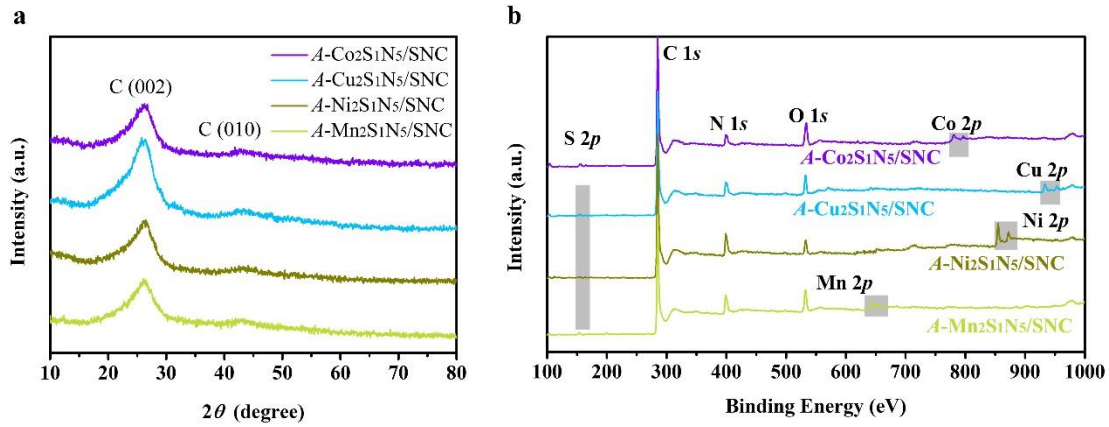

Supplementary Fig. 49. Component characterization. (a) XRD and (b) XPS survey spectrum of *A*-$Co_2S_1N_5$/SNC, *A*-$Cu_2S_1N_5$/SNC, *A*-$Ni_2S_1N_5$/SNC, and *A*-$Mn_2S_1N_5$/SNC.

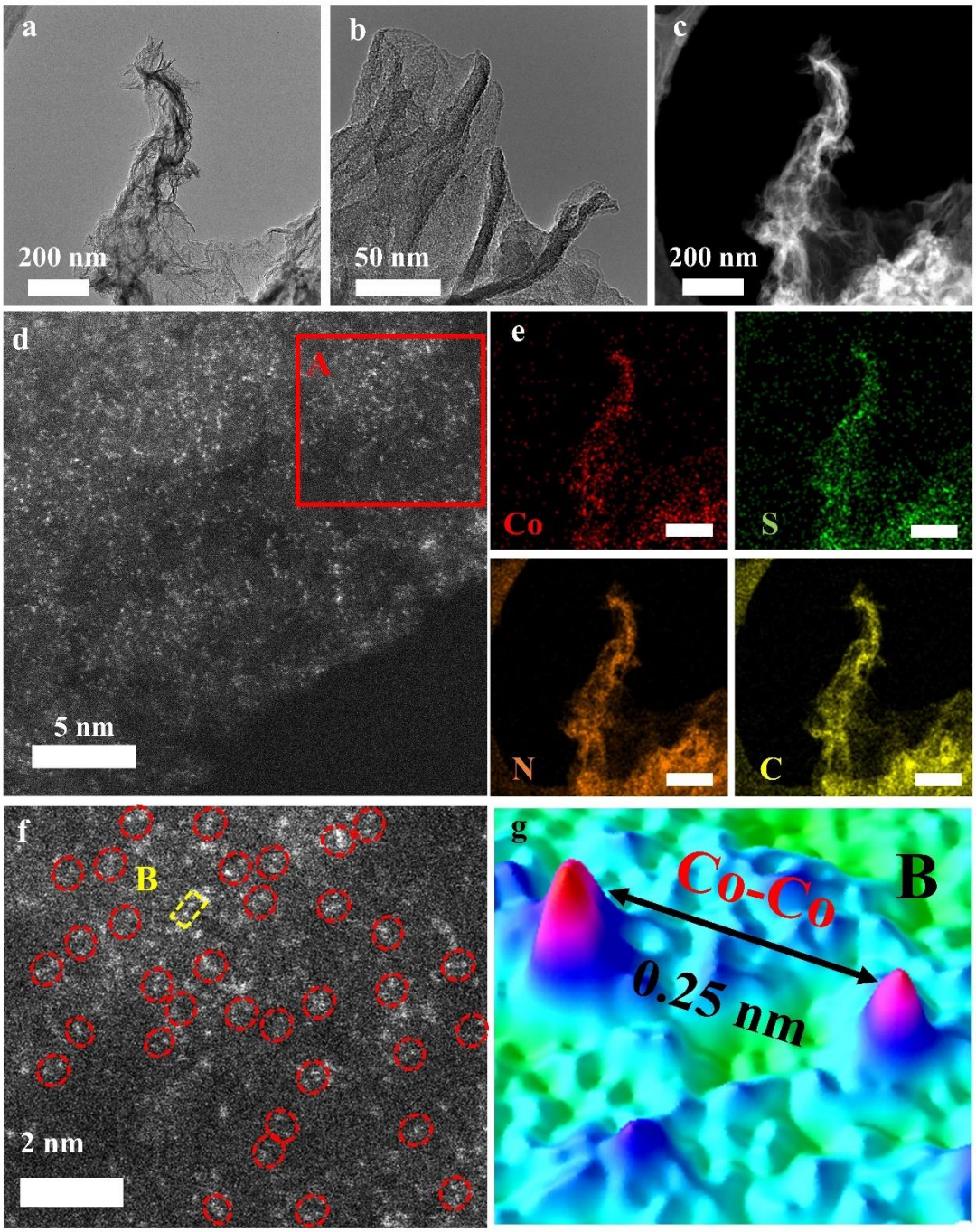

Supplementary Fig. 50. Morphology characterizations of *A*-$Co_2S_1N_5$/SNC. (a, b) TEM. (c) HAADF-STEM. (d, f) Aberration-corrected HAADF-STEM. (e) EDS mapping images of Co, S, N, and C. (g) statistical Co-Co distance in the observed diatomic pairs in region B of Figure (f). Scale bar: 200 nm.

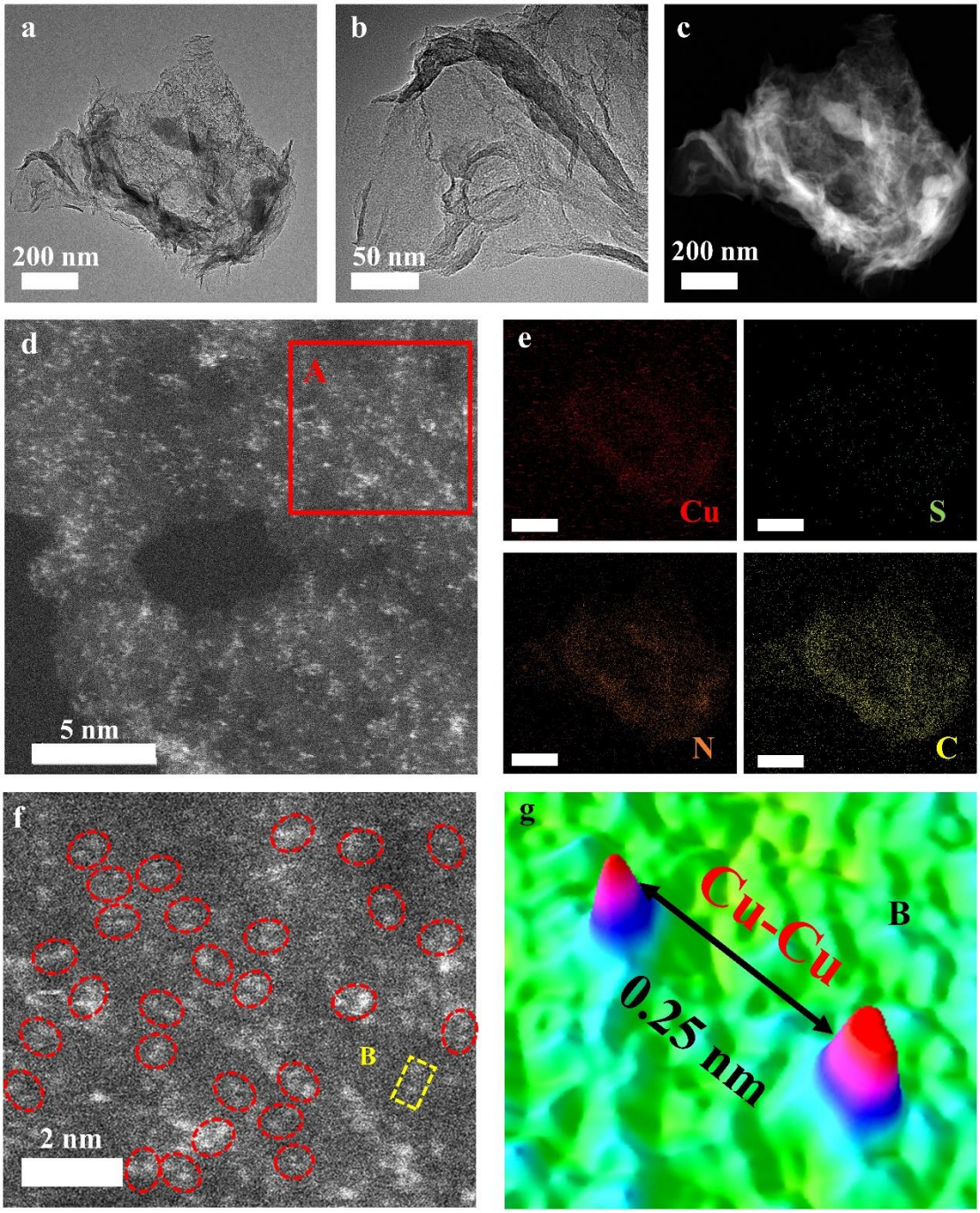

Supplementary Fig. 51. Morphology characterizations of *A*-$Cu_2S_1N_5$/SNC. (a, b) TEM. (c) HAADF-STEM. (d, f) Aberration-corrected HAADF-STEM. (e) EDS mapping images of Cu, S, N, and C. (g) statistical Cu-Cu distance in the observed diatomic pairs in region B of Figure (f). Scale bar: 200 nm.

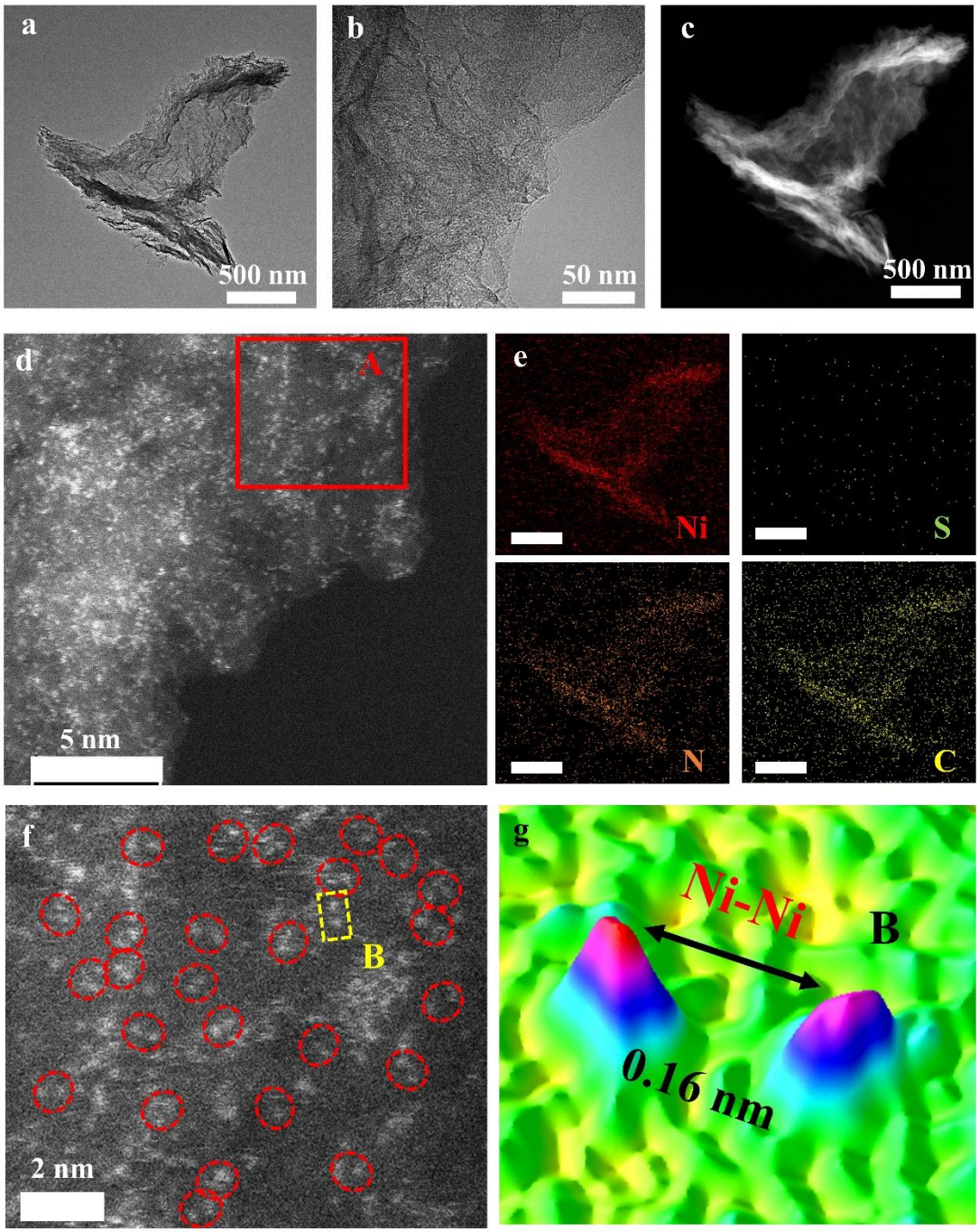

Supplementary Fig. 52. Morphology characterizations of *A*-$Ni_2S_1N_5$/SNC. (a, b) TEM. (c) HAADF-STEM. (d, f) Aberration-corrected HAADF-STEM. (e) EDS mapping images of Ni, S, N, and C. (g) statistical Ni-Ni distance in the observed diatomic pairs in region B of Figure (f). Scale bar: 500 nm.

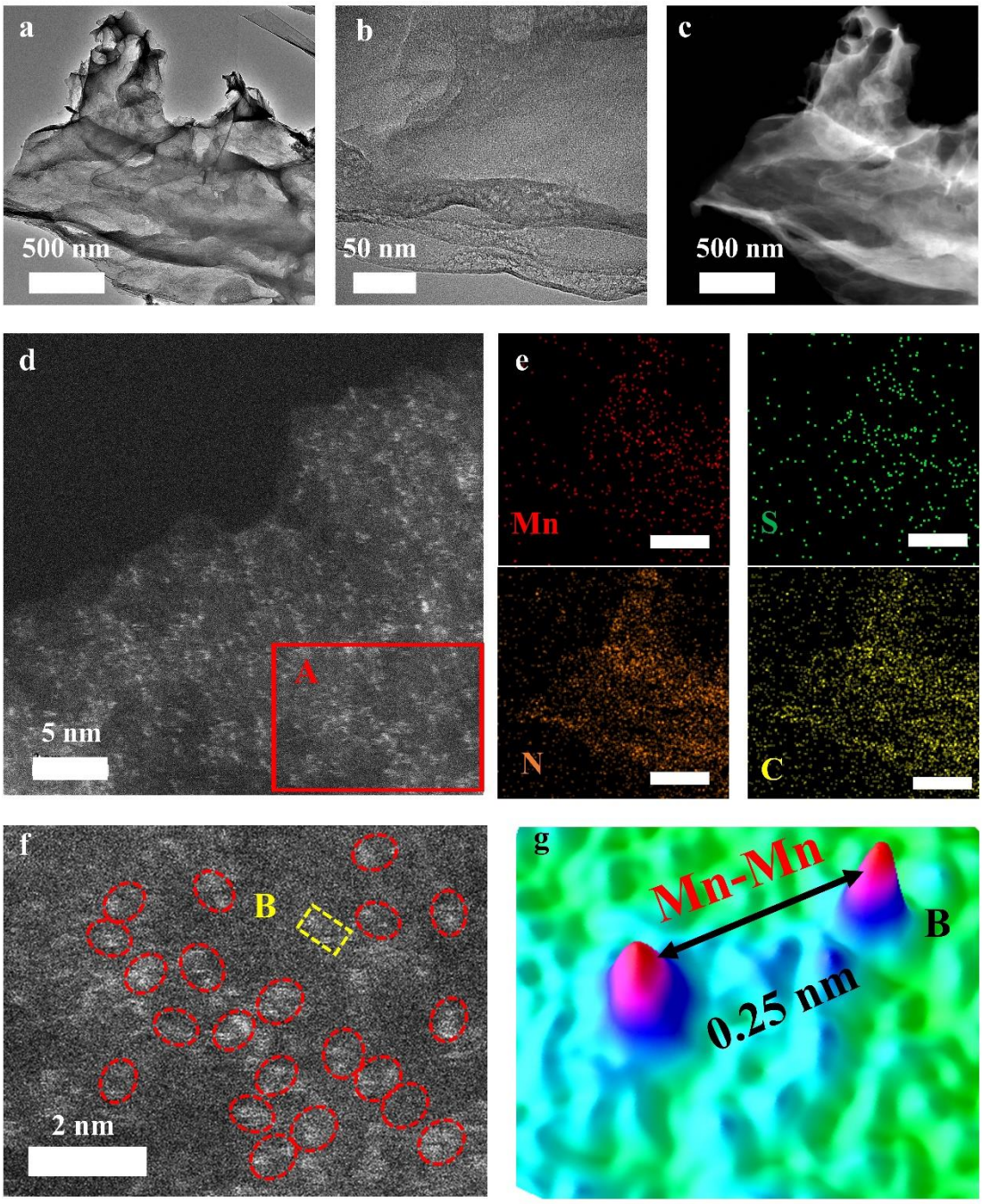

Supplementary Fig. 53. Morphology characterizations of *A*-$Mn_2S_1N_5$/SNC. (a, b) TEM. (c) HAADF-STEM. (d, f) Aberration-corrected HAADF-STEM. (e) EDS mapping images of Mn, S, N, and C. (g) statistical Mn-Mn distance in the observed diatomic pairs in region B of Figure (f). Scale bar: 500 nm.

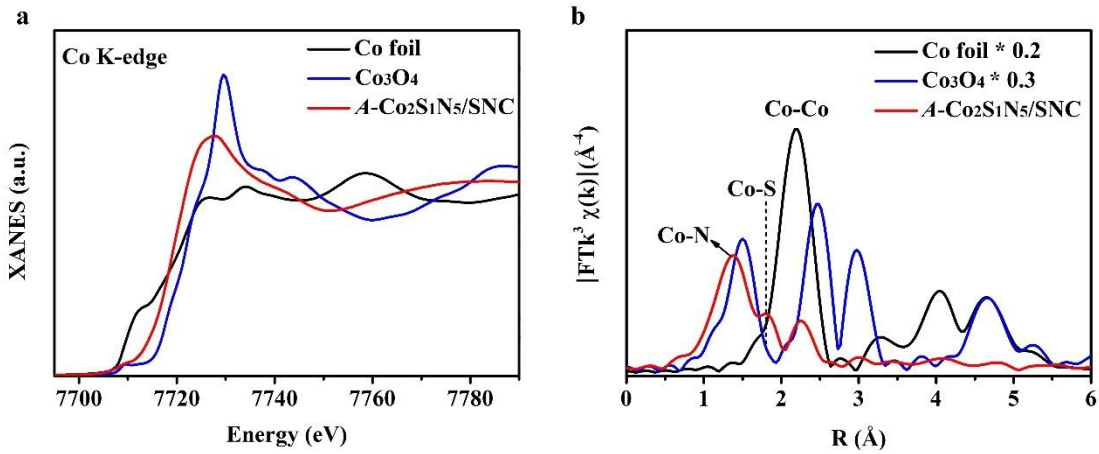

Supplementary Fig. 54. Atomic local structure characterizations. (a) XANES spectra at the Co K-edge of *A*-$Co_2S_1N_5$/SNC, Co_3O_4, and Co foil. (b) Fourier transforms (FT) at the Co K-edge of *A*-$Co_2S_1N_5$/SNC, Co_3O_4, and Co foil.

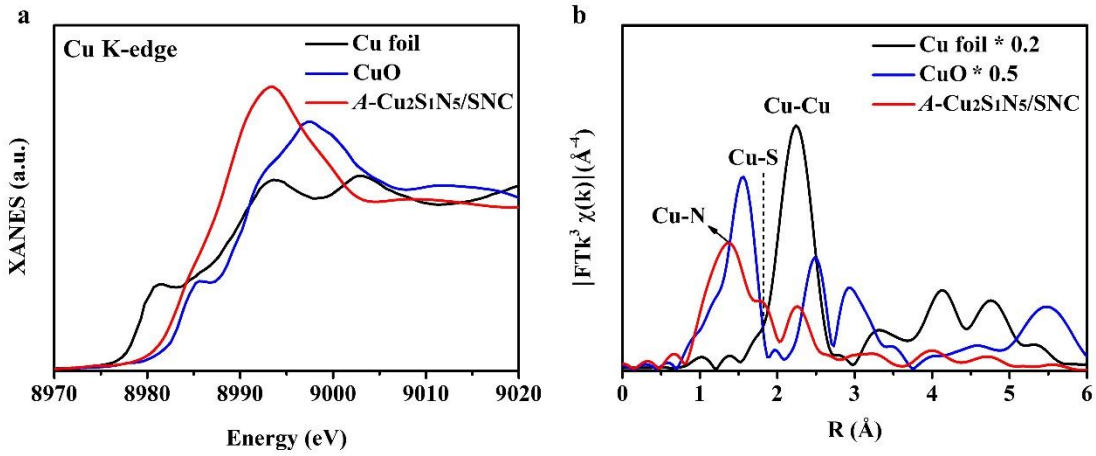

Supplementary Fig. 55. Atomic local structure characterizations. (a) XANES spectra at the Cu K-edge of *A*-$Cu_2S_1N_5$/SNC, CuO, and Cu foil. (b) Fourier transforms (FT) at the Cu K-edge of *A*-$Cu_2S_1N_5$/SNC, CuO, and Cu foil.

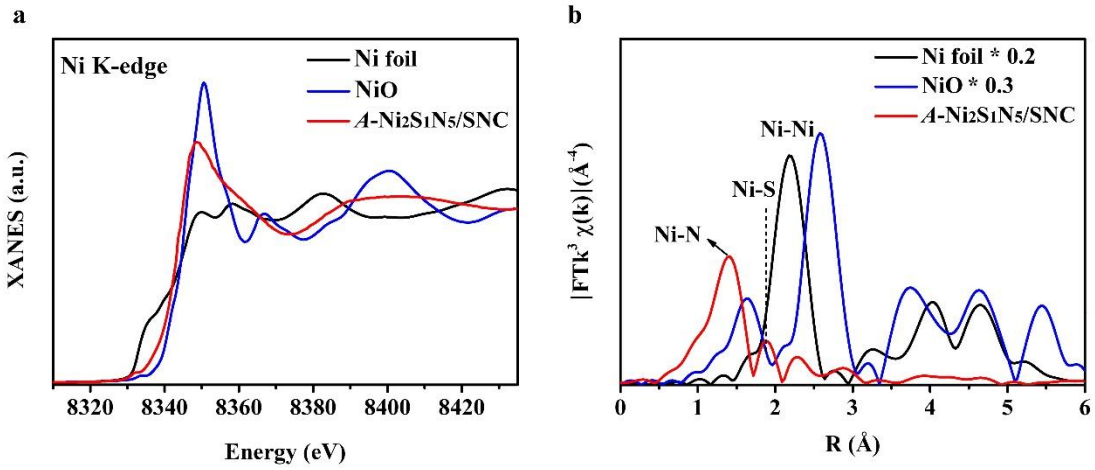

Supplementary Fig. 56. Atomic local structure characterizations. (a) XANES spectra at the Ni K-edge of *A*-$Ni_2S_1N_5$/SNC, NiO, and Ni foil. (b) Fourier transforms (FT) at the Ni K-edge of *A*-$Ni_2S_1N_5$/SNC, NiO, and Ni foil.

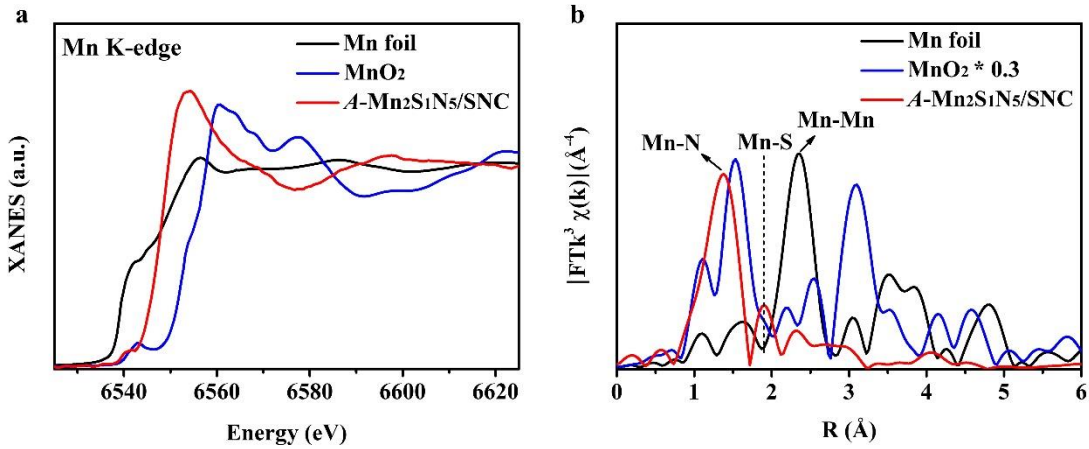

Supplementary Fig. 57. Atomic local structure characterizations. (a) XANES spectra at the Mn K-edge of *A*-$Mn_2S_1N_5$/SNC, MnO_2, and Mn foil. (b) Fourier transforms (FT) at the Mn K-edge of *A*-$Mn_2S_1N_5$/SNC, MnO_2, and Mn foil.

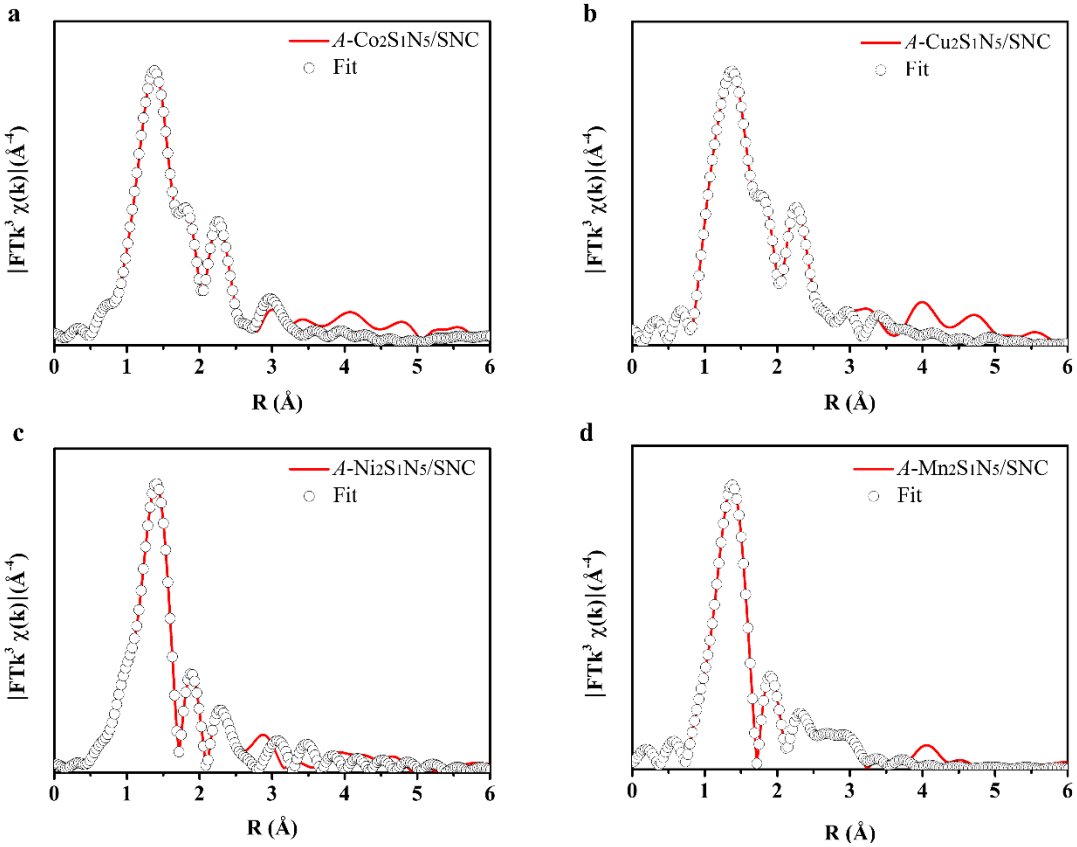

Supplementary Fig. 58 The FT-EXAFS fitting curve. (a) *A*-$Co_2S_1N_5$/SNC, (b) *A*-$Cu_2S_1N_5$/SNC, (c) *A*-$Ni_2S_1N_5$/SNC, and (d) *A*-$Mn_2S_1N_5$/SNC.

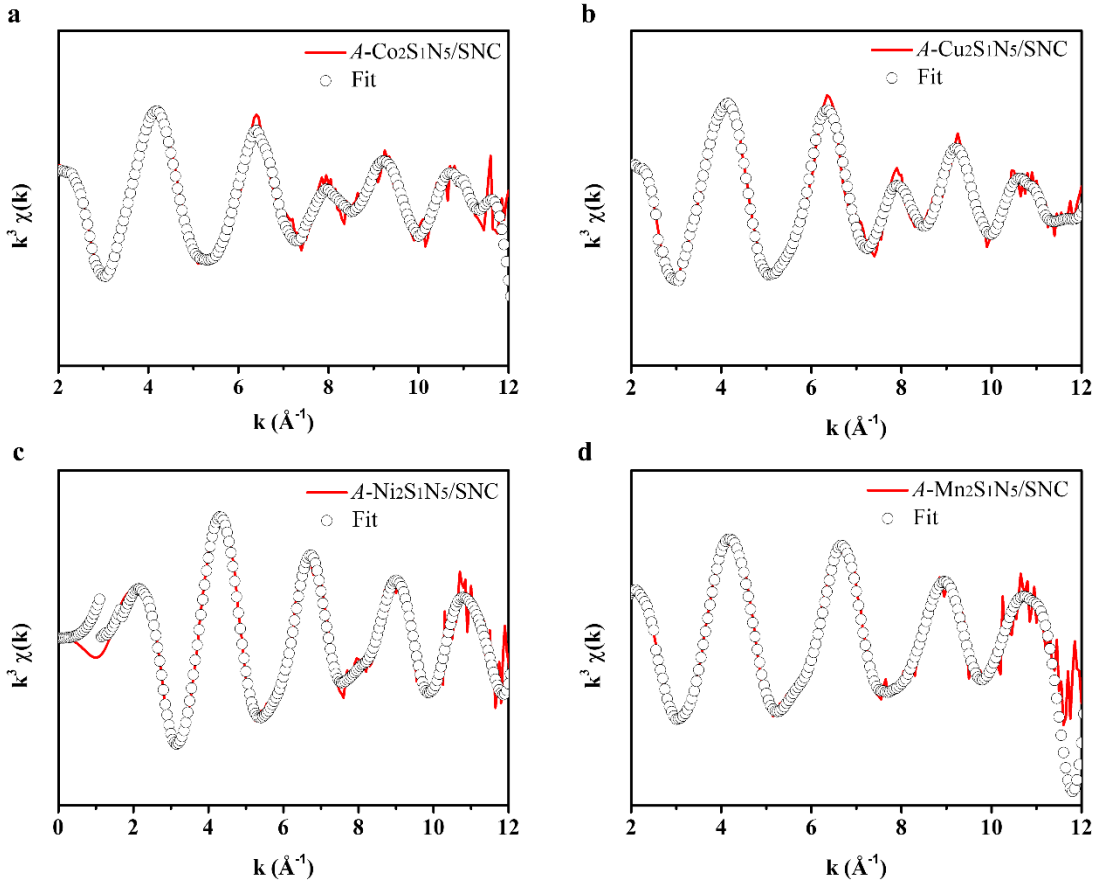

Supplementary Fig. 59. The *k* space fitting curve. (a) *A*-$Co_2S_1N_5$/SNC, (b) *A*-$Cu_2S_1N_5$/SNC, (c) *A*-$Ni_2S_1N_5$/SNC, and (d) *A*-$Mn_2S_1N_5$/SNC.

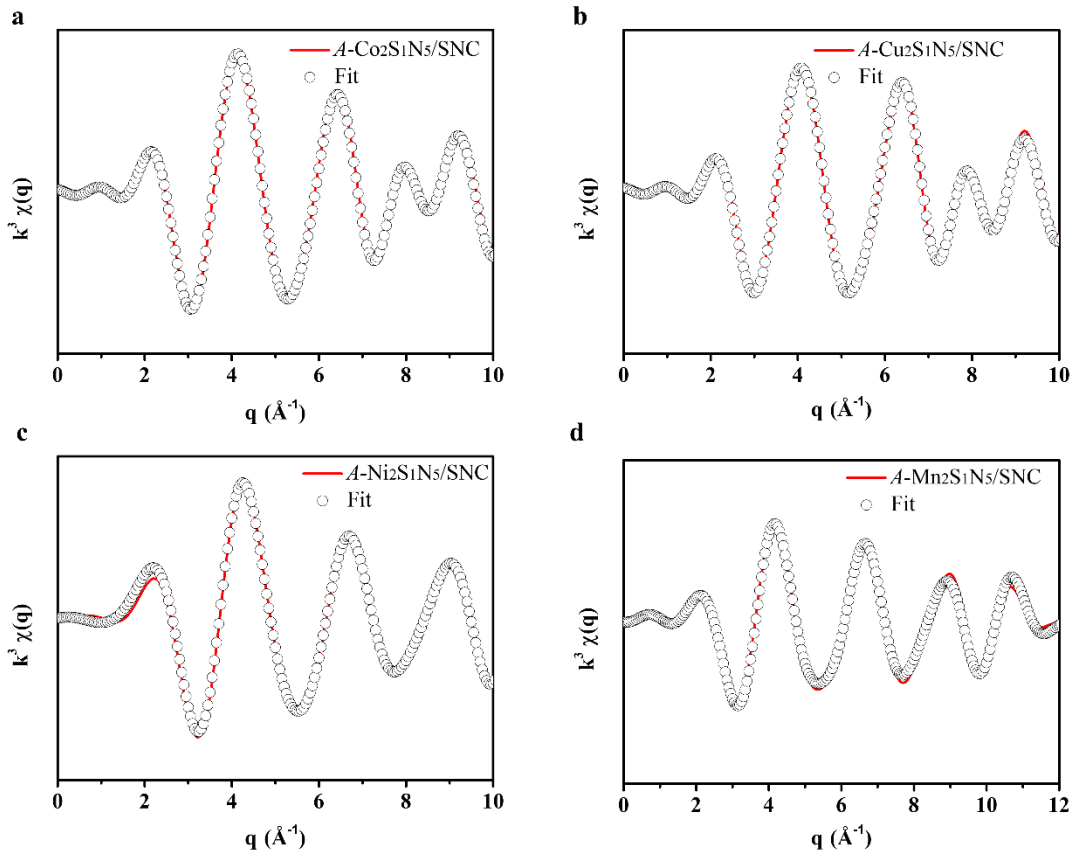

Supplementary Fig. 60. The *q* space fitting curve. (a) *A*-$Co_2S_1N_5$/SNC, (b) *A*-$Cu_2S_1N_5$/SNC, (c) *A*-$Ni_2S_1N_5$/SNC, and (d) *A*-$Mn_2S_1N_5$/SNC.

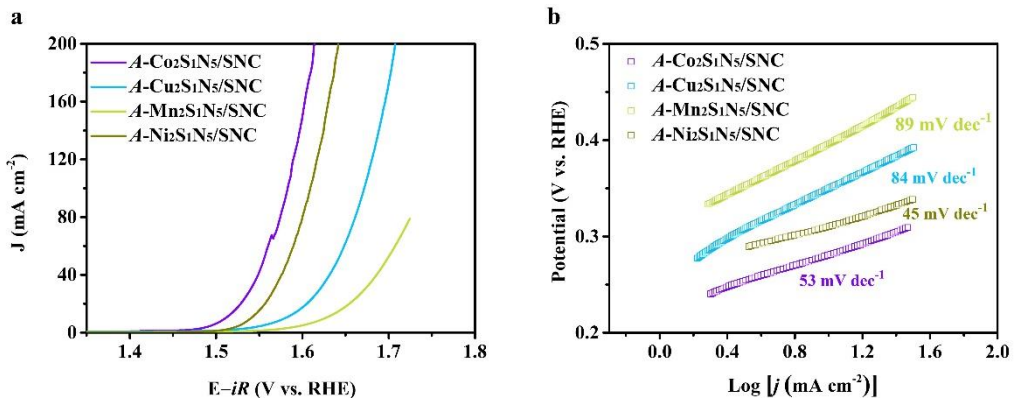

Supplementary Fig. 61. OER performance of *A*-$Co_2S_1N_5$/SNC, *A*-$Cu_2S_1N_5$/SNC, *A*-$Mn_2S_1N_5$/SNC, and *A*-$Ni_2S_1N_5$/SNC. (a) LSV curves, (b) Tafel slope.

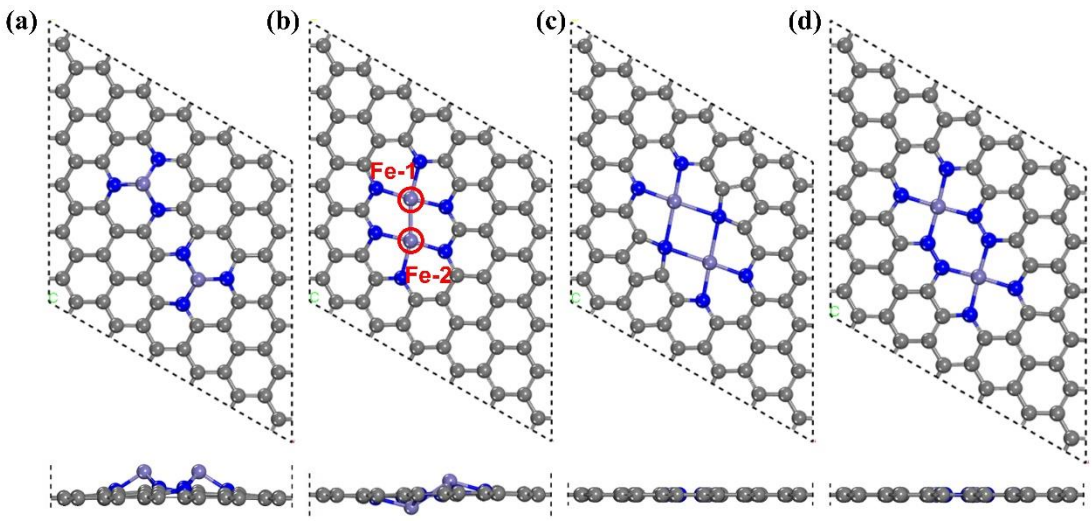

Supplementary Fig. S62 Four kinds of optimized diatomic Fe embedding into N-doped graphene: (a) Fe_2/N_3-6_1, (b) Fe_2/N_3-6_2, (c) Fe_2/N_4-6, and (d) Fe_2/N_4-8. The brown, blue, and gray balls mark Fe, N, and C atoms, respectively. The red circles indicate Fe-1 and Fe-2.

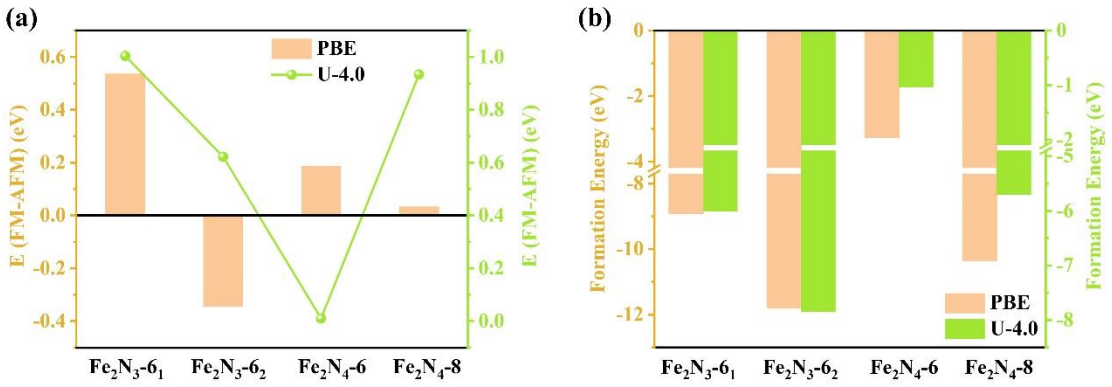

Supplementary Fig. 63. (a) The energy difference between FM (ferromagnetic) and AFM (antiferromagnetic) states in possible diatomic Fe embedding into N-doped graphene configurations using PBE functional with and without DFT+U (U = 4.0 for Fe atom) correction. Note that FM and AFM states are based on the initial magnetic state setting, after optimizing, the AFM state may be altered to be a ferrimagnetic state. (b) Their formation energies are based on the stable magnetic state.

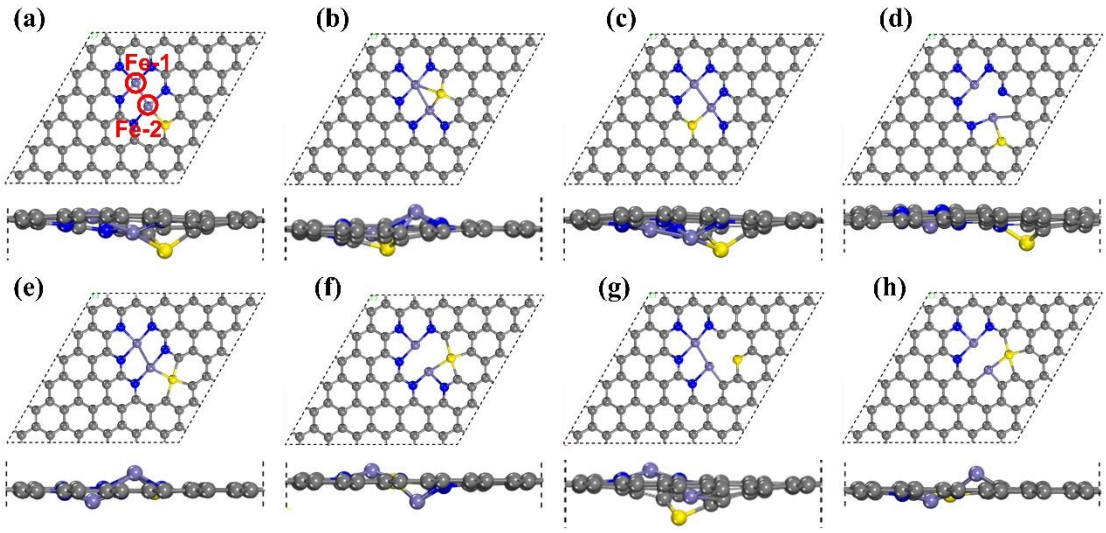

Supplementary Fig. 64. The optimized configurations of *A*-$Fe_2S_1N_5$/SNC in the 6×6 supercell of graphene (a-h). (a-c) Fe dimer displaces four carbon sites, coordinated by five nitrogen atoms and one sulfur atom with different carbon sites, named "1, 2, 3". (d-f) Fe dimer replacing five carbon sites, coordinating by five nitrogen atoms and sulfur atom with different carbon sites, named "4, 5, 6". (g, h) Fe dimer displacing five carbon sites, bonding with fewer nitrogen atoms with number four and three, named "7, 8". The Brown, blue, yellow, and gray balls indicate Fe, N, S, and C atoms, respectively. The red circle indicates Fe-1 (with three nitrogen atoms) and Fe-2 (with two nitrogen atoms and one sulfur atom).

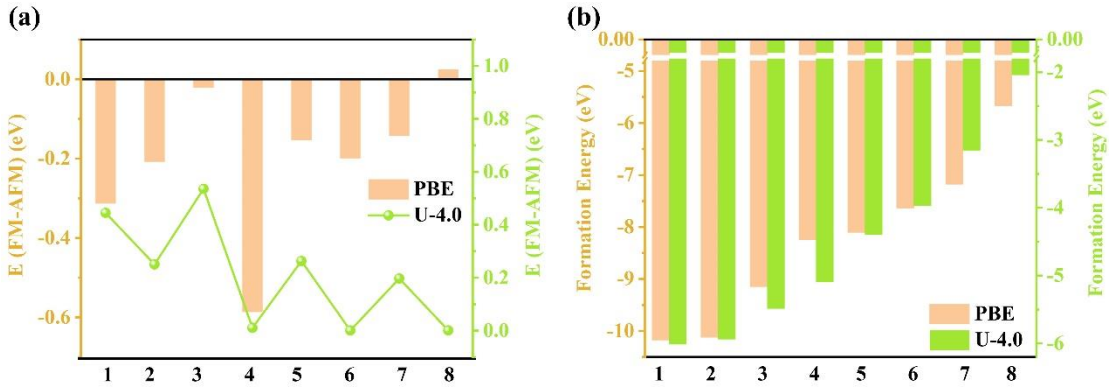

Supplementary Fig. 65. (a) The energy difference between FM (ferromagnetic) and AFM (antiferromagnetic) states in possible *A*-$Fe_2S_1N_5$/SNC configurations (named "1-8") using PBE functional with and without DFT+U (U = 4.0 for Fe atom) correction. Note that FM and AFM states are based on the initial magnetic state setting, after optimizing, the AFM state may be altered to be a ferrimagnetic state. (b) Their formation energies are based on the stable magnetic state.

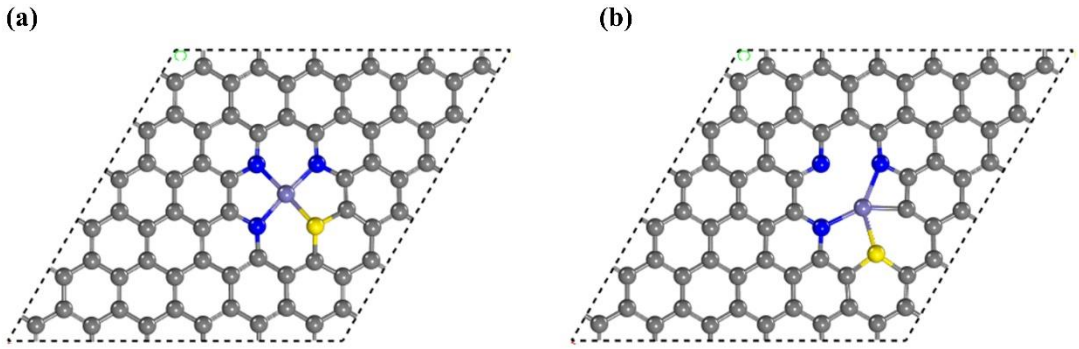

Supplementary Fig. 66. The possible configurations of $Fe_1S_1N_3$/NC single-atom catalyst with (a) $Fe_1S_1N_3$-1 and (b) $Fe_1S_1N_3$-2. The $Fe_1S_1N_3$-1 model possesses the lowest formation energy with -11.07 and -13. 38 eV by PBE functional with and without DFT + U correction.

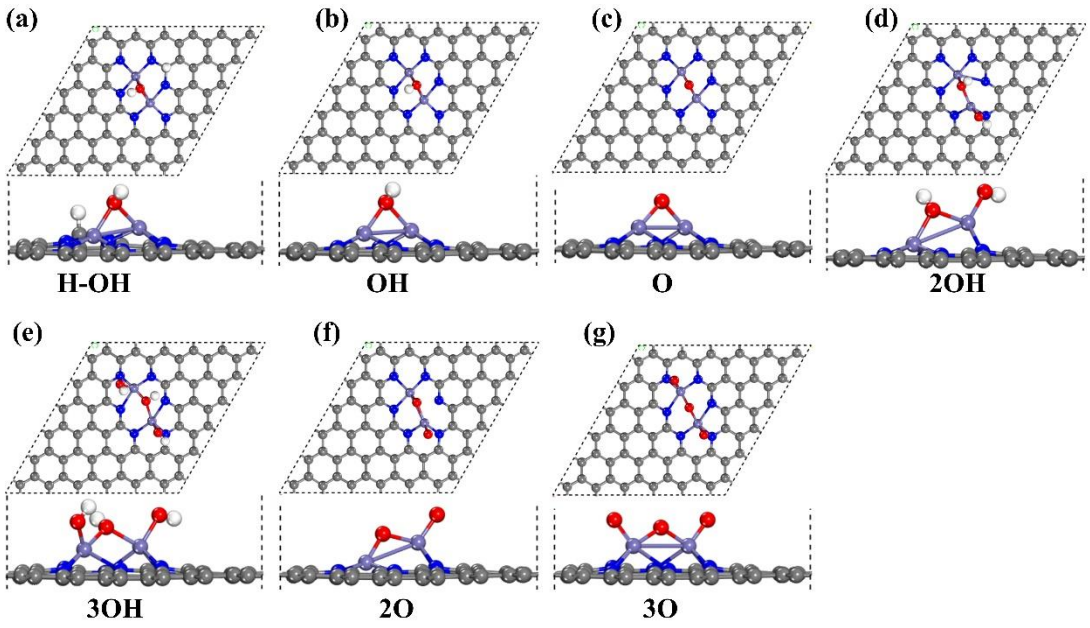

Supplementary Fig. 67. Optimized configurations with different H, OH, and O coverages on the Fe_2N_6/NC system. (a) H-OH, (b) OH, (c) O, (d) 2OH, (e) 3OH, (f) 2O, and (g) 3O overages on the Fe_2N_6/NC system. The brown, red, gray, blue, and white ball marks Fe, O, C, N, and H atoms, respectively.

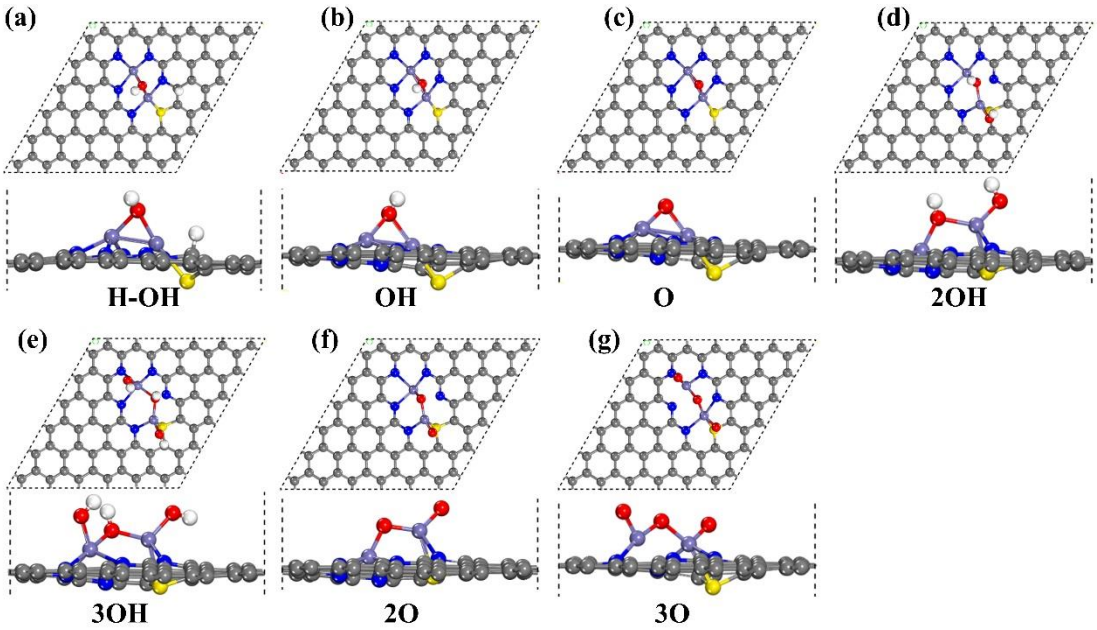

Supplementary Fig. 68. Optimized configurations with different H, OH, and O coverages on the *A*-$Fe_2S_1N_5$/SNC system. (a) H-OH, (b) OH, (c) O, (d) 2OH, (e) 3OH, (f) 2O, and (g) 3O overages on the *A*-$Fe_2S_1N_5$/SNC system. The brown, yellow, red, gray, blue, and white ball marks Fe, S, O, C, N, and H atoms, respectively.

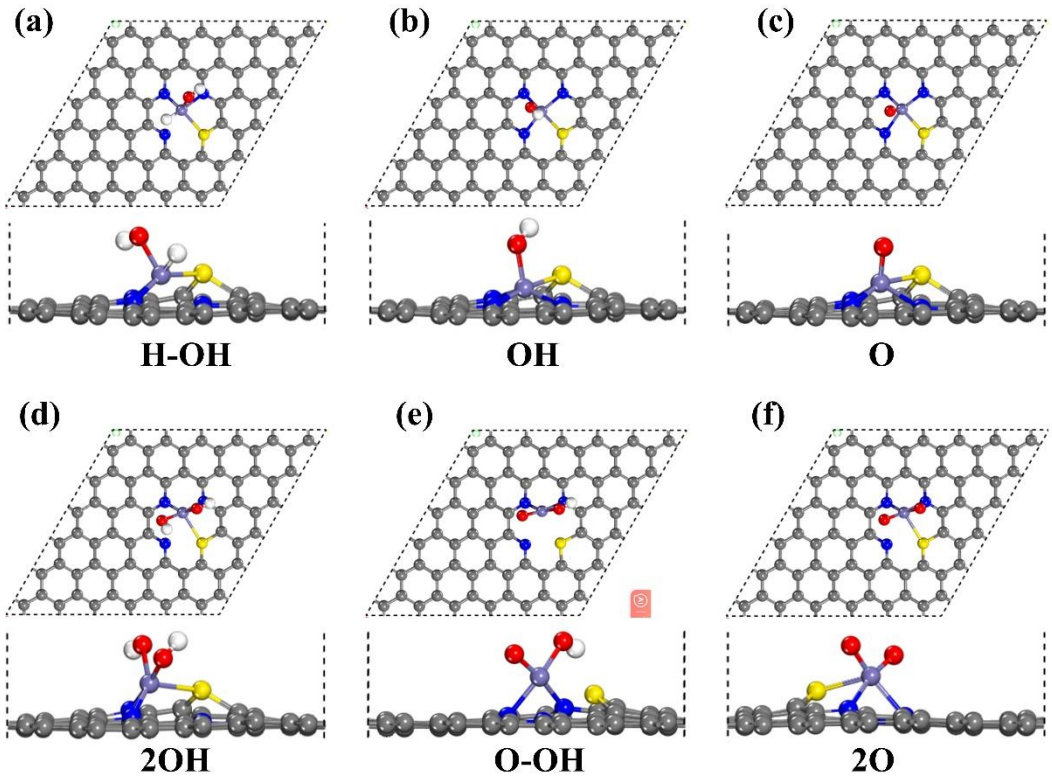

Supplementary Fig. 69. Optimized configurations of H, O, and OH coverage on the $Fe_1S_1N_3$/NC system. (a) H-OH, (b) OH, (c) O, (d) 2OH, (e) O-OH, and (g) 2O overages on the $Fe_1S_1N_3$/NC system. The brown, yellow, red, gray, blue, and white ball marks Fe, S, O, C, N, and H atoms, respectively.

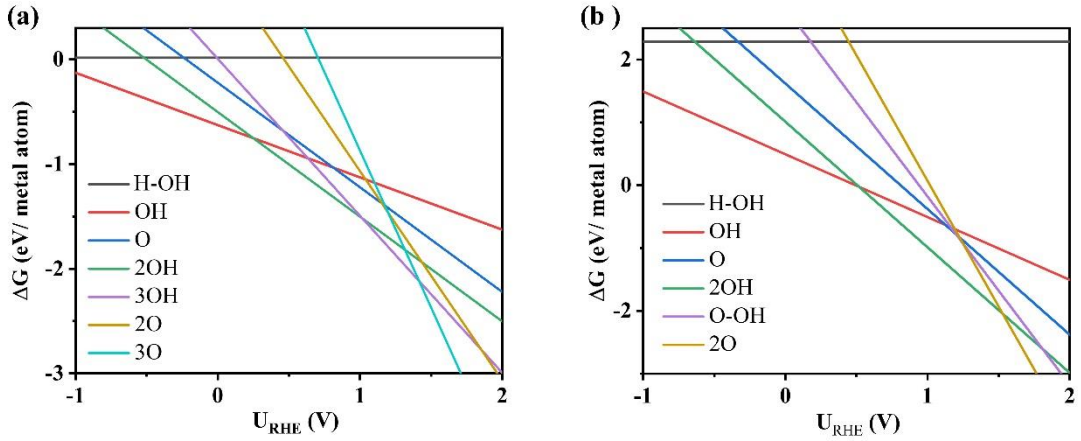

Supplementary Fig. 70. The free energy change of different intermediate coverages versus reversed hydrogen electrode potential on the bare (a) Fe_2N_6/NC and (b) $Fe_1S_1N_3$/NC catalysts.

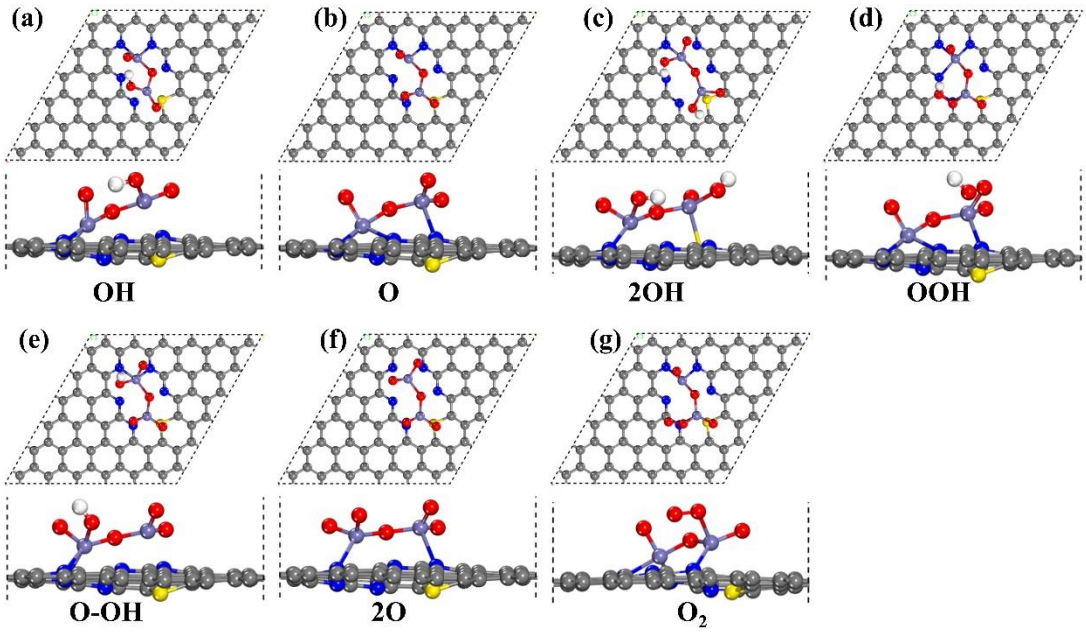

Supplementary Fig. 71. Optimized configurations of OER intermediates. (a) OH, (b) O, (c) 2OH, (d) OOH, (e) O-OH, (f) 2O, and (g) O_2 on the 3O-$Fe_2S_1N_5$/SNC system. The brown, yellow, red, gray, blue, and white ball marks Fe, S, O, C, N, and H atoms, respectively.

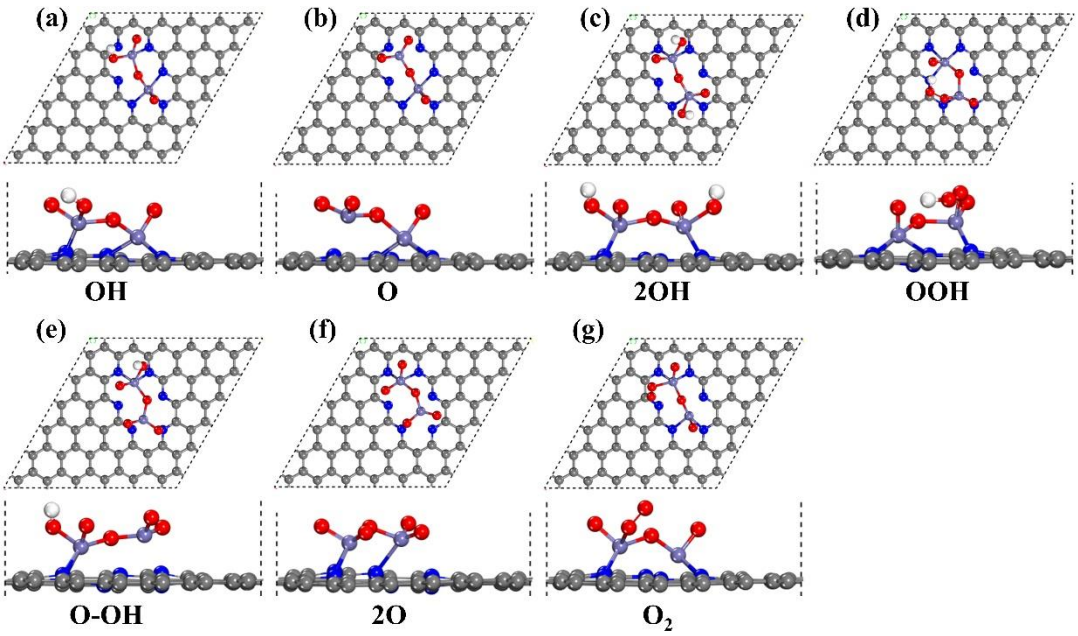

Supplementary Fig. 72. Optimized configurations of OER intermediates. (a) OH, (b) O, (c) 2OH, (d) OOH, (e) O-OH, (f) 2O, and (g) O_2 on the 3O-Fe_2N_6/NC system. The brown, red, gray, blue, and white ball marks Fe, O, C, N, and H atoms, respectively.

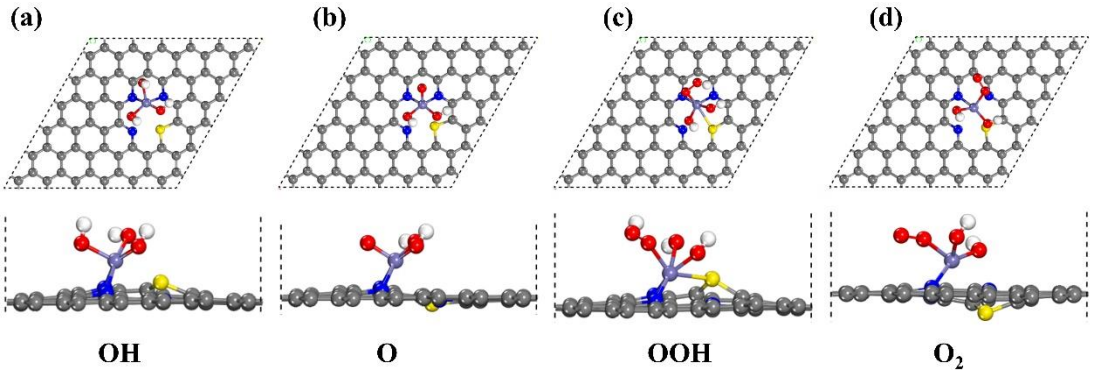

Supplementary Fig. 73. Optimized configurations of OER intermediates. (a) OH, (b) O, (c) OOH, and (d) O_2 on the 2OH-$Fe_1S_1N_3$/NC system. The brown, yellow, red, gray, blue, and white ball marks Fe, S, O, C, N, and H atoms, respectively.

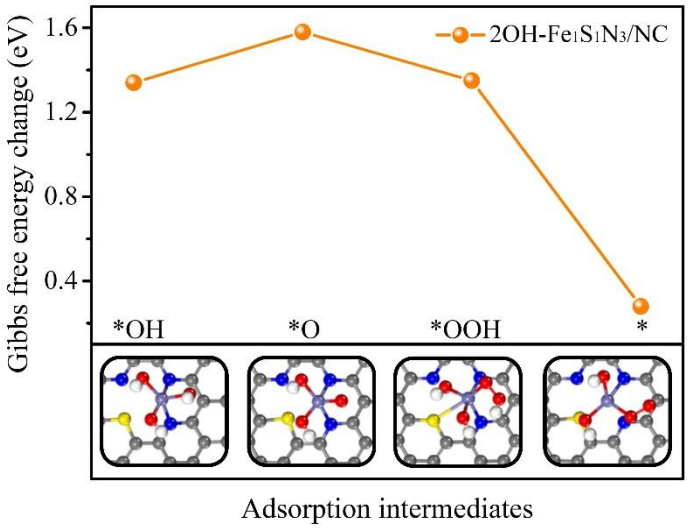

Supplementary Fig. 74. At U = 0 V, a comparison of Gibbs free energy changes of OER intermediates in $Fe_1S_1N_3$/NC.

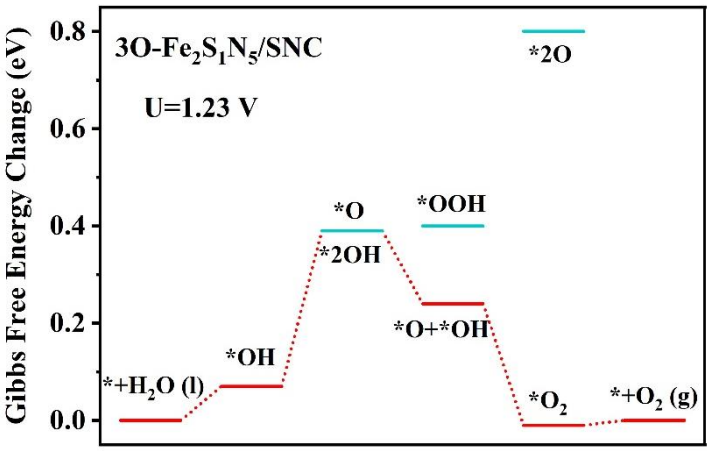

Supplementary Fig. 75. Gibbs free energy profiles of 3O-$Fe_2S_1N_5$/SNC under the potential of 1.23 V vs RHE. The conventional intermediates are represented in cyan, the unconventional ones are in red.

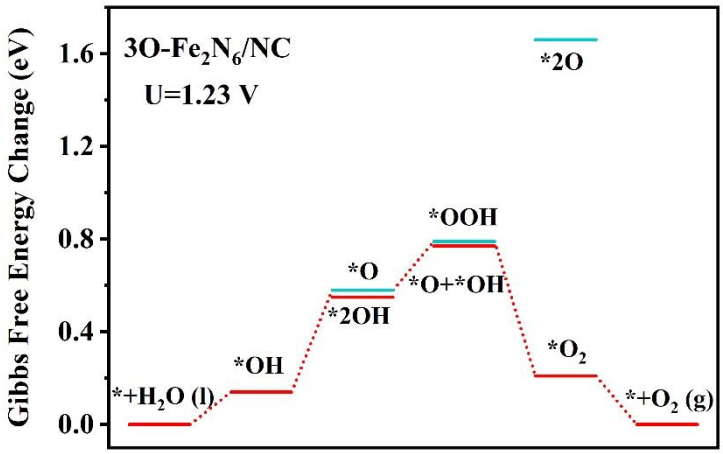

Supplementary Fig. 76. Gibbs free energy profiles of 3O-Fe_2N_6/NC under the potential of 1.23 V vs RHE. The conventional intermediates are represented in cyan, the unconventional ones are in red.

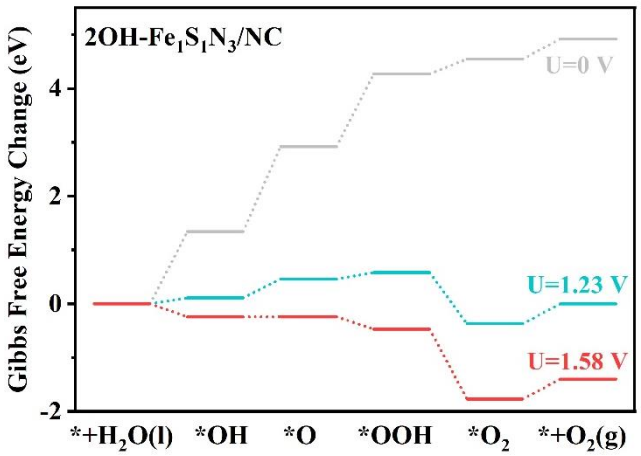

Supplementary Fig. 77. The free energy change of primary steps for OER on the 2OH-$Fe_1S_1N_3$/NC sites under the RHE with 0, 1.23, and 1.58 V. wherein the 1.23 V and 1.58 V indicate the equilibrium potential and the onset potential of OER, respectively.

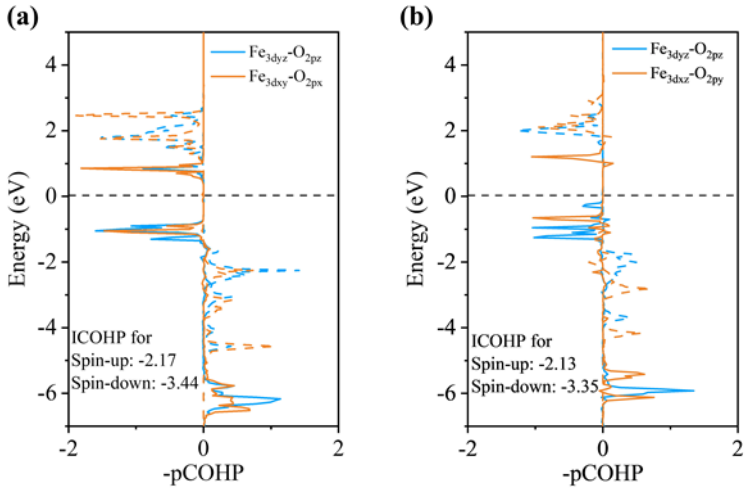

Supplementary Fig. 78. The pCOHP results with O-Fe bond of OER intermediate on the (a) 3O-$Fe_2S_1N_5$/SNC and (b) 3O-Fe_2N_6/NC systems. Solid and dashed line marks the spin-up and spin-down, respectively.

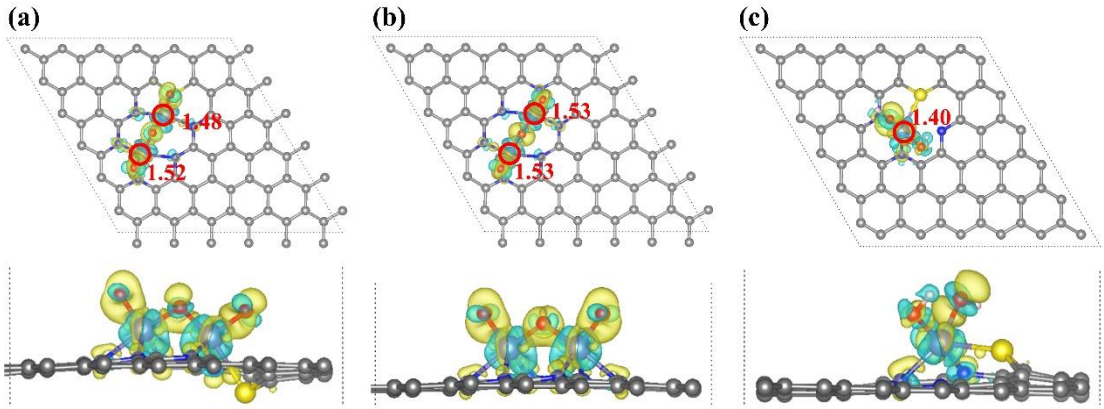

Supplementary Fig. 79. Differential charge density diagram. (a) *A*-$Fe_2S_1N_5$/SNC, (b) Fe_2N_6/NC, and (c) $Fe_1S_1N_3$/NC between Fe and SNC/NC substrates. The yellow and cyan contour with the isosurface value of 0.01 e/bohr^3 marks augmented and reduced charge density, respectively. The number indicates the localized charge of the Fe atom by the scheme of the Bader formula. The brown, gray, blue, yellow, red, and white balls indicate Fe, C, N, S, O, and H atoms, respectively.

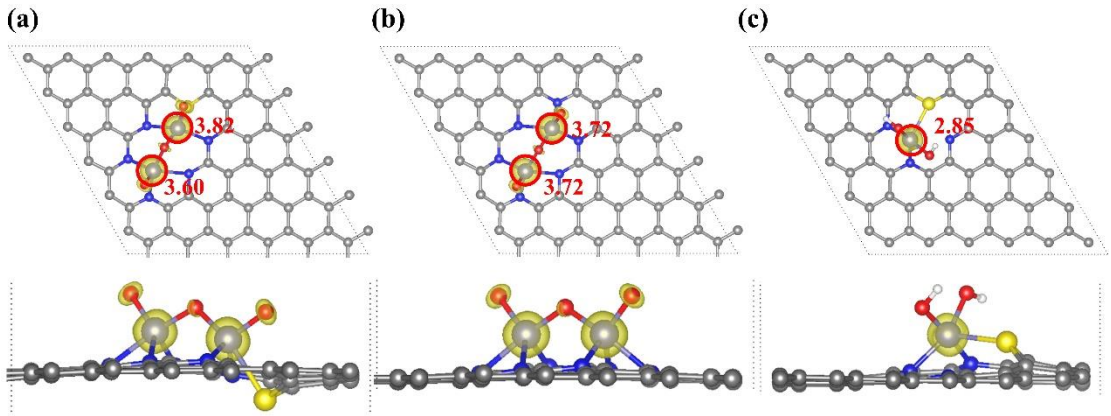

Supplementary Fig. 80. Spin charge density diagram. (a) *A*-$Fe_2S_1N_5$/SNC, (b) Fe_2N_6/NC, and (c) $Fe_1S_1N_3$/NC between Fe and SNC/NC substrates. The yellow contour with the isosurface value of 0.05 e/bohr^3 marks spin charge density, the number indicates the size of the magnetic moment. The brown, gray, blue, yellow, red, and white balls indicate Fe, C, N, S, O, and H atoms, respectively.

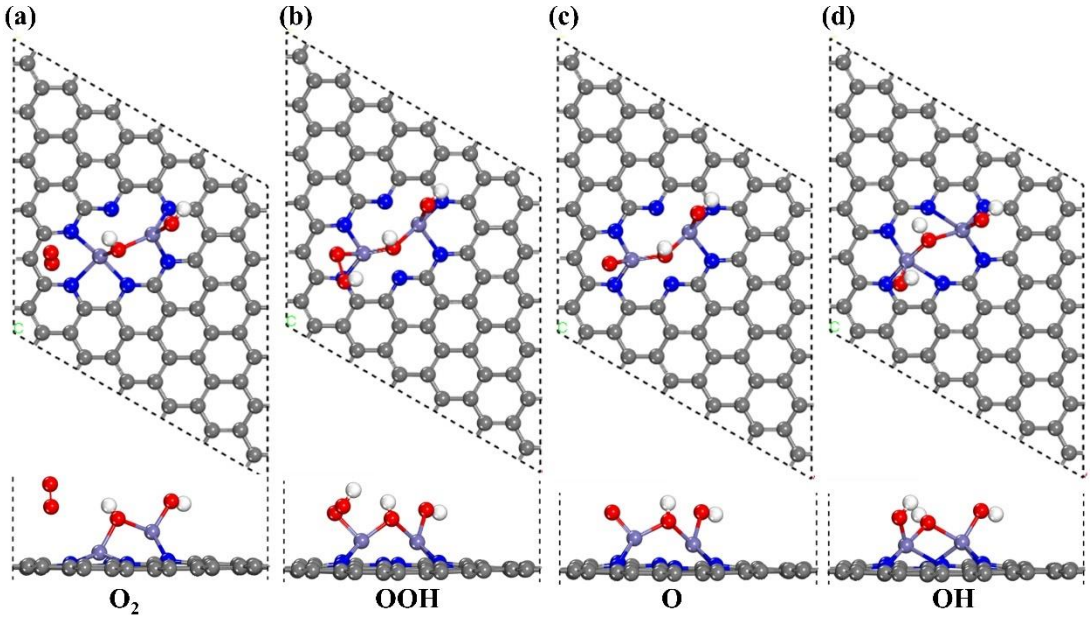

Supplementary Fig. 81. Optimized configurations of ORR intermediates. (a) O_2, (b) OOH, (c) O, and (d) OH on the 2OH-Fe_2N_6/NC system. The brown, red, gray, blue, and white ball marks Fe, O, C, N, and H atoms, respectively.

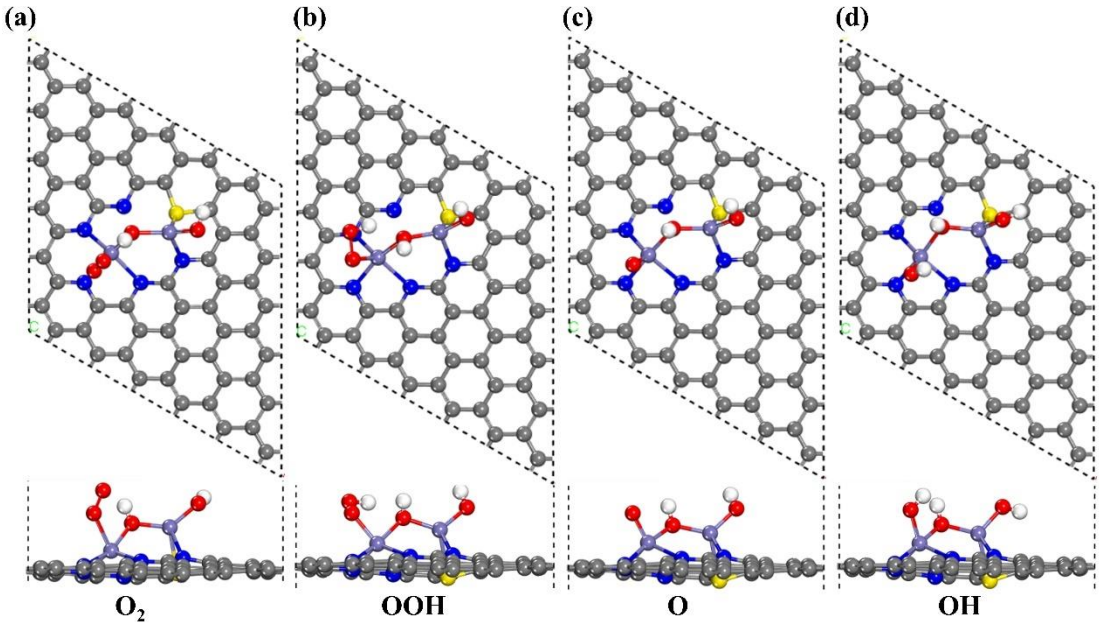

Supplementary Fig. 82. Optimized configurations of ORR intermediates. (a) O_2, (b) OOH, (c) O, and (d) OH on the 2OH-$Fe_2S_1N_5$/SNC system. The brown, yellow, red, gray, blue, and white ball marks Fe, S, O, C, N, and H atoms, respectively.

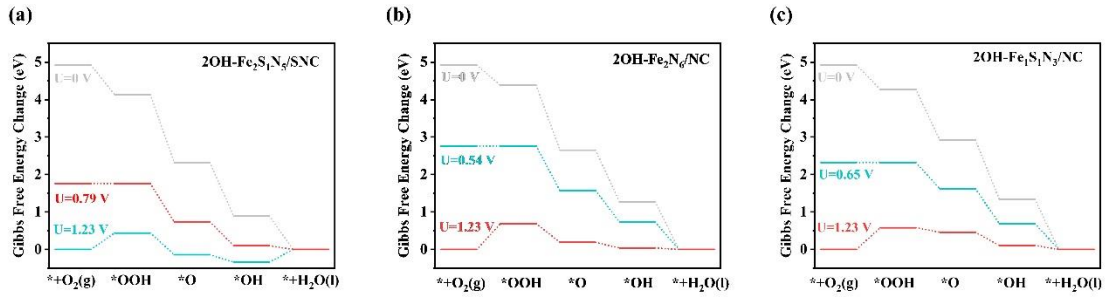

Supplementary Fig. 83. The free energy change profile of ORR mechanism. (a) 2OH-$Fe_2S_1N_5$/SNC, (b) 2OH-Fe_2N_6/NC, and (c) 2OH-$Fe_1S_1N_3$/NC.

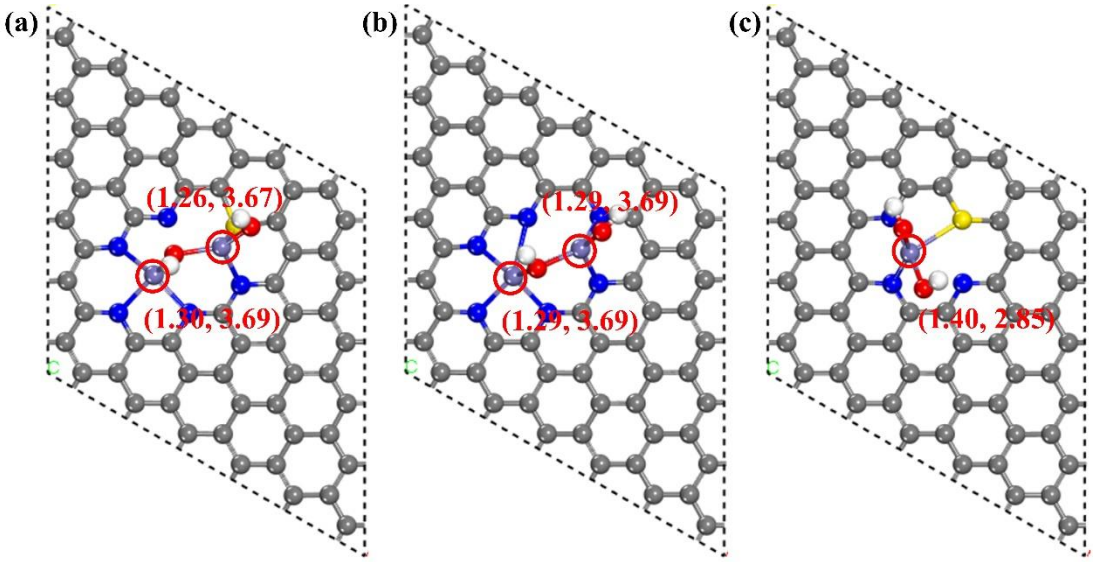

Supplementary Fig. 84. The charge and magnetic moment distribution of Fe atom. (a) 2OH-$Fe_2S_1N_5$/SNC, (b) 2OH-Fe_2N_6/NC, and (c) 2OH-$Fe_1S_1N_3$-NC. The former and latter number of the parenthesis marks the Bader charge and magnetic moment, respectively. The brown, gray, blue, yellow, red, and white balls indicate Fe, C, N, S, O, and H atoms, respectively.

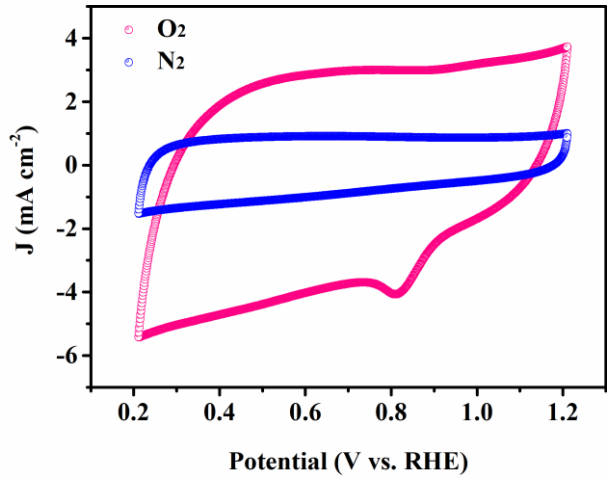

Supplementary Fig. 85. CV test in different atmospheres. (a) CV curves of *A*-$Fe_2S_1N_5$/SNC in O_2- and N_2-saturated 0.1 M KOH electrolyte at a scan rate of 50 mV/s.

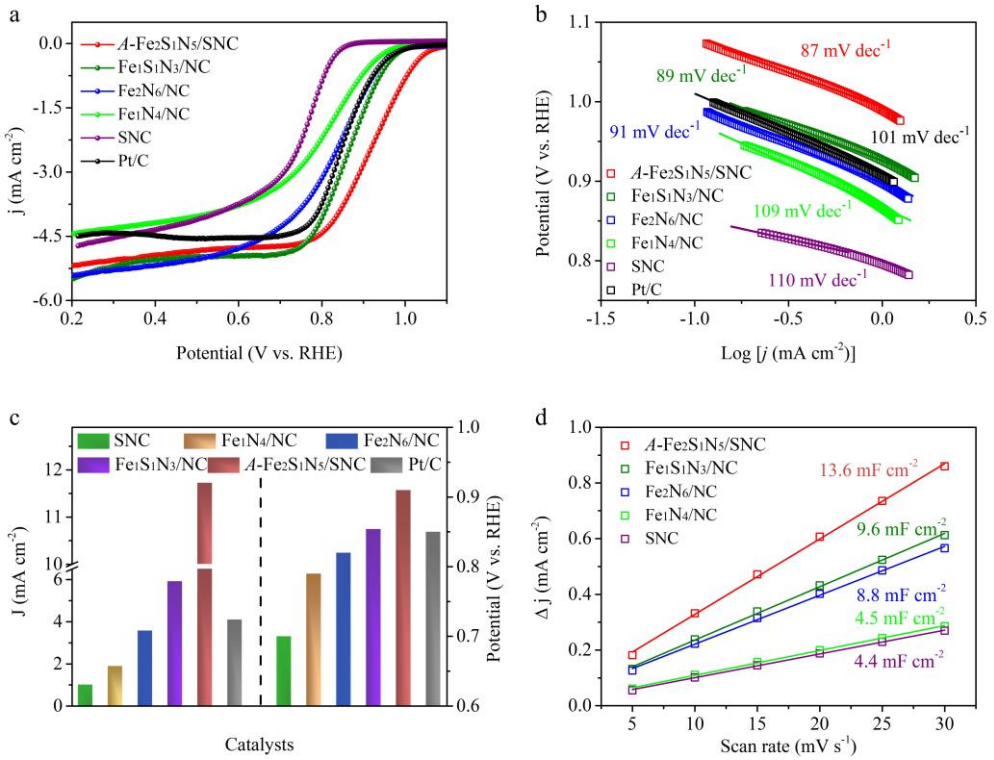

Supplementary Fig. 86. ORR electrochemical activity in 0.1 M KOH. (a) Linear sweep voltammetry curves (LSV) and (b) the corresponding Tafel plots of the different catalysts at 1600 rpm. (c) Kinetic current density (J_k) at 0.85 V versus reversible hydrogen electrode (versus RHE) and half-wave potentials of *A*-$Fe_2S_1N_5$/SNC, $Fe_1S_1N_3$/NC, Fe_2N_6/NC, Fe_1N_4/NC, SNC, and Pt/C catalysts. (d) Calculated C_{dl} values from corresponding samples.

As shown in **Supplementary Fig. 86a**, *A*-$Fe_2S_1N_5$/SNC displayed superior ORR activity as evidenced by a high onset potential (E_{onset}) of 1.05 V, close to that of Pt/C (0.99 V). However, $Fe_1S_1N_3$/NC, Fe_2N_6/NC, Fe_1N_4/NC, and SNC exhibited lower electrocatalytic performance with E_{onset} values of 0.98, 0.97, 0.95, and 0.83 V, respectively. Linear sweep voltammetry (LSV) curves of these catalysts indicated the best activity of *A*-$Fe_2S_1N_5$/SNC with aspect to its highest halfwave potential ($E_{1/2}$).

Specifically, $E_{1/2}$ of *A*-$Fe_2S_1N_5$/SNC, $Fe_1S_1N_3$/NC, Fe_2N_6/NC, Fe_1N_4/NC, SNC, and Pt/C was 0.91, 0.85, 0.82, 0.79, 0.70, and 0.85 V *vs.* RHE, respectively. The lowest Tafel slope of *A*-$Fe_2S_1N_5$/SNC (87 mV dec^{-1}) among those of $Fe_1S_1N_3$/NC (89 mV dec^{-1}), Fe_2N_6/NC (91 mV dec^{-1}), Fe_1N_4/NC (109 mV dec^{-1}), SNC (110 mV dec^{-1}), and Pt/C (101 mV dec^{-1}) also supported the superior ORR kinetics of *A*-$Fe_2S_1N_5$/SNC (**Supplementary Fig. 86b**). Moreover, *A*-$Fe_2S_1N_5$/SNC exhibited a remarkable kinetic current density (J_k) of 12.6 mA cm^{-2} at 0.85 V *vs.* RHE, about 4 times and 7 times higher than those of Fe_2N_6/NC (3.5 mA cm^{-2}) and Fe_1N_4/NC (1.8 mA cm^{-2}), respectively (**Supplementary Fig. 86c**). Moreover, the electrochemical double-layer capacitance (C_{dl}) examinations revealed that *A*-$Fe_2S_1N_5$/SNC exhibited the highest C_{dl} (13.6 mF cm^{-2}), confirming the highest exposed electrochemical active surface area for ORR (**Supplementary Fig. 86d**).

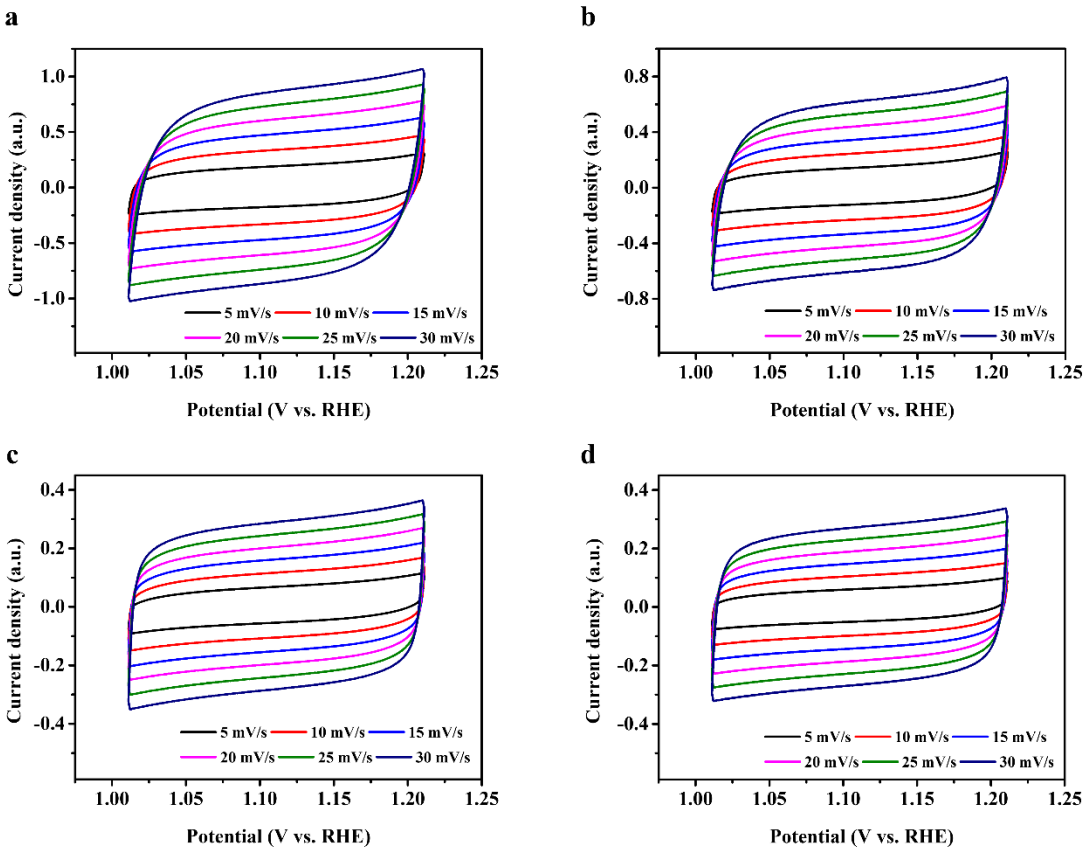

Supplementary Fig. 87. CV plots at various sweep rates. (a) *A*-$Fe_2S_1N_5$/SNC, (b) Fe_2N_6/NC, (c) Fe_1N_4/NC, and (d) SNC for ORR.

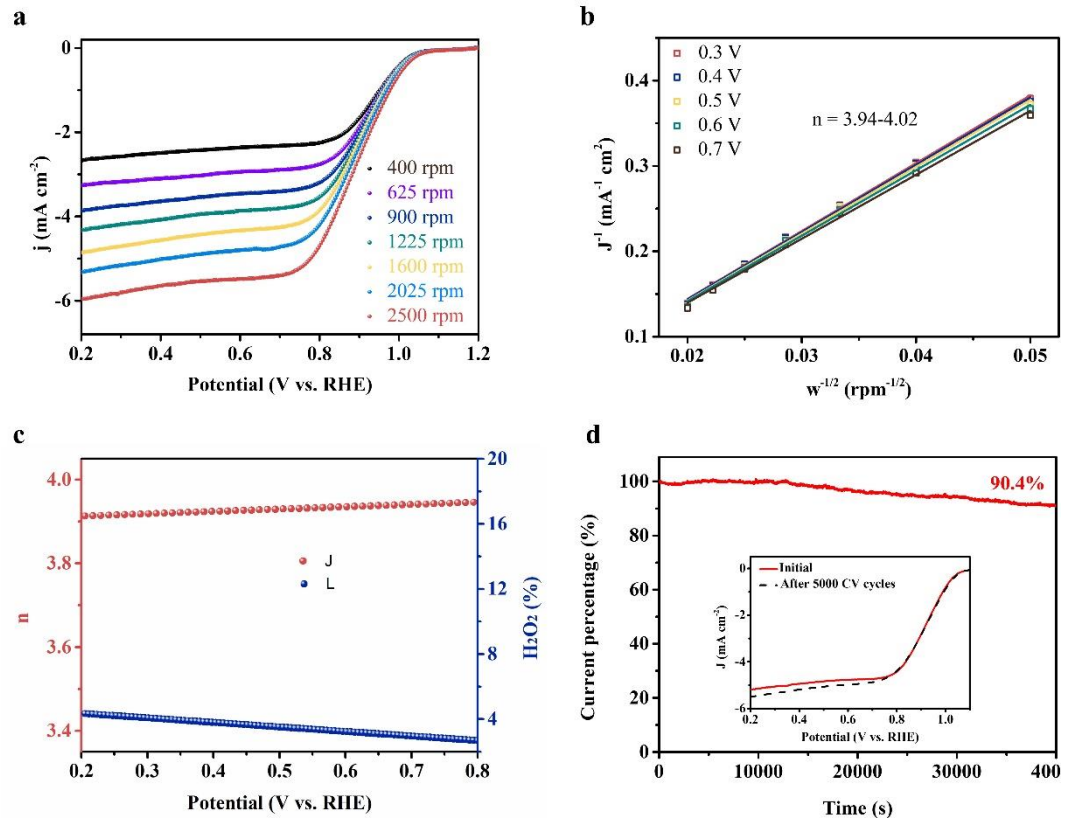

Supplementary Fig. 88. ORR electrochemical activity. (a) LSV curves of *A*-$Fe_2S_1N_5$/SNC at various rotation rates. (b) The K-L plots for *A*-$Fe_2S_1N_5$/SNC. (c) Electron transfer number (*n*, bottom) and H_2O_2 yield (top) versus potential for *A*-$Fe_2S_1N_5$/SNC. (d) Stability test of *A*-$Fe_2S_1N_5$/SNC. Inset: LSV curves before and after the 5000 CV test.

To further analyze the ORR reaction mechanism of the *A*-$Fe_2S_1N_5$/SNC catalyst, Koutecky-Levich plots at various applied potentials (**Supplementary Fig. 88a**) were collected to determine the electron transfer number (*n*) based on the LSV curves at various rotating speeds ranging from 400 rpm to 2025 rpm. Linear plots comply with the first-order reaction kinetic of the dissolved oxygen concentration and the *n*. According to the Koutecky-Levich equation, the *n* was calculated to be ≈ 4, signifying a high $4e^-$ selectivity for ORR (**Supplementary Fig. 88b**). Durability was another

important evaluation indicator of the electrocatalyst. In addition, the catalyst could still maintain high electrochemical durability after 40000 s of continuous operation under a constant voltage (**Supplementary Fig. 88d**).

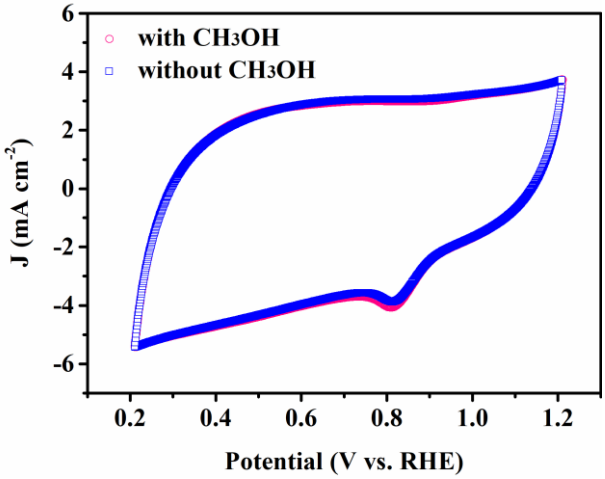

Supplementary Fig. 89. Cyclic voltammetry (CV) data for *A*-$Fe_2S_1N_5$/SNC in O_2-saturated 0.1 M KOH without and with 0.5 M CH_3OH. There was no obvious change in the current density for the *A*-$Fe_2S_1N_5$/SNC catalyst after methanol injection.

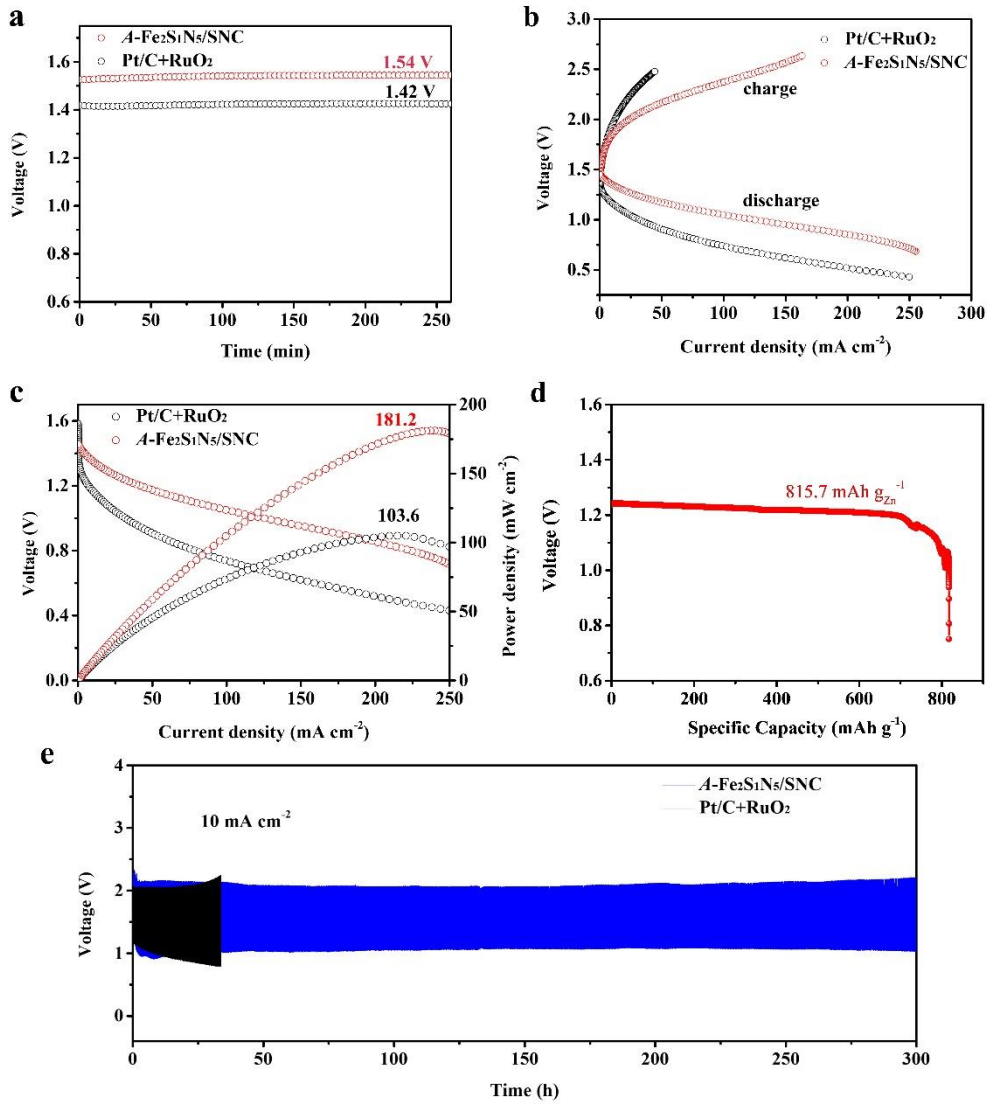

Supplementary Fig. 90. Rechargeable Zn-air battery performance. (a) Open-circuit voltage diagram of *A*-$Fe_2S_1N_5$/SNC and Pt/C-based ZABs. (b) Charge/discharge polarization. (c) LSV curves and corresponding power density plots. (d) Specific capacity measurements of *A*-$Fe_2S_1N_5$/SNC and Pt/C-based ZABs. (e) Galvanostatic discharge-charge cycling curves.

The *A*-$Fe_2S_1N_5$/SNC-based battery shows a maximum peak power density of 182.1 mW cm^{-2}, significantly higher than that of Pt/C+RuO_2 (103.6 mW cm^{-2}) based batteries. Importantly, the *A*-$Fe_2S_1N_5$/SNC-based battery delivered good performance

and outperformed most reported results. In **Supplementary Fig. 90d**, the specific capacity of *A*-$Fe_2S_1N_5$/SNC-based battery at discharge currents of 10 mA cm^{-2} was determined to be 815.7 mA h g^{-1}, and the corresponding Zn utilization ratios were calculated to be 95.7%. The cyclability of ZAB was evaluated under continuous galvanostatic discharge/charge at a current density of 10 mA cm^{-2} with a duration of 30 min per cycle (**Supplementary Fig. 90e**). Compared with Pt/C+RuO_2-based battery, *A*-$Fe_2S_1N_5$/SNC demonstrated negligible voltage decay within 300 h (600 discharge/charge cycles), revealing superior long-term durability. More importantly, the zinc–air battery assembled with *A*-$Fe_2S_1N_5$/SNC exhibited superior performance than other benchmarking counterparts in terms of peak power density, specific capacity, and cycling stability. The highly exposed active sites and unique electronic structure in SACs obtained by different synthesis methods contribute to the good bifunctional ORR and OER performance in rechargeable zinc–air batteries. Taken together, these results strongly support the superiority of *A*-$Fe_2S_1N_5$/SNC as a potential material in the zinc-air battery.

Supplementary Table 1 The porosity of as-prepared catalysts.

Samples	S_{BET} ($m^2\ g^{-1}$)	Total pore volume ($cm^3\ g^{-1}$)	Average pore diameter (nm)
A-$Fe_2S_1N_5$/SNC	1019.0	0.7294	2.42
$Fe_1S_1N_3$/NC	1073.4	0.7109	2.31
Fe_2N_6/NC	976.4	0.7391	2.35
Fe_1N_4/NC	994.9	0.7109	2.31
SNC	1125.3	0.7511	2.75

Supplementary Table 2 Light elements contents in the *A*-$Fe_2S_1N_5$/SNC using CHNS analysis.

Samples	C wt%	N wt%	S wt%	H wt%
A-$Fe_2S_1N_5$/SNC	80.05	11.55	1.775	0.098

Supplementary Table 3 Structural parameters extracted from the Fe K-edge EXAFS fitting. (S_0^2=0.87)

sample	Scattering pair	CN	R(Å)	σ^2(10^{-3}Å^2)	ΔE_0(eV)	R factor
Fe foil	Fe-Fe1	8	2.47	6.5	1.5	0.008
	Fe-Fe2	6	2.84	7.3		
Fe_1N_4/NC	Fe-N	4.0	1.95	6.7	1.0	0.005
Fe_2N_6/NC	Fe-N	3.1	1.92	5.4	2.0	0.008
	Fe-Fe	1.0	2.52	5.9		
A-$Fe_2S_1N_5$/SNC	Fe-N	2.5	1.90	4.1	2.0	0.006
	Fe-S	0.5	2.30	4.6		
	Fe-Fe	1.0	2.56	6.9		

S_0^2 is the amplitude reduction factor; CN is the coordination number; R is interatomic distance (the bond length between central atoms and surrounding coordination atoms); σ^2 is Debye-Waller factor (a measure of thermal and static disorder in absorber-scatterer distances); ΔE_0 is edge-energy shift (the difference between the zero kinetic energy value of the sample and that of the theoretical model). R factor is used to value the goodness of the fitting.

Supplementary Table 4 Calculated C_{dl} and ECSA values for different catalysts.

Catalyst	C_{dl} (mF)	ECSA (cm^2)[a]
A-$Fe_2S_1N_5$/SNC	3.2	91.4
$Fe_1S_1N_3$/NC	2.5	71.4
Fe_2N_6/NC	2.1	60.0
Fe_1N_4/NC	1.2	28.6

[a] ECSAs are determined by the equation of ECSA = $C_{dl}/C_s \times S$ and S is the electrode area (1.0 cm^2).

Supplementary Table 5 Comparison of OER performance with other catalysts.

Catalyst	Tafel slope (mV dec^{-1})	η_{10} (mV)	Durability (h)	reference
A-$Fe_2S_1N_5$/SNC	61	193[a]	>2000 50000 CV	This work
Ni-NHGF	63	331[a]	20	*Nature Catalysis* **2018**, 63-72
WC_x-FeNi	44	237[a]	1000	*Nature Materials* **2021**, 20, 1240-1247
Ir_1/Ni LDH-T	41	228[a]	12	*Nat. Commun.* ***2024, 152:559***
Ni/Fe-CNG	74	270[b]	72	*Nat. Commun.* **2021**, 12, 5589
NiFe-DASC	45	310[a]	30	*Nat. Commun.* **2021**, 12:4088
EA-FCCN (FeCoCrNi MCA)	38.7	221[a]	20	*Nat. Commun.* **2020**, 11:4066
Ru/CoFe-LDHs	39	198[a]	24	*Nat. Commun.* **2019**, 10:1711
S|NiNx-PC	45	280[a]	10	*Nat. Commun.* **2019**, 10:1392
$Ni_3Fe_{1-x}V_x$/CFP	39	264[a]	60	*Nat. Commun.* **2018**, 9:2885
Au-NiFeOOH	36	237[a]	20	*J. Am. Chem. Soc.* **2018**, 140, 3876-3879
Fe-Co-Ni MOF	53.1	254[a]	48	*J. Am. Chem. Soc.* **2022**, 144, 3411-3428

Co-Fe-N-C	37	309[a]	16	*J. Am. Chem. Soc.* **2019**, 141, 14190–14199
FeNiP/NCH	69	250[a]	72	*J. Am. Chem. Soc.* **2019**, 141, 7906-7916
P/Fe-N-C	65	304[b]	10	*J. Am. Chem. Soc.* **2023**, 145, 3647-3655
Co-SeMON	57.4	265[a]	50	*J. Am. Chem. Soc.* **2023**, 145, 2, 1144-1154
Co_2Fe_1@NC	141.6	420[b]	6	*J. Am. Chem. Soc*. **2020**, 142, 7116-7127
Fe_2/Co_1-GNCL	70	350[a]	200	*Angew. Chem. Int. Ed. **2023**, 62, e202314303*
Mg/Fe-N-C	52	224[b]	15	*Angew. Chem. Int. Ed.* **2019**, 58, 13565-13572
S, N-Fe/N/C-CNT	82	370[b]	11	*Angew. Chem. Int. Ed.* **2016**, 55, 1-6
a-NiCo/NC	49	252[a]	150	*Angew. Chem. Int. Ed.* **2022**, 61, e202207537
$(Ni,Fe)P(S,Se)_3$	34	210[a]	50	*Angew. Chem. Int. Ed.* **2023**, e202214570
$ZnCo_2O_4$/CNTs	59.2	350[b]	14	*Angew. Chem. Int. Ed.* **2023**, 62, e202301408
Fe-UNT	36.6	270[a]	10	*Angew. Chem. Int. Ed.* **2020**, 59, 2313-2317
Ir_1@Co/NC	119	315[a]	5	*Angew. Chem. Int. Ed.* **2019**, 19, 11868-11873
Fe-N_4 SAs/NPC	95	430[a]	20	*Angew. Chem. Int. Ed.* **2018**, 57, 8614-8618
CoFe/N-GCT	106	310[b]	10	*Angew. Chem. Int. Ed.* **2018**, 57, 16166-16170
Ni-BDC-1	89	225[a]	100	*Angew. Chem.* **2022**, *134*, e202214794
Ni SAs@S/N-FCS	56.5	249[a]	166	*Angew. Chem. Int. Ed.* **2022**, 61, e202212542
S/N-CMF@$Fe_xCo_yNi_{1-x-y}$-MOF	53.5	296[a]	100	*Adv. Mater. **2023**, 35, 2207888*
Fe/N-G-SAC	73	370[b]	2000 CV	*Adv. Mater.* **2020**, 2004900
Fe SAs/NC	55.5	320[b]	25	*Adv. Mater.* **2022**, 2209644
HCM@Ni-N	76	304[a]	12	*Adv. Mater.* **2019**, *31*, 1904548
CoNi-SAs/NC	58.7	340[a]	10	*Adv. Mater*. **2019**, 31, 1905622
Mo_1-NiFeOxHy	32.33	193[a]	30	*Adv. Mater.* **2022**, 34, 2202523
Ni SAs@S/N-CMF	50.8	285[a]	60	*Adv. Mater*. **2022**, 34, 2203442
Fe-NiMo-NH_3/H_2	28	192[a]	18	*Adv. Energy Mater.* **2020**, 2002285
Pt_1@Fe-N-C	62	310[b]	5	*Adv. Energy Mater*. **2018**, 8, 1701345
SCoNC	74	310[b]	56	*Adv. Energy Mater*. **2019**, 1900149
FePc||CNTs||NiCo/CP	50	358[b]	5000 CV	*Adv. Energy Mater.* **2022**, *12*, 2202984

$Fe_{0.55}Co_{0.45}BPO$	26	270[a]	50	*Adv. Energy Mater*. **2023**, 2203886
FeNi SAs/NC	54.68	270[a]	35	*Adv. Energy Mater.* **2021**, 11, 2101242
S-Fe-Co-N_5	59.2	260[b](η_{50})	20	*Adv. Energy Mater. **2023**, 13, 2301547*
NiFeLDH/Fe_1-N-C	41	320[a]	12	*Adv. Energy Mater.* **2023**, 2203609
Mn/Fe-HIB-MOF	45	280[b]	100	*Energy Environ. Sci.*, **2019**, 12, 727-738
Co/Fe-SNC800	47.92	240[a]	26	*Energy Environ. Sci.*, **2023**, 16, 1685–1696
Mn/Fe-HIB-MOF	45	280[b]	100	*Energy Environ. Sci.*, **2019**, 12, 727-738
A-Ni@DG	47	270[a]	10	*Chem* **2018**, 4, 285-297
planar-Fe-Co DSC	33.6	190[a]	160	*PNAS* **2024**, 121, e2317247121
Cu,Co/NSC3	85.4	339[a]	25	*Adv. Funct. Mater. **2024**, 34, 2311664*
Fe_3Co_7-NC	69	343[b]	60	*Adv. Funct. Mater.* **2023**, 33, 2212299
SS-Co-SAC NSAs	94.2	348[b]	80	*Adv. Funct. Mater.* **2019**, 29, 1906477
$Ni_{0.5}Fe_{0.5}$-THQ	47.9	272[b]	40	*Adv. Funct. Mater.* **2024**, 34, 2310902
Co_1/TaS_2-3	70	330[a]	121	*ACS Nano* **2021**, 15, 7105-7113
$NiSO_4$-GF	80	300[a]	20	*ACS Nano* **2020**, 14, 11662-11669
S-R-NiFe-CPs	30.8	245[a](η_{20})	25	*ACS Nano* **2022**, 16, 15318-15327
Fe,Co,N-C	76	410[b]	20	*ACS Nano* **2022**, 16, 5, 7890-7903
FePc-GO	112	420[b]	17	*ACS Nano* **2020,** 14, 13279–13293
Fe-N/S-CNT-GR	78	370[a]	12	*ACS Catal.* **2022**, 12, 7994-8006
Fe_1Co_3-NC-1100	99.93	349[b]	5000 CV	*ACS Catal.* **2022**, 12, 1216-1227
$Fe_1(OH)_x$/P-C	41	320[a]	20	*Nano Lett.* **2021**, 21, 4795-4801
NiFe-DG	76	358[a]	12	*Nano Energy* **2021**, 90, 106488
CoFe-N-C	68	360[b]	25	*Nano Lett.* **2022**, 22, 3392−3399
Fe–NiNC-50	54	340[b]	5000 CV	*Nano Energy,* **2020**, 71, 104597
FeCo/Se-CNT	74.2	340[b]	9	*Nano Lett*. **2021**, 21, 2255-2264
Ni-O-G SACs	42	224[a]	50	*Adv. Sci*. **2020**, 7, 1903089
FeCoDACys	67	320[b]	12	*Chem. Commun.* **2022**, 58, 1934
Fe-N-NDC-900	66.3	350[b]	12	*J. Mater. Chem. A* **2021**, 9, 5556-5565
NiFe@g-C_3N_4/CNT	67	326[a]	16	*J. Mater. Chem. A* **2018**, 6, 6840–6846

Fe-NC	114	450[b]	3000 CV	*J. Mater. Chem. A*, **2020**, 8, 9981-9990
Ni-O-G SACs	42	224[a]	50	*Adv. Sci.* **2020**, 7, 1903089
H-Co@FeCo/N/C	96	378[b]	12	*Applied Catalysis B: Environmental.* **2020**, 278, 119259

[a] in 1.0 M KOH electrolyte. [b] in 0.1 M KOH electrolyte. The electrolyte is 1.0 M KOH solution at a constant temperature of 25 ± 2 °C, with the mass loading of 0.26 mg cm^{-2}.

Supplementary Table 6. Results of metal leaching experiments (before and after 50000 CV cycles) by ICP.

Sample	Fe content (wt%)		Retention
A-$Fe_2S_1N_5$/SNC	Initial	6.72	97.9%
	50000 CV	6.57	

Supplementary Table 7 Structural parameters extracted from the Fe K-edge EXAFS fitting. (S_0^2=0.87)

sample	Scattering pair	CN	R(Å)	σ^2(10^{-3}Å^2)	ΔE_0(eV)	R factor
A-$Fe_2S_1N_5$/SNC-in situ-1.31V	Fe-N	2.4	1.88	3.7	3.0	0.007
	Fe-O	1.1	2.01	5.6		
	Fe-S	0.5	2.29	4.9		
	Fe-Fe	1.0	2.53	6.5		
A-$Fe_2S_1N_5$/SNC-in situ-1.42V	Fe-N	2.3	1.85	6.5	2.0	0.009
	Fe-O	1.4	2.01	5.8		
	Fe-S	0.4	2.27	5.9		
	Fe-Fe	1.1	2.49	7.0		

S_0^2 is the amplitude reduction factor; CN is the coordination number; R is interatomic distance (the bond length between central atoms and surrounding coordination atoms); σ^2 is Debye-Waller factor (a measure of thermal and static disorder in absorber-scattered distances); ΔE_0 is edge-energy shift (the difference between the zero kinetic energy value of the sample and that of the theoretical model). R factor is used to value the goodness of the fitting.

Supplementary Table 8 Structural parameters extracted from the Mn, Cu, Co, and Ni K-edge EXAFS fitting. (S_0^2=0.86)

sample	Scattering pair	CN	R(Å)	σ^2(10^{-3} Å^2)	ΔE_0(eV)	R factor
A-$Mn_2S_1N_5$/SNC	Mn-N	2.3	1.91	4.1	4.8	0.008
	Mn-S	0.6	2.34	2.5		
A-$Cu_2S_1N_5$/SNC	Cu-N	2.4	2.02	3.2	5.9	0.005
	Cu-S	0.5	2.31	6.8		
A-$Co_2S_1N_5$/SNC	Co-N	2.6	1.95	4.6	2.5	0.008
	Co-S	0.4	2.33	7.3		
A-$Ni_2S_1N_5$/SNC	Ni-N	2.5	1.93	5.3	3.7	0.007
	Ni-S	0.6	2.32	6.4		

Supplementary Table 9 The adsorption free energy of various intermediates on the *A*-$Fe_2S_1N_5$/SNC catalyst. MM represents the total magnetic moment. $\Delta G = \Delta G_{corr} + \Delta E$.

Species	MM/μB	ΔE/eV	ΔG_{corr}/eV	ΔG/eV
O	7.45	-0.65	0.01	-0.64
OH	7.93	-1.80	0.31	-1.49
2OH	0.33	-2.12	0.63	-1.49
3OH	8.00	-1.51	0.94	-0.57
2O	-1.00	0.81	0.02	0.83
3O	9.00	3.32	0.03	3.34
H-OH	1.00	-0.44	0.66	0.22

Supplementary Table 10 The adsorption free energy of various intermediates on the Fe_2N_6/NC catalyst. MM represents the total magnetic moment. $\Delta G = \Delta G_{corr} + \Delta E$.

Species	MM/μB	ΔE/eV	ΔG_{corr}/eV	ΔG/eV
O	8.00	-0.47	0.03	-0.44
OH	7.67	-1.57	0.32	-1.25
2O	8.00	1.80	0.07	1.87
3O	8.67	4.17	0.10	4.27
2OH	8.00	-1.64	0.64	-1.00
3OH	1.00	-0.94	0.95	0.01
H-OH	8.00	-0.63	0.64	0.01

Supplementary Table 11 The adsorption free energy of various intermediates on the $Fe_1S_1N_3$/NC catalyst. MM represents the total magnetic moment. $\Delta G = \Delta G_{corr} + \Delta E$.

Species	MM/μB	ΔE/eV	ΔG_{corr}/eV	ΔG/eV
O	3.00	1.64	-0.02	1.62
OH	2.00	0.23	0.26	0.49
2OH	3.00	0.49	0.52	1.01
2O	3.04	4.10	-0.04	4.07
H-OH	1.00	1.63	0.66	2.29

Supplementary Table 12 The adsorption free energy of OER intermediates on the 3O-$Fe_2S_1N_5$/SNC surface. $\Delta G = \Delta E + \Delta G_{corr}$, $\Delta G_{corr} = \Delta ZPE + \Delta H$ (0→298.15K) + $T\Delta S$, MM: total magnetic moment.

Species	MM/μB	ΔE/eV	ΔG_{corr}/eV	ΔG/eV
*OH	6.22	0.99	0.31	1.30
*O	5.17	2.84	0.01	2.85
*2OH	7.22	2.22	0.63	2.85
*OOH	8.03	3.77	0.31	4.09
*O+*OH	7.44	3.61	0.32	3.93
*2O	7.00	5.70	0.02	5.72
$*O_2$	7.16	4.96	-0.05	4.91

Supplementary Table 13 The adsorption free energy of OER intermediates on the 3O-Fe_2N_6/NC surface. $\Delta G = \Delta E + \Delta G_{corr}$, $\Delta G_{corr} = \Delta ZPE + \Delta H$ (0→298.15K) + $T\Delta S$, MM: total magnetic moment.

Species	MM/μB	ΔE/eV	ΔG_{corr}/eV	ΔG/eV
*OH	7.95	1.05	0.32	1.37
*O	7.98	3.00	0.03	3.04
*2OH	8.00	2.37	0.64	3.01
*OOH	7.23	4.17	0.31	4.48
*O + *OH	7.00	4.11	0.35	4.46
*2O	6.00	6.52	0.07	6.58
*O_2	8.67	5.18	-0.05	5.13

Supplementary Table 14 The adsorption free energy of OER/ORR intermediates on the 2OH-$Fe_1S_1N_3$/NC surface. $\Delta G = \Delta E + \Delta G_{corr}$, $\Delta G_{corr} = \Delta ZPE + \Delta H$ (0→298.15 K) + $T\Delta S$, MM: total magnetic moment.

Species	MM/μB	ΔE/eV	ΔG_{corr}/eV	ΔG/eV
*OH	2.21	1.06	0.28	1.34
*O	1.01	2.94	-0.02	2.92
*OOH	2.00	4.00	0.27	4.27
$*O_2$	4.78	4.61	-0.06	4.55

Supplementary Table 15 The adsorption free energy of ORR intermediates on the 2OH-Fe_2N_6/NC surface. $\Delta G = \Delta E + \Delta G_{corr}$, $\Delta G_{corr} = \Delta ZPE + \Delta H$ (0→298.15 K) + $T\Delta S$, MM: total magnetic moment.

Species	MM/μB	ΔE/eV	ΔG_{corr}/eV	ΔG/eV
$*O_2$	6.03	4.93	-0.05	4.88
*OOH	7.01	4.07	0.31	4.38
*O	8.13	2.62	0.03	2.65
*OH	7.00	0.95	0.32	1.27

Supplementary Table 16 The adsorption free energy of ORR intermediates on the 2OH-$Fe_2S_1N_5$/SNC surface. $\Delta G = \Delta E + \Delta G_{corr}$, $\Delta G_{corr} = \Delta ZPE + \Delta H$ (0→298.15 K) + $T\Delta S$, MM: total magnetic moment.

Species	MM/μB	ΔE/eV	ΔG_{corr}/eV	ΔG/eV
$*O_2$	9.00	4.65	-0.05	4.60
*OOH	8.00	3.82	0.31	4.13
*O	9.00	2.32	0.01	2.32
*OH	8.00	0.58	0.31	0.89

Supplementary Table 17 Comparison of our work with recent reported catalysts for AEMWE.

Anode//Cathode	Cell voltage (V)	Temperature (℃)	Area (cm^{-2})	Ref.
A-$Fe_2S_1N_5$/SNC//(Pt/C)	1.94@500 mA cm^{-2}	25[a]	4	This work
NiFe LDH//Co-1T-MoS_2-bpe	2.56@500 mA cm^{-2}	25[a]	1	[1]
NiFe LDH//OH-Ni/Ni_3C	2.35@500 mA cm^{-2}	25[a]	4	[2]
RuO_2//PtSA-NiSe-V	2.05@500 mA cm^{-2}	25[b]	4	[3]
RuO_2//Mn-O-Ru	2.36@500 mA cm^{-2}	25[a]	4	[4]
Ir@Zr-CoP//Ir@Zr-CoP	2.01@1 A cm^{-2}	25[a]	2	[5]
Tuning PtNiNb//PtIr	1.86@500 mA cm^{-2}	25[a]	1	[6]
Ni_2P/Ni_7S_6//(Pt/C)	1.88@500 mA cm^{-2}	75[a]	1	[7]
NiCoFe-Bi/NF//Co_3S_4/NF	1.98@500 mA cm^{-2}	50[c]	4.9	[8]
NiFe LDH//$NiFeP_x$	2.58@500 mA cm^{-2}	60[b]	4	[9]
S-NiFe LDH//Pt@S-NiFe LDH	2.5@500 mA cm^{-2}	65[a]	1	[10]
$Ir_1/Co(OH)_2$//$Pt_1/Co(OH)_2$	2.15@500 mA cm^{-2}	75[a]	1	[11]
$NiCoP_v$@NF//$NiCoP_v$@NF	1.94@500 mA cm^{-2}	25[a]	-	[12]

Measured in [a]:1.0 M KOH, [b]: 6.0 M KOH and [c]: KBi-containing KOH.

Supplementary Notes

Supplementary Note 1: Calculation for Turnover Frequency (TOF)

Initially, it was assumed that each iron atom within the catalyst contributed to the formation of a single active center. The quantity of iron (Fe) atoms present in the *A*-$Fe_2S_1N_5$/SNC catalyst was determined based on the molar mass of Fe and the mass loading on the carbon cloth electrode, which was obtained from the results of ICP analysis. The Fe content of the catalyst, as indicated by ICP-OES measurements, was approximately 6.72%, with a mass loading of around 0.67 mg cm^{-2}. Consequently, the Turnover Frequency (TOF) of the *A*-$Fe_2S_1N_5$/SNC electrocatalyst was calculated using equation (1).

$$\mathrm{TOF}=\frac{\text{number of } O_2 \text{ turnovers}}{\text{number of metal ions}} \tag{1}$$

The number of total O_2 turnovers was calculated using the current density (j) from the OER-LSV polarization:

Number of

$$O_2 \text{ turnovers} \left(j\frac{\mathrm{mA}}{\mathrm{cm}^2}\right)\left(\frac{1\ \frac{\mathrm{C}}{\mathrm{s}}}{1000\ \mathrm{mA}}\right)\left(\frac{1\ \mathrm{mol\ e^-}}{96485\ \mathrm{C}}\right)\left(\frac{1\ \mathrm{mol\ O_2}}{4\ \mathrm{mol\ e^-}}\right)\left(\frac{6.02\times10^{23}\ \mathrm{mol\ O_2}}{1\ \mathrm{mol\ O_2}}\right)$$

$$=1.56\times10^{15}\ \frac{{O_2}/{\mathrm{s}}}{\mathrm{cm}^2}\ \mathrm{per}\ \frac{\mathrm{mA}}{\mathrm{cm}^2} \tag{2}$$

The upper limit of active sites density for *A*-$Fe_2S_1N_5$/SNC:

$$=\frac{0.67\ \mathrm{mg\ cm^{-2}}\times10^{-3}\times6.72\%\times6.023\times10^{23}}{55.85\ \mathrm{g\ mol^{-1}}}\ \mathrm{per\ cm^2}$$

$$=0.48\times10^{18}\ \mathrm{Fe\ site\ per\ cm^2} \tag{3}$$

The TOF of *A*-$Fe_2S_1N_5$/SNC can be obtained via the current density from the OER LSV polarization curves and according to:

$$TOF=\frac{1.56\times10^{15}}{0.48\times10^{18}}\ |j|=0.0033|j| \quad (4)$$

Particularly, at the overpotential of 250 and 300 mV, the current density of OER is 50 and 242 mA cm^{-2}, respectively. Therefore, the TOF values of the *A*-$Fe_2S_1N_5$/SNC electrocatalyst were calculated to be:

$$TOF_{(250\ mV)} = 0.0033\times50 = 0.165\ O_2\ s^{-1} = 594\ O_2\ h^{-1}. \quad (5)$$

$$TOF_{(300\ mV)} = 0.0033\times242 = 0.799\ O_2\ s^{-1} = 2875\ O_2\ h^{-1}. \quad (6)$$

Supplementary Note 2: Mass activity (MA) calculation

Mass activity (A g_{metal}^{-1}) was derived from the current density (mA cm^{-2}) that normalized by the mass loading (0.67 mg cm^{-2}) and per metal at a certain applied overpotential. As the following equation exhibited the mass activity of *A*-$Fe_2S_1N_5$/SNC:

$$\text{Mass activity} = \frac{|j|}{0.67\times6.72\%} = 22.2|j|\ A\ g_{metal}^{-1}\ \text{per}\ cm^2 \quad (7)$$

The current densities for *A*-$Fe_2S_1N_5$/SNC are 50 and 242 mA cm^{-2} at the overpotential of 250 and 300 mV, respectively. Therefore, the mass activities were calculated to be:

$$\text{Mass activity}_{250\ mV} = 22.2\times50 = 1110\ A\ g_{metal}^{-1} = 1.11\ A\ mg_{metal}^{-1} \quad (8)$$

$$\text{Mass activity}_{300\ mV} = 22.2\times242 = 5372\ A\ g_{metal}^{-1} = 5.37\ A\ mg_{metal}^{-1} \quad (9)$$

Supplementary Note 3: Faradaic efficiency (FE) determination

To assess the Faradaic efficiency of oxygen evolution, we need to evaluate the ratio of the amounts of O_2 produced experimentally to those of O_2 produced theoretically at

cathodic electrolysis. Therefore, the FE was calculated by the following equations:

$$FE = \frac{n \times F \times V}{Q \times V_m} \times 100\% \quad (10)$$

Where n is 4 for O_2 production. F is the Faraday constant (96485 A·s mol^{-1}), and V is the oxygen volume measured by the drainage method at a current density of 10 mA cm^{-2} under the standard conditions (room temperature). V_m is the molar volume (22.4 L/mol) and Q is the total theoretical electric charge. Test condition: The Faradaic efficiency was estimated using a simple water drainage method. The evolved O_2 was collected in a 10 mL graduated tube filled with electrolyte. The current was fixed at 10 mA cm^{-2} for about 60 minutes under standard conditions (25 ℃, 1 atm). The gas volume of O_2 collected was recorded every 10 minutes. The accumulated charge passing through the working electrode was calculated by the equation ($Q = It$).

Supplementary Note 4: XAFS measurements

The X-ray absorption fine structure spectra data were collected at BL1W1B station in Beijing Synchrotron Radiation Facility (BSRF) respectively. The data of the samples were collected at room temperature (Fe K-edge in fluorescence excitation mode using a Lytle detector). All samples were pelletized as disks of 13 mm diameter with 1mm thickness using PVDF powder as a binder.

The EXAFS spectra were obtained by subtracting the post-edge background from the overall absorption and then normalizing with respect to the edge-jump step. Subsequently, the χ(k) data of Fourier transformed to real (R) space using a hanning window (dk = 1.0 $Å^{-1}$) to separate the EXAFS contributions from different coordination shells. To obtain the quantitative

structural parameters around central atoms, least-squares curve parameter fitting was performed using the ARTEMIS module of the IFEFFIT software packages.

The following EXAFS equation was used:

$$\chi(k)=\sum_{j}\frac{N_j S_o^2 F_j(k)}{k R_j^2}\exp[-2k^2\sigma_j^2]\exp[\frac{-2R_j}{\lambda(k)}]\sin[2kR_j+\phi_j(k)] \quad (11)$$

S_0^2 is the amplitude reduction factor, $F_j(k)$ is the effective curved-wave backscattering amplitude, N_j is the number of neighbors in the j^{th} atomic shell, R_j is the distance between the X-ray absorbing central atom and the atoms in the j^{th} atomic shell (backscatter), λ is the mean free path in Å, $\phi_j(k)$ is the phase shift (including the phase shift for each shell and the total central atom phase shift), σ_j is the Debye-Waller parameter of the j^{th} atomic shell (variation of distances around the average R_j). The functions $F_j(k)$, λ, and $\phi_j(k)$ were calculated with the ab initio code FEFF8.2. The additional details for EXAFS simulations are given below.

The coordination numbers of model samples were fixed as the nominal values. The obtained S_0^2 was fixed in the subsequent fitting. While the internal atomic distances R, Debye-Waller factor σ^2, and the edge-energy shift ΔE_0 were allowed to run freely.

Supplementary Note 5: ICP-OES measurements

ICP-OES was used to detect the metal content before and after stability testing of the catalyst, only a small amount of the elements dissolved into the electrolyte. The aqua regia was prepared by mixing concentrated hydrochloric acid and concentrated nitric acid in a 1:3 volume ratio for the experiment. 1.0 mg catalyst powder was added in 8 mL of aqua regia. The obtained solution was kept in an oil bath for 5 h at 90 ℃, and then added 10 mL DI into the solution and

maintained for 2 h at 120 ℃. After cooling down, filtered the obtained solution, and diluted it to a 50 mL volumetric flask, taking 10 mL for later use.

Open the liquid Ar switch and gas pathway. After opening the software and starting the measurement, place the catheter into the test solution. When the liquid inside the catheter rises and enters the instrument, click 'Start'. After the test is completed, check the displayed scalar result, if it is greater than 0.999, perform sample detection. Click on the results list, record the test results, and complete the test. Click 'Shut down', then turn off the gas path, exhaust switch, power supply, gas pathway, and liquid Ar switch in sequence.

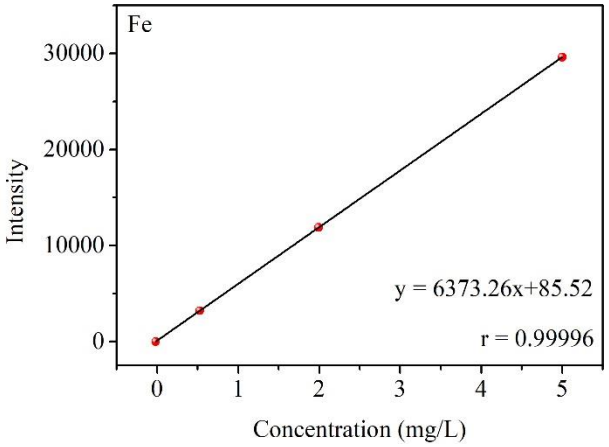

Supplementary Fig. 91. Calibration curves of Fe element for ICP test.

References

1 Liu, H.-J., Zhang, S., Chai, Y.-M. & Dong, B. Ligand modulation of active sites to promote cobalt-doped 1T-MoS_2 electrocatalytic hydrogen evolution in alkaline media. *Angew. Chem. Int. Ed*. **62**, e202313845, (2023).

2 Wen, Q. et al. Engineering a local free water enriched microenvironment for surpassing platinum hydrogen evolution activity. *Angew. Chem. Int. Ed.* **61**, e202206077, (2022).

3 Chen, Z. et al. Stabilizing Pt single atoms through Pt−Se electron bridges on vacancy-enriched nickel selenide for efficient electrocatalytic hydrogen evolution. *Angew. Chem. Int. Ed*. **62**, e202308686, (2023).

4 Yang, C. et al. Mn-oxygen compounds coordinated ruthenium sites with deprotonated and low oxophilic microenvironments for membrane electrolyzer-based H_2-production. *Adv. Mater*. **35**, 2303331, (2023).

5 Ngo, Q. P., Nguyen, T. T., Le, Q. T. T., Lee, J. H. & Kim, N. H. Unveiling the synergistic effect of atomic iridium modulated zirconium-doped pure phase cobalt phosphide for robust anion-exchange membrane water electrolyzer. *Adv. Energy Mater*. **13**, 2301841, (2023).

6 Gu, J. et al. Turing structuring with multiple nanotwins to engineer efficient and stable catalysts for hydrogen evolution reaction. *Nat. Commun*. **14**, 5389, (2023).

7 Wang, F.-L. et al. Porous heterojunction of Ni_2P/Ni_7S_6 with high crystalline phase and superior conductivity for industrial anion exchange membrane water electrolysis.

Applied Catalysis B **330**, 122633, (2023).

8 She, X. et al. A stable alkaline anion exchange membrane water electrolyzer based on a self-healing anode. *International Journal of Hydrogen Energy* **59**, 1297-1304, (2024).

9 Zhao, J., Liao, N. & Luo, J. Transforming NiFe layered double hydroxide into $NiFeP_x$ for efficient alkaline water splitting. *Journal of Materials Chemistry A* **11**, 9682-9690, (2023).

10 Lei, H., Wan, Q., Tan, S., Wang, Z. & Mai, W. Pt-quantum-dot-modified sulfur-doped NiFe layered double hydroxide for high-current-density alkaline water splitting at industrial temperature. *Adv. Mater*. **35**, 2208209, (2023).

11 Cao, D. et al. One-step approach for constructing high-density single-atom catalysts toward overall water splitting at industrial current densities. *Angew. Chem. Int. Ed*. **62**, e202214259, (2023).

12 Guo, L. et al. Phosphorus defect mediated electron redistribution to boost anion exchange membrane-based alkaline seawater electrolysis. *Adv. Energy Mater*. **14**, 2400975, (2024).